Metal−organic framework-derived nanomaterials in environment related fields: fundamentals, properties and applications

Yangzhuo He [a, b, 1], Ziwei Wang [a, b, 1], Han Wang [a, b, 1], Zixuan Wang [a, b, 1], Guangming Zeng [a, b, *], Piao Xu [a, b, *], Danlian Huang [a, b], Ming Chen [a, b], Biao Song [a, b], Hong Qin [a, b], Yin Zhao [a, b]

[a] *College of Environmental Science and Engineering, Hunan University, Changsha 410082, P.R. China.*

[b] *Key Laboratory of Environmental Biology and Pollution Control, Ministry of Education, Hunan University, Changsha 410082, P.R. China.*

[*]Corresponding Authors at: College of Environmental Science and Engineering, Hunan University, Changsha 410082, PR China; E-mail addresses: zgming@hnu.edu.cn (G. Zeng) and piaoxu@hnu.edu.cn (P. Xu).

[1] These authors contribute equally to this article.

Abstract: Metal–organic frameworks (MOFs) as a new class of crystalline porous materials, composing of metal nodes and organic linkers, have been extensively used as versatile precursors or sacrificial templates for the preparation of numerous nanomaterials. The advantages of these MOF-derived nanomaterials such as controllable composition, tunable structure and high porosity endow them with enormous potential in many areas, including catalysis, sensors, energy storage and conversion. Herein, MOF derivatives in environment related fields are highly emphasized. The fundamental properties and general background of these nanomaterials are summarized. The primary strategies involved in compositional manipulation, pre-synthetic modulation, morphology control and post-synthetic treatment to improve the performance of MOF-derived nanomaterials are highlighted. In addition, we systematically discuss their recent progress in environmental cleaning and monitoring, especially for the wastewater treatment, air purification and target-specific sensing. Finally, the challenges and prospects of MOF-derived nanomaterials are also proposed. This article gives a comprehensive overview of MOF-derived nanomaterials for environmental applications and is expected to shed light on the further study in this highly exciting area.

Keywords: metal−organic frameworks; derivatives; nanomaterials; environmental remediation; sensing.

Contents

1. Introduction

Over the past decades, the booming modern science and technology has caused serious threats and challenges to human survival and development such as energy shortage, ecological destruction and environmental deterioration. In order to mitigate these ever-increasingly severe issues, the utilization of advance technology is of great significance. Nanomaterials have aroused widespread research interest owing to the inherent superiorities including large surface area to volume ratio, stability, easy to fabrication as well as distinct electrical, optical and magnetic behaviors [1-4]. These novel features related to their molecular level state are generally not observed in conventional and macro-scale materials, motivating great potential for many applications no matter in emerging or the traditional domains [5-9]. Typically, environmental pollution as a long-term problem has been evidently alleviated because of the development of nanomaterials [10-13]. Exploiting more new types of functional nanomaterials for contaminant removal and detection are critically needed in environmental field [14-19].

Metal-organic frameworks (MOFs, also known as porous coordination polymers (PCPs)), constructing from metal-containing nodes (*i.e.* metal ions or clusters) and organic linkers, have attracted a great deal of concerns and emerged as one of the most fascinating advanced materials for both academia and engineering due to their intrinsic properties. The compositions and structures of MOFs can be facile tuned by adjusting the well-designed organic and inorganic building blocks or changing the synthetic

conditions, and their morphologies can be carefully tailored to display ultrahigh surface area and porosity, high intensity and desirable chemical activity. Moreover, MOFs can serve as excellent supports to combined with other active species to form MOF composites due to their favorable surface area and porous structure [20-25]. However, the instability in water or other harsh conditions resulted from the weak coordination bonding between organic ligands and metal nodes as well as the weak conductivity restricts the practical utilization of many MOFs [26, 27]. For instance, when MOF-5 exposed to atmospheric environment, its structure begins to collapse over 10 min, let alone at humid conditions [28]. With studies progressed, researchers found that when employed as sacrificial templates/precursors, MOFs can be transformed to nanomaterials (carbon materials, metal oxides, metal phosphides, metal carbides, metal chalcogenides as well as their hybrids) with much better stability [29-31]. Using MOFs as starting materials to fabricate carbon/metal-based porous nanomaterials has sparked considerable research interest. These nanoporous materials converted from MOFs, namely MOF derivatives, show synergistic effect by combining metallic and carbonaceous characters due to the hierarchical structures and metallic contents [32]. In addition, MOF derivatives could inherit the strengths and maintain original morphology of parent MOFs, which endows them with superior functional properties such as extremely highly specific surface area, tailored porosity, tunable pore size and diverse composition, enabling them as highly attractive candidates for chemical sensing, gas storage, energy conversion, catalysis, etc [33-36].

Actually, the derivation of MOFs creates new opportunities for the preparation of novel diversified nanomaterials with many attracting properties, mainly as following points: (i) facile preparation process without extra templates; (ii) controllable pore size and ordered/uniform distribution pore structure; (iii) accurate adjustment of active sites; (iv) enough choices for synthetic product in virtue of the diversity of metal nodes and ligands in pristine MOFs; (v) simple heteroatom doping and hybridization with other functional materials [37-40]. Thus, MOF-derived nanomaterials with ultrahigh porosity, large surface area and tailored texture open up an avenue to various applications.

As far as we know, MOF derivatives have been extensively investigated in the energy related area, such as supercapacitors, water splitting, lithium-ion batteries and hydrogen storage [41-46]. Their utilization in environmental field is extremely promising as well. Although several reviews about adsorption and catalysis are reported [47-49], the review with comprehensive emphasis on this field is rare. There is still lack of a comprehensive and systematic summary of these newly emerged MOF-derived nanomaterials in the environmental application. Providing a focus review to summarize MOF-derived nanomaterials with versatile components and/or sophisticated architectures for environmental related application is highly expected. This would give researchers a deep understanding of the recent progress in various applications (e.g. adsorption, catalysis and sensing) of these functional materials derived from MOFs as well as the relationship between their enhanced performance and well-designed structures.

In this article, fundamental properties and general background of MOF derivatives are briefly summarized. The primary strategies to enhance the performance of nanomaterials derived from MOFs especially for the environmental remediation and monitoring are highlighted. Most importantly, this overview emphasizes the promising applications of MOF-derived nanomaterials for air purification (CO_2 capture and separation, volatile organic compounds (VOCs) degradation, and radionuclide adsorption and separation), wastewater treatment (adsorption and catalytic degradation), and target-specific sensing (gaseous pollutants sensing, organic pollutants sensing, and heavy metal ions sensing). The research scope mainly focuses on the excellent achievements in the past ten years. Finally, the bottlenecks and perspectives for future work of MOF-derived nanomaterials in this highly significant area are critically proposed. In short, this overview aims at providing a new insight into the elaborate design and potential application of advanced MOF-derived nanomaterials in environmental field.

2. Brief overview of MOF-derived nanomaterials

First coordination polymer (known as MOF) was reported in 1959 [50]. Then, MOF constructions and functionalization were pioneered and emphasized in the 1990s [51-53]. Until now, over 70, 000 MOFs have been discovered [54], but just a limited species have been selected as suitable templates/precursors and utilized successfully, such as MOF-5, MOF-74, UiO-66 (UiO stands for University of Oslo), MILs (Matérial Institut Lavoisier), ZIFs (Zeolitic Imidazolate Frameworks), etc. Consequently, great

attention has been paid to MOF-derived nanomaterials due to their diverse compositions and they have been regarded as outstanding substitutions in many areas. In 2008, pristine porous carbons as the first reported MOF-derived nanostructures were prepared by carbonization of MOF-5 precursors [55]. Later, the same group also prepared the nanomaterials by heating ZIF-8 with furfuryl alcohol (FA) [56]. Since then, a variety of metal-based nanoscale materials were obtained using MOFs as the starting materials [57, 58]. Versatile metal compounds containing Zn(II), Cu(II), Al(III), Fe(III) or Zr(IV) can be constructed due to the diversity of metal nodes of parent MOFs [59-61]. MOF-derived nanoporous carbons with more heteroatomic doping, reactive sites and favorable structural stability can be ascribed to the diversiform of organic ligands, including amines, carboxylates, phosphates and sulfonates. The nanostructured architectures synthesized by this novel MOF-templated pathway possess much superiority compared with the traditional methods. Fig. 1 summarized the breakthrough of MOF-derived nanomaterials in the environmental field.

Through the meticulous control of chemical/thermal conversion, various nanomaterials with structural and compositional merits derived from MOFs such as metal compounds, carbonaceous nanomaterials, and metal/carbon hybrids [62-64] can be gained. Apart from the extra acquired advantages (e.g. water stability) after heating, MOF-derived nanocomponents can effectively retain the highly BET surface area, porous architecture and basic morphology of parent MOFs [65-67]. Meanwhile, the common equipment for the production process offers much more possibilities for the

large-scale industrial preparation for the MOF-derived nanomaterials, which involved in a furnace responsible for the high-temperature calcination and a gas supply system capable of providing predetermined pyrolysis atmosphere (e.g. N_2, Ar, air). In the fabrication process, themolysis conditions (e.g. heating rate, pyrolysis temperature, annealing parameters and gaseous condition) greatly govern the composition and shape of MOF derivatives and further influence their properties in relevant applications [68, 69]. Owing to the thorough consumption of MOF templates in the fabrication of nanoparticles, only carbon and/or nanoparticles were reserved at last [70]. With the extensive investigation of employing MOFs as sacrificial templates/precursors to acquire versatile materials in recent years, several reviews on the synthesis of porous nanostructures derived from MOFs are available [21, 29, 32]. Therefore, for a more comprehensive and systematic overview on the preparation of the MOF-derived porous materials, we refer readers to these publications.

Over the recent years, researchers have bended to develop more excellent nanomaterials derived from MOFs for overcoming the energy shortage. It is worthy to note that removing/detecting environmental pollutants is also of great potential. For instance, with the large specific surface areas, MOF-derived materials display a large density of active sites and thus can be employed as remarkable heterogeneous catalysts, co-catalysts, or catalyst supports for numerous reactions [71, 72]. Moreover, the controllable pore size and high porosity endow them with the excellent adsorption ability for target pollutants [73]. In addition, MOF-derived metal oxide semiconductors

with inherited advantages from original precursors can concentrate and capture more analytes with suitable pore diameter and configuration, further achieving high sensing performances [74, 75]. Taking into account these intrinsic characteristics, MOF-derived nanomaterials are a class of promising next-generation material with superb efficiencies for wastewater treatment, air purification and detection for specific pollutants. Inevitably, however, derivatives obtained from directly pyrolyzing pristine MOFs also have some disadvantages, and therefore much more efforts have been devoted to enhancing their performance to adapt for environment-related applications. The details will be discussed in next section.

3. Strategies to improve the performance of MOF-derived nanomaterials

At an early stage, studies revealed that some MOF derivatives tend to undergo structural collapse and serious particle aggregation in high-temperature pyrolysis. The inevitable damage to original morphologies of MOFs result in featureless morphologies of bulk materials [76]. Additionally, active metal species leached from MOF-derived nanoporous carbon materials can cause secondary pollution to water system [77]. These above-mentioned shortcomings may hinder their extensive application in environment. So far, there are four popular routines to accomplish the improvement of performance: (i) judiciously manipulating the components of MOF-derived nanomaterials; (ii) precisely controlling the morphology/structure of the derivatives; (iii) pre-synthetic modulation of MOF precursors; (iv) post-synthetic treatment for calcined MOFs. In some cases, these pathways are adopted simultaneously.

3.1 Compositional manipulation

Multiple selections of component of MOFs bring infinite potential to the diversity of their derivatives, enabling them with the desirable physico-chemical properties in various fields. Through ingenious manipulation of metal nodes/ organic ligands and the conversion conditions such as pyrolytic atmospheres and temperature, MOFs as excellent sacrificial precursors/templates can be converted to metal compounds (e.g. metal oxides/chalcogenides/phosphides/carbides and their composites), carbons, and their hybrids. Rational selection of suitable precursors is of great importance because of the diversity of metal nodes and organic ligands. Specifically, metal complex contained Fe, Co, Cu or their hybrids derived from MOFs with changeable valence state can be employed as the catalyst directly or co-catalyst in Fenton system and persulfate (PS)/peroxymonosulfate (PMS) activation [78-80]. Ti-based metal compounds are regarded as a potential alternative to improve the photocatalytic activity [81]. Aside from metal nodes, organic linkers in MOFs are important for the thermal stability, which mainly depend on the metal-ligand bond strength, and thus avoid structure collapse under high-temperature calcination. As is well-known, the bond strength is positively related to charges of metal cations and negatively associated with the ionic radius. High-valent metal ions like Zr^{4+}, Ti^{4+}, Fe^{3+}, Al^{3+} and Cr^{3+} with high charge densities could generate powerful coordination bonds and thereby a more stable network [82-84]. In addition, the stable framework of MOFs also can be assembled by

soft divalent metal ions (e.g. Ag^{+}, Cu^{2+}, Zn^{2+}, Mn^{2+} and Ni^{2+}) and soft azolate ligands (e.g. pyrazolates, tetrazolates, triazolates, and imidazolates) [85].

By careful selection and design of the MOF precursors, their derivatives with distinct features show outstanding activity for specific environmental applications. Metal compounds with versatile chemical components like bi-/tri-metallic compounds and complex heterojunction can be constructed for enhanced performance in catalysis and sensing [86, 87]. The prepared carbonaceous nanomaterials possess ultrahigh surface area, favorable porosity and tunable pore size, which could benefit the adsorption ability and extremely improve the accessibility of the target molecules into the active locations, further ensuring the rapid diffusion of the target molecular for catalysis [88]. In view of the simultaneous existence of metal components and organic in MOFs, metal/carbon hybrids can be easily fabricated. The composites composed of metal and carbon successfully combine the strengths of each composition and trigger the synergic action between them. In the next sections, the fundamental synthetic approaches of MOF derivatives in terms of compositional manipulation are summarized.

3.1.1 MOF-derived metal compounds

Metal compounds involved in metal oxides, metal phosphides, metal chalcogenides (MX, X = S, Se, Te) and metal carbides are a crucial kind of materials with great promise in many applications. The release of internally formed CO_2 and H_2O during the oxidative decomposition of organic linkers in MOFs eventually results in the

generation of metal compounds [89]. Among these metal-based materials derived from MOFs, metal oxides have received particular interest owing to their ultrahigh surface area and ample pore structures inherited from the parent MOF. Generally, direct pyrolysis of MOFs under oxygen-containing flow generates corresponding metal oxides. Tao and co-workers constructed the regular rod-like CeO_2 photocatalysts with rich oxygen vacancies, high crystallinity and wide UV absorption range by calcination of Ce-MOF under 450 ℃ for 4 h [90]. The prepared samples showed 98% degradation rate for methyl orange (MO) within 36 min under ultraviolet light. Likely, a mixed-phase (anatase and rutile) TiO_2 photoanode with octahedral structure was fabricated by using MIL-125-NH_2 as a sacrificial template and annealing under air atmosphere for 4 h at 500 ℃ [30]. The obtained photoanode was employed for hydrogen generation and performed well after sensitization.

Aside from single metal oxides, construction of polymetallic oxides also can be achieved. Typically, Cheng and colleagues developed a simple two-step process to obtain porous CuFe oxide (CuFeO) through heating the Cu-Fe prussian blue analogs (PBAs) under 550 ℃ and keeping at the same temperature for 2 h in air [91]. The formed CuFeO as catalyst showed massive and accessible active sites because of its large surface and high porosity. The synergistic effect among Cu, Fe and photo-induced electrons indicated prominently enhancement of performance in the catalytic activation of H_2O_2, facilitating the generation of •OH and $•O_2^-$. Jiang et al. obtained MnO_x-CeO_2 through the impregnation approach and subsequently by calcination at 300 °C for 6 h

274 in air [92]. Mn cations were infiltrated into Ce-BTC (BTC stands for benzene-1,3,5-
275 tricarboxylate) in solution by adding $MnNO_3$ as Mn source. The load of 7% manganese
276 oxide on CeO_2 supports greatly increased the active sites and promoted the catalytic
277 activity. Notably, the metal node of MOF precursor exerts an impact on final production.
278 In 2012, Das et al. indicated that metal atom with -0.27 V reduction potential or larger
279 (e.g. Cu, Ni or Co) in MOFs, pure metal nanoparticles were fabricated by calcination
280 in an inert (e.g. N_2 or Ar) gas, and the formed carbon in the reaction may give rise to
281 the metal nanoparticles by the reduction of metal ions. On the contrary, the MOFs
282 consisting of the metal atom with reduction potential lower than -0.27 V (e.g. Mn, Mg,
283 Al, Cr or Zn) can form metal oxide nanoparticles by combining with oxygen presented
284 in the organic linker of MOFs during the final treatment, because these metal ions are
285 incapable of reducing to a zero oxidation state to generate their respective metal
286 nanoparticles (Fig. 2) [93].

287 In addition to metal oxides, diverse metal-based functional materials, such as
288 sulfides [94-96], selenides [97, 98], phosphides [99, 100], carbides [101, 102], and their
289 nanocomposites, can be afforded by introducing additional precursor into MOF solution
290 and then following heat treatment. For example, Yu et al. investigated an anisotropic
291 chemical etching and ion exchange approach to convert Ni-Co PBA nanocube
292 templates into NiS nanoframes with tailored size by reacting with Na_2S in solution [94].
293 The annealed NiS nanoframes showed enhanced characteristics in relevant fields due
294 to their large specific surface area, three-dimensional (3D) open structure and superb

295 architectural robustness. It was demonstrated that diverse reactivity between the edges
296 and the plane surface of the bimetallic PBA precursor was crucial for the preparation
297 of NiS nanoframes. As the anions exchange process between the Ni-Co PBA nanocubes
298 and S^{2-} ions prolonged from 0.5 h to 6 h, the morphology of product transformed from
299 nanocubes to nanoframes which involved the continuously changed edges and plane
300 surface of precursors. Unfortunately, rigorous and complicated reaction control (e.g.
301 reactant concentration and reaction rate/time/temperature) was required for high quality
302 NiS production.

303 Cho and colleagues demonstrated a solution infiltration approach to synthesize a
304 series of CuS nanoparticles in/on a three-dimensional Cu-BTC with an ethyl alcohol
305 solution of thioacetamide as the sulfide source under determined reaction time and
306 temperature [95]. The amount of CuS generated in/on Cu-MOF can be modulated easily
307 benefiting from such a construction route. Similarly, inserting desirable constituent into
308 MOF cavity can prepare specific functional materials. Using MOFs-based compound
309 (NENU-5) as precursor, relying on a copper-centered MOF (HKUST-1) precursor as a
310 host and molybdenum-based polyoxometalates (Mo-based POMs) occupied the MOF
311 channels, Wu and colleagues constructed mesoporous molybdenum carbide
312 nanoparticles (MoC_x NPs) by thermal treatment under N_2 flow at 800 ℃ and
313 subsequent Cu NPs etching with $FeCl_3$ solution (Fig. 3) [103]. The as-synthesized
314 MoC_x nanomaterials with octahedral structure composed of ultrafine nanocrystallites

315 with an unusual η-MoC phase embedded in an amorphous carbon matrix showed
316 remarkable electrocatalytic activity.

317 However, considering the high cost of carbonization technology, a facile and low-
318 cost ligand extraction process was proposed to prepare stable and porous inorganic
319 materials with versatile functions. This appealing method focused on replacing organic
320 ligands with inorganic component existing in the digestion solution or directly
321 removing them from MOFs, which enabled the rapid and vast formation of
322 nanomaterials without other fussy synthesis conditions [104]. The resultant inorganic
323 materials can reserve highly porosity and large surface area and retain the morphology
324 of the MOF precursors. For example, highly defective UiO-66-50Benz was used as
325 precursor to fabricate porous oxide (ZrOx), sulfide (ZrSulf) and phosphate (ZrOxyPhos)
326 *via* a wet-treatment process in the presence of NaOH, $Na_2S{\cdot}9H_2O$ and Na_3PO_4,
327 respectively [105]. During the ligand extraction process, the organic ligands were
328 completely removed due to no other weight change except for residual solvent
329 evaporation. The composition analysis demonstrated that nearly 4.2 wt.% of S or 3.5
330 wt.% of P was integrated into ZrSulf or ZrOxyPhos. The obtained three materials
331 inherited the original octahedral morphology but slightly smaller than that of parent
332 MOFs because of the removal of the bridging organic linkers. Using different digest
333 solutions and MOF precursors may yield different metal compounds, suggesting the
334 great promise of this ligand extraction strategy for the preparation of inorganic materials
335 for wastewater treatment. Similarly, Peera et al. reported a simple, ecofriendly and low-

cost mechanochemical coordination self-assembly strategy without solvent to prepare core-shell Co@NC using $Zn_xCo_{1-x}(C_3H_4N_2)$ as precursor [106]. The resultant nanostructures were well-ordered and highly crystalline in nature and showed excellent catalytic activity.

3.1.2 MOF-derived carbons

In particular, porous carbonaceous nanostructures with tunable pore size, highly specific surface area, as well as facile heteroatom doping have been confirmed as promising materials for various applications, which can be produced through pyrolysis of MOFs in inactive gaseous and then by an acid-etching treatment (this process could be skipped if metal center could be *in situ* evaporation). Typically, Zn-centered frameworks are attracting ones and universally chosen as precursors/templates to construct porous carbons because of their simple operation to remove Zn. In detail, high-temperature calcination (> 900 ℃) enables metallic-Zn (boiling point: 907 ℃) to vaporize and is conducive to the formation of MOF-derived porous materials with numerous void spaces [107].

Accordingly, directly carbonizing MOFs without any auxiliary carbon source to obtain highly nanoporous carbons can be achieved due to the tremendous carbon content in MOFs. Carbonization of MOFs *via* single-step procedure greatly simplifies the preparation process. A novel type of hierarchically porous carbon (HPC) with nanostructure was exploited by direct thermolysis of MOF-5 at 950 °C (named HPC-950) [108]. Alternatively, MOF-5 calcined at 540 ℃ (named HPC-540) and subsequent

elution step using HCl solution also implemented to yield carbon product. The results revealed that the pore volume and surface area of prepared carbon heated at 540 ℃ were 0.79 $cm^3 g^{-1}$ and 1266 $m^2 g^{-1}$, which were lower than those of HPC-950 (0.94 $cm^3 g^{-1}$ and 1512 $m^2 g^{-1}$). Obviously, pore size distributions may rely on the temperature during carbonization and this phenomenon can be ascribed to the formation of more micro-, meso- and macropores at relatively high temperature, further leading to higher porosity. The acquired HPC-950 possessed hierarchically porous architectures, high specific areas and partial graphitization, exhibiting excellent adsorption capacity (up to 310 mg g^{-1}) for *p*-nitrophenol.

However, the broad pore size distributions and larger cracks also simultaneously appear owing to the anisotropic shrinkage and lacking carbon sources of MOFs, which may impact their performance in various applications. Consequently, additional carbon source supplement plays a vital part in yielding carbon structure with appropriate pore size. Many organic compounds contained carbon have been utilized as secondary carbon sources for carbon materials generation, such as glucose [109], glycerol [110], phenolic resin [111], and typical FA [112].

In 2008, using MOF-5 as template, Liu and colleagues successfully synthesized porous carbon (NPC) [55]. In this process, FA was infiltrated into the cavities within the MOF-5 frameworks by a vapor phase method and then transformed to polymerized FA (PFA). Next, the PFA/MOF-5 composite was calcined in furnace filled with inert Ar gas under 1000 ℃ (Fig. 4a). The resultant carbon materials showed sheet-like

structure as revealed by scanning electron microscopy (SEM) and high resolution transmission electron microscopy (HRTEM) (Fig. 4b and c). The prepared NPC displayed a favorable Brunauer-Emmett-Teller (BET) surface area (2872 m^2 g^{-1}), closing to the theoretical surface area of a double-sided separated graphitic sheet (2965 m^2 g^{-1}), and excellent hydrogen uptake capacity (2.6 wt.%) at 760 Torr, much higher than that of MOF-5 (1.3 wt.%) at the same conditions. Considering that FA as the toxic, irritant and explosive reagent is extremely detrimental to the human health and environment, sucrose can alternatively serve as a green carbon source during MOF derivatives preparation. For instance, using IRMOF-3 (IR = isoreticular) as a template and sucrose as an additional carbon precursor, the functional NPC materials were synthesized by pyrolysis in a N_2 flow for 6 h under 900 °C [113]. The generated ZnO species in the calcination process were removed after washing with HCl, affording the final NPC samples. It was demonstrated that sucrose as an external carbon precursor resulted in a beneficial influence to the high specific surface area (3119 m^2 g^{-1}) and high micropore volume (1.93 cm^3 g^{-1}) of NPC materials.

Owing to the N-moieties in organic ligands, N-containing carbons derived from MOFs are readily available. The doped N could break the inertness of sp^2-hybridized carbon networks, regulate the electronic structures, and form more active sites [114]. Generally, directly doping heteroatoms in porous carbon materials in the synthesis is defined as *in situ* doping [115]. ZIFs, a class of N-enriched MOFs, comprise transition metal ions (e.g. Zn^{2+} and Co^{2+}) and imidazolate ligands, which can form 3D tetrahedral

399 scaffolds like zeolite topologies. Other than those MOF analogues with carboxyl-
400 ligands, many ZIFs not only show extraordinary chemical and thermal stability, but are
401 rich in N source in imidazolate linkers. Therefore, ZIFs are usually selected as starting
402 precursors to prepare N-doped carbons with superior performances. For instance, Li
403 and colleagues obtained nanoporous carbon from ZIF-8 by one-step carbonization
404 under N_2 atmosphere [116]. At different carbonization temperature, carbons converted
405 from ZIF-8 possessed versatile adsorption capacity. In their work, the produced
406 materials presented optimal adsorption capacity when carbonized at 700 °C, because
407 lower temperature caused the decrease of available pore and relatively higher
408 temperature resulted in the destruction of structure. Compared with samples calcinated
409 at other temperatures, large amounts of defects and more edge modification of N atoms
410 were obtained in NPC-700, which might be responsible for its good adsorption ability.

411 **3.1.3 MOF-derived metal/carbon hybrids**

412 Apart from metal-containing materials and carbon products, their nanocomposites
413 also can be fabricated by pyrolysis of MOFs in an inert gas without acid leaching. The
414 composites can combine the advantageous features of metallic component and carbon,
415 inducing interfacial interactions and synergistic effects, thus further improving the
416 performance in many applications. In reaction process, the metal compounds
417 coated/supported by carbons could promote their stability, decreasing the metal
418 leaching and ensuring the high recyclability. Furthermore, nanocomposites derived

419 from MOFs afford a better distribution of metal-containing particles on the carbon
420 matrix compared to conventional technology [117-119].

421 Metal compounds stabilized on carbons provide an extraordinary enhancement of
422 overall properties. In Yang's research [120], ZnO nanoparticles with hierarchical
423 coalescence were prepared under air atmosphere, while ZnO@C hybrid composites
424 with large surface area were formed during heat treatment under a nitrogen condition,
425 demonstrating calcination atmosphere played a pivotal part in generation of final
426 products. Intriguingly, the resultant materials with unique features showed a different
427 inclination for a particular application. The ZnO exhibited favorable photocatalytic
428 degradation of target dye (almost 98% in 12 h) due to the low recombination rate of
429 photogenerated hole-electron pairs, while ZnO@C displayed a much higher adsorption
430 capacity (nearly 100% within 30 min) for organics ascribed to their high porosity and
431 pore size.

432 Different from loaded metal compounds, isolated single metal atoms uniformly
433 embedded in carbons can extremely promote the atomic utilization and further facilitate
434 the reaction activity. Torad et al. reported a novel approach to construct magnetic Co
435 nanoparticles with nanoporous carbon by one-step carbonization method of ZIF-67
436 [121]. The as-synthesized complex could be recovered and separated effectively from
437 reaction system owing to their strong magnetism. The proposed strategy presented a
438 powerful combination of metallic particles with magnetic response and catalytic
439 activity as well as carbon materials with high porosity and surface area. The graphitic

carbon presented good affinity to aromatic compounds, while the zeolite-like pore structure was adequate for adsorbing toxic metal ions. The high-weight Co nanoparticles located in the carbon matrix uniformly allowed it as an ideal adsorbent for water treatment. The Co/NPC-800 showed a remarkable methylene blue (MB) adsorption ability with the maximum adsorption amounts of 500 mg g^{-1}. Importantly, their method is quite facile and thus convenient for large-scale production.

3.2 Morphology control

Precisely controlling the morphology and structure in nanometer scale is a major motivation for developing MOF-derived functional materials and has been considered as another attracting route to enhance the performance of MOF-derived nanomaterials. MOFs with thermally stable can achieve morphology-preserved thermal transformation in pyrolysis process to obtain versatile structured hybrids [122, 123]. The elaborate tuning of the morphology of MOF derivatives is essential to obtain a robust nanocomposite characterized by ultrahigh porosity, large surface area and more exposed active sites. With great progress developing, many methods such as the construction of hierarchically porous, hollow and/or core-shell nanostructure and 3D materials based on large substrate have been applied for regulating the morphology of MOF derivatives.

3.2.1 Hierarchical porous structure

Porous structure is a basic and common structure among derivatives of MOFs. Featuring high surface area, well-distributed pores and adjustable pore diameter,

nanoporous materials exhibit great superiority in adsorption and catalysis. For example, interconnected hierarchically N-doped porous carbon (IHNPC) with a reticular and typical microporous structures showed a larger pore volume (0.68 $cm^3 g^{-1}$) and higher surface area (912.5 $m^2 g^{-1}$) than precursors, making it beneficial for the 17β-estradiol capture (up to 455.95 mg g^{-1}) [124]. The huge specific surface area and abundant micro/mesopores in carbon materials enable the target molecules to have better chance to access to pores and penetrate into active sites of the carbon matrix, resulting in fast and high adsorption. Besides, Zhang et al. fabricated a morphology-retaining N-doped hierarchical porous carbon material (ZIFC@RUFC) with mesoporous shell and microporous core by a universal synthetic strategy [125]. The ZIFC@RUFC presented a huge surface area of 982 $m^2 g^{-1}$ and total pore volume of 0.70 $cm^3 g^{-1}$ in comparison of ZIFC (713 $m^2 g^{-1}$, 0.41 $cm^3 g^{-1}$, respectively) and RUFC (647 $m^2 g^{-1}$, 0.38 $cm^3 g^{-1}$, respectively) counterparts. Benefiting from highly developed microporosity in conjunction with ordered mesoporosity, the ZIFC@RUFC achieved greater promotion in CO_2 adsorption kinetics and amounts (3.37 mmol g^{-1}) than RUFC (3.10 mmol g^{-1}) and ZIFC (1.89 mmol g^{-1}).

The pore characteristics (e.g. pore shape, pore size and porosity) of MOF derivatives is highly important for various applications. However, due to the lack of understanding of the MOF decomposition mechanism, the control of pore size is insufficient [126]. It is reported the structure and component of precursor have an effect on pore size [127]. Hussain et al. reported three different Zn-containing MOFs (i.e.

MOF-5, ZIF-8 and MOF-74) derived porous ZnO/C nanocomposites by one-step carbonization [127]. The differences of the pore shape/size of these samples can be attributed to their diverse precursor frameworks. MOF-5 with an open pore structure consists of Zn_4O nodes and benzenedicarboxylate linkers. When pyrolysis at 800 ℃ in water vapors saturated Ar flow, the organic linker decomposed and resulted in a little larger micro- and meso-pores. Likely, $Zn–N_4$ with tetrahedral structure in ZIF-8 framework are connected by methylimidazole rings forming spherical hexagonal architectures. Whereas, ZnN_4-imidazole linked in spherical order causes more pore openings with a smaller pore size than that of MOF-5, leading to the higher micropore volume in $ZnO/C_{ZIF\text{-}8}$. Among these samples, $ZnO/C_{MOF\text{-}5}$ displayed the fast adsorption and photocatalytic MB dye degradation activity because of its larger pore diameters and the existence of micro/mesopores, allowing the MB molecules to permeate and access into the porous carbon.

In the research of Ku's group, the relationship between carbonization temperature and pore volume was studied by preparing NCo@CNT-NFT [128]. The pore volume of resultant samples was proportional to the abundant carbon nanotubes (CNTs), more CNTs in a unit mass afforded a higher pore volume. At 600 ℃ , NCo@CNT-NF600 without formation of any CNTs can be obtained, which were contrary to 700, 800, 900 and 1000 ℃ . Subsequently, the same group confirmed that the amounts of introduced guest iron ions exhibited a great influence on the porosity of the prepared samples, which possessed hierarchical porous superstructures (co-existence of meso- and

503 micropores) [129]. With the increasing of Fe content, the pore volume decreases from
504 0.497 (Co@CC) to 0.350 (CoFe5@CC) and 0.301 $cm^3 g^{-1}$ (CoFe10@CC) gradually,
505 and then increased to 0.438 $cm^3 g^{-1}$ (CoFe20@CC) with further increasing the iron
506 amounts, due to the formation of the distinctive hydrangea-like superstructure. In the
507 work reported by Shang et al., the hierarchically porous Co,N co-doped carbon
508 nanoframework (Co,N-CNF)-derived from Zn/Co bimetallic ZIF precursor was
509 synthesized by mesoporous silica ($mSiO_2$)-protected-calcination approach [130]. After
510 remove the $mSiO_2$ outer shell with hydrofluoric acid (HF), the as-prepared Co,N-CNF
511 presented obvious hierarchically porous structure, while the A-Co,N-CNF carbonized
512 without $mSiO_2$ only exhibited mesopores.

513 **3.2.2 Hollow structures**

514 Complex hollow structures play a positive role in various applications because of
515 their sizeable surface area, abundant active sites as well as more sufficiently accessible
516 contact interfaces between reactants for fast mass transport [131, 132]. Compared to
517 the hard-template approaches with tedious procedures for construction of hollow
518 structures, which involved in the preparation of starting template, the filling of organic
519 precursor, pyrolytic treatment and removal of the template, MOF-templated approach
520 greatly simplifies the fabrication steps and gives the obtained hollow structure with
521 open pore channels [133]. Wei and co-workers proposed three pivotal factors for
522 creation of hollow structures [134]: (i) an intensive interfacial interaction of core-shell;
523 (ii) the clearly higher shrinkage degree of the inner core in comparison with the outer

524 shell; (iii) the relatively loose core structures. Above-mentioned theories offer an
525 explicit guide for the exploitation of MOF-derived nanostructures with hollow cavity.
526 Encouraged by the merits of MOF-derived hollow structures, numerous efforts
527 have been dedicated to utilizing this unique architecture in catalysis. For example, the
528 novel $CoFe_2O_4$/CuO (sub)microcages derived from dual-MOF (Fe^{II}-Co
529 PBAs@HKUST-1) with core-shell structure were fabricated by thermal annealing in
530 oxygen-containing atmosphere [135]. The obtained materials showed obvious core-
531 shell hollow structure with a well-defined gap between the inside solid core and the
532 outside shell as well as well-distributed Fe, Cu, Co and O elements. The high catalytic
533 efficiency for the reduction of organic pollutants by $NaBH_4$ could ascribe to the unique
534 yolk-shell hollow shape which offered hierarchical porosity structure and large surface
535 area. Moreover, hollow semiconductor oxide nanomaterials are advantageous in gas
536 sensing by accelerating the surface reaction and the diffusion of gas molecules. Song et
537 al. prepared the $NiFe_2O_4$ microspindles with hollow structure by annealing Ni/Fe MOF
538 in the air [136]. The as-synthesized $NiFe_2O_4$ consist of major nanosize particles and
539 plentiful deep pores in the hollowed-out shells. Acting in synergistic action with the
540 highly BET surface area, abundant oxygen species and unique hollow structure, the
541 high-performance sensor behaved well towards acetone detection. This study provided
542 a promising route to the efficient construction of gas sensors based of MOF-derived
543 semiconductor oxide in future.

3.2.3 Core-shell structure

Core-shell structures have recently attracted intensive attention in view of their distinctive multilevel architecture and wide applications in many fields. Notably, the core-shell structures used for catalysts possess distinct superiorities as follows: (i) enhancement of the catalytic activity by the confinement effect; (ii) increase of the dispersibility by strong synergy within the inside core and the outside shell; (iii) the formed microenvironment in a void space between the shell and the core offers reaction driving force for degradation and adsorption; (iv) the active core within a hollow environment can improves the stability and extends service life while retains their all surface active sites [137, 138]. In general, two common pathways have been used to construct MOF-derived core-shell buildings. One is the predesign of core-shell structures and then by a thermal treatment, including self-template method by creating MOF@MOF precursors, external-template method by creating template@MOF structures and introduction of guest nanoparticles; the other is the direct pyrolysis of pristine MOFs to their core-shell derivates.

MOFs with a similar crystal/topological structure can be facilely fabricated into core-shell architecture. A novel ZnO@C-N-Co nanocomposites with core-shell structure were prepared by directly heating hollow bimetallic Zn/Co-ZIFs comprising a ZIF-8 as shell and some ZIF-67 nanoplates as core at 600 ℃ for 2 h (Fig. 5) [139]. Intriguingly, ZnO nanoparticles derived from ZIF-8-shell could agglomerate spontaneously and transfer to the hollow cavity internally. Whereas, the inside Co

565 nanoparticles inversely moved to the organic ligand-derived outer N-C shell, leading to
566 the final core-shell ZnO@C-N-Co. This unique nanostructure endowed the
567 intermediate ZnO with good stability, high specific surface area, and effective electron-
568 hole separation capacity. The prepared ZnO@C-N-Co exhibited a greatly enhanced
569 photocatalytic activity (99.5%) than pure ZnO (60.2%) for MO due to the strong
570 synergic effect between the ZnO core and C-N-Co shell.

571 External templates such as SiO_2 and polymers are extensively applied for the
572 creation of core-shell structure, in which MOF commonly served as inner core. Zhang
573 et al. reported yolk-shell Co_3O_4/C@SiO_2 nanoreactors (YSCCSs) for PMS activation
574 (Fig. 6a-h) [140]. This hybrid with rational morphology and composition exhibited
575 outstanding degradation effect of BPA compared to YSCSs (pyrolysis in air), Co_3O_4
576 and MOF-derived Co_3O_4/C NPs (Fig. 6i). It is noting that the superior catalytic activity
577 of YSCCSs can be attributed to their structure and composition optimization (Fig. 6j).
578 Specifically, the confinement effect of yolk-shell nanoarchitecture and good dispersity
579 of Co_3O_4 species improved the stability and catalytic performance; and the presence of
580 graphitized carbon promoted the reaction kinetics because of the facilitation of electron
581 transport from catalyst to oxidant.

582 Various porous core-shell morphologies of MOF-derived metal oxide
583 semiconductors exert an important impact on the gas detection. Zhang and co-workers
584 constructed four kinds of ZIF-67-templated porous hierarchical Co_3O_4 structures (*i.e.*
585 nanoparticle Co_3O_4 (NP-Co_3O_4), porous core-shell Co_3O_4 (PCS-Co_3O_4), porous

586 popcorn Co_3O_4 (PPC-Co_3O_4) and core-shell Co_3O_4 (CS-Co_3O_4)) (Fig. 7a-e) [141].
587 Benefiting from the elaborate architecture, ZIF-67-derived Co_3O_4 materials offered a
588 sufficient exposed surface and active sites, which could be the reactive locations for the
589 pre-adsorbed reducing analytes and O_2. These obtained samples with mesoporous
590 structure were beneficial to access and departure of target gas on the materials surface,
591 further promoting a fast mass transfer. Among them, Co_3O_4 with core-shell structure
592 showed the superior performance owing to its multilevel architecture, which could hold
593 a stable structure as well as provide a large contact area between the target gas and
594 surface regions of materials (Fig. 7f). In another study, NH_2-MIL(Fe)-88B-derived
595 nano-ZVI@C-N was prepared through annealing the MOF precursor for 4 h under N_2
596 flow [142]. The presence of core-shell nano-ZVI and Fe_3O_4 NPs distributed along N-
597 doped fusiform porous carbon rods ensured the conversion of Fe(III) to Fe(II),
598 achieving 95% drug removal during 60 min in heterogeneous electro-Fenton process.

599 **3.2.4 Three-dimensional monolithic materials**

600 Despite the great success of powdery nanomaterials derived from MOFs, most of
601 them undergo numerous drawbacks, such as weak durability, difficult separation from
602 reaction system, and easy-clogging of the pipes, which largely thwart their practical
603 demand. In view of the recycling problems in industrial operations, MOF-derived
604 functional materials integrated with 3D monolithic substrates or support have gained
605 increasing attentions. Lin's group investigated a new concept to employ a self-assembly
606 of melamine sponge and cobalt-centered ZIF-67 to yield a magnetic carbon sponge

607 (MCS) by one-step carbonization (Fig. 8a) [143]. After calcination, the layer of
608 melamine sponge coated with ZIF-67 converted into a layer of nanoscale cobalt/carbon
609 hybrid immobilized on carbon sponge. Such carbon material with 3D monolithic
610 structure showed not only nanosize porosity of carbonized ZIF-67 and macroporous
611 carbon sponge but magnetic features of cobaltic components. The proposed synthetic
612 strategy of 3D hierarchical carbon materials can be further explored by using versatile
613 MOFs.

614 Su et al. reported a simple dipping-pyrolysis method to fabricate a unique 3D
615 architecture photocatalytic microreactor, where the hollow ZnO nanocages derived
616 from ZIF-8 were steadily and uniformly distributed in the overall surface of carbon
617 sponge networks coated by rGO (Fig. 8b) [144]. The as-prepared porous ZnO based of
618 carbon frameworks displayed superior adsorption and degradation performance for
619 water pollutants. The rhodamine B (RhB) degradation efficiency was as high as 99% in
620 120 min and better than ZnO_{ZIF-8}/carbon sponge without rGO (89%) and pristine carbon
621 sponge (more than 20%). Owing to the good recyclability, robust structure and
622 convenient maneuverability, the microreactors have great potential in sustainable
623 environmental remediation towards industrial photocatalytic applications. In addition
624 to carbon sponges/foams, cellulose aerogels, ceramics, ion-exchange resin and so on
625 also can be developed as efficient anchor [145-147]. Such an elaborate design and novel
626 strategy can be expanded to a wider series of 3D bulk supported with MOF-derived
627 porous materials.

To sum up, versatile morphologies and structures of MOF-derived nanomaterials affect their properties seriously and hence lead to different removal efficiency for organic contaminants. Rational regulation of the morphology and structure endow these derivatives with highly porosity, large surface area, abundant reaction locations and suitable pore sizes, which can enhance the adsorption capacity of functional materials and create the chances for targeted molecules to close to the active sites, further facilitating the catalytic efficiency. Therefore, more representative researches for deeply analyzing the relationship between the structures and the physical and chemical features of MOF-derived nanoscale materials are highly desirable.

3.3 Pre-synthetic modulation

Owing to the unique structure of MOFs, various approaches to modulate the active metal nodes, active linkers and/or incorporate active guest into the pore channels of MOFs before calcination have been employed. In this section, several methods related to pre-synthetic modulation are proposed emphatically: (i) introduction of heteroatoms through external template; (ii) modification of MOFs with functional groups; (iii) addition of extra activating agent; (iv) MOFs loaded/coated with other materials; (v) encapsulation of guest into MOF cavities.

Notably, introduction of heteroatoms such as nitrogen (N), phosphorus (P), sulfur (S), oxygen (O) or boron (B) into carbon frameworks can effectively enhance their physico-chemical features [148-150]. Doping heteroatoms into carbon-based materials derived from MOFs can (i) promote π-electron mobility through conjugation, (ii) offer

649 more active sites for selective adsorption, and (iii) increase the defective edges and
650 surface hydrophilicity [151-154]. These features highly promote the catalytic activity
651 of carbon nanomaterials for refractory organic contaminants. For example, modified
652 HKUST-1 with triphenylphosphine (TPP) was utilized for construction of carbon
653 supported Cu_2O heterostructures doped with phosphorus [155]. Carbon materials doped
654 with P can enhance the electrical conductivity, surface area, possible catalytic sites and
655 mitigate the steric hindrance effects encountered in N-doped carbon materials [156].
656 This obtained carbon-based heterostructure showed superior photocatalytic activity for
657 phenol decomposition, which was up to 99.8% within 90 min. The P-doping was
658 advantageous in facilitating charge carrier separation and developed a synergistic effect
659 with carbon/Cu_2O towards promoting charge transport to the catalyst surface, thus
660 resulting in the enhancement of photocatalytic degradation performance.

661 N-doped carbon nanomaterials have attracted extensive research. In addition to
662 obtaining N-containing carbons by *in situ* doping, thermal treatment of MOF precursors
663 with external N-source is another method to synthesize such materials, peculiarly those
664 MOFs without any N-moieties in organic linker. In the research of Aijaz, highly N-
665 decorated nanosized porous carbons were synthesized through using ionic
666 liquids@MIL-100(Al) (IL@MIL-100(Al)) as the precursors, in which the IL (1-ethyl-
667 3-methylimidazolium dicyanamide (EMIM·DCN)) was served as the external N source
668 [157]. Particularly, ILs were impregnated into the as-prepared MIL-100(Al), and
669 calcined at 800 °C for 7 h in argon flow. Then, the resultant samples were washed with

HF to remove the Al_2O_3 species generated in carbonization, which afforded the final carbon materials. The nanoporous carbons displayed large surface area (2397 m^2 g^{-1}) and high N amounts (14.8 wt.%), where overall the N moieties came from the IL because the MOF precursor is free of N atoms, suggesting the achievement of efficient heteroatom doping from external template.

In reality, co-doped or tri-doped carbon materials may show good enhancement than monotonous N-doped carbon catalysts because of the possible synergy between multiple kinds of heteroatoms. Ma el al. successfully prepared N (8.09 at.%), P (0.69 at.%), and S (0.80 at.%) co-doped hollow carbon shells (NPSC-700) using poly (cyclotriphosphazene–co-4,4′-sulfonyldiphenol) and Co-centered MOF as precursors [158]. The NPSC-700 showed much better bisphenol A (BPA) degradation efficiency than N-doped CNTs, N-doped GO as well as N-doped mesoporous carbon, which suggested that N-doped carbons were far from enough to degrade model compounds, but introduction of P and S definitely broke the electroneutrality of sp^2 carbon and provided more charged sites for organics decomposition. The positive synergistic effect of N, P and S in carbon materials regulated the polarizability, the spin density and structural defects, facilitating the O–O cleavage of PMS and thus accelerating the formation of radicals. Likely, Jin et al. reported that Fe, N and S co-doped carbon matrix/carbon nanotube nanocomposites derived from ZIF-8 showed superior electrocatalytic activity in light of the synergy of carbon nanotubes and matrix, thiophene-S active sites and adequate iron nitrides [153].

691 The introduction of functional groups (e.g. CH_3, NH_2, NO_2, OH, Cl and SH) into
692 MOFs and subsequent pyrolysis has raised increasingly research interests, which could
693 intensively improve their chemical durability and property. Particularly, amino groups
694 as electron donator have been widely used due to their interactions with π*-orbitals of
695 the ligand benzene ring [159]. For example, Liu et al. synthesized a NH_2-functionalized
696 carbon material using MOF-5 and tetraethylenepentamine (TEPA) by a fast approach
697 in high temperature [160]. The introduction of amino groups could obviously promote
698 the adsorption property of the products. 20% TEPA-C-MOF-5 showed the best capture
699 amounts (550 mg g^{-1}) for U(VI), better than that of 10% TEPA-C-MOF-5 (342 mg g^{-1})
700 and raw MOF-5 (160 mg g^{-1}), which was because U(VI) could be coordinated with a
701 large number of amino groups. In another case, single Ru sites derived from UiO-66-
702 NH_2 was prepared by Li et al. for selective hydrogenation of the quinoline [161]. The
703 amino group of UIO-66 ligands served as the Lewis base to stabilize $RuCl_3$, allowing
704 the confinement of the single Ru atom into the MOF channels.
705 A mild chemical activation with potassium hydroxide (KOH) was proved as
706 another routine to improve the textural property of nanomaterials derived from MOFs
707 [162-164]. Pyrolysis of MOFs along with KOH (as an activator) could greatly increase
708 the surface area and porosity of as-synthesized carbon, broadening its various potential
709 applications. For instance, MAF-6 (MAF = metal azolate framework, a kind of Zn-
710 based MOF) was heated with KOH under a wide range of conditions to fabricate porous
711 carbons [164]. The porosity of obtained carbons depended a lot on the concentration of

712 incorporated KOH, while the pore size was controlled by the pyrolysis temperature.
713 The KOH activator might generate K_2CO_3 and then dissociate into CO_2, CO and K_2O
714 to eliminate carbons [165], and this process primarily enhanced the present porosity
715 instead of creating new larger pores. Benefiting from the presence of KOH, the defect
716 phase and specific surface area (from 1484 to 3123 $m^2 g^{-1}$) of resultant porous carbons
717 both increased. The maximum adsorption capacities of CDM6-K1000 for ibuprofen
718 and diclofenac sodium separately were 408 mg g^{-1} and 503 mg g^{-1}, much higher than
719 those of commercial active carbon (AC) (168 mg g^{-1} and 79 mg g^{-1}, respectively).
720 The assembly of MOFs onto diverse substrates (e.g. graphene, CNTs and g-C_3N_4)
721 has achieved extensive interests in many fields. Gong et al. synthesized a novel Zn-
722 centered MOF-derived N doped carbon (ZIF-NC) loaded on g-C_3N_4 heterostructure by
723 a two-step calcination approach [166]. The integration of ZIF-NC with g-C_3N_4 not only
724 enhanced the light harvesting but also facilitated the activation of PMS to generate high
725 active $SO_4^{\bullet-}$ radicals. Besides, the formation of junction between ZIF-NC and g-C_3N_4
726 could greatly accelerate charge transfer and shorten the charge transport distance,
727 leading to acceleration of the photogenerated carrier separation. 0.5% ZIF-NC/g-C_3N_4
728 with PMS exhibited the excellent photocatalytic performance with removal rate of 97%
729 within 60 min irradiation, much higher than that of g-C_3N_4 and ZIF-NC counterparts.
730 MOFs coated/doping with polymer exhibited outstanding electrocatalytic performance
731 owing to the fabrication of hierarchically porous nanostructures and more exposure of
732 active sites. Zhang et al. prepared N-doped hierarchical carbon (NDHC) catalyst by

733 using ZIFs coated with phenolic resin (PR) as precursors (Fig. 9) [167]. The
734 confinement effect of PR led to a NDHC catalyst with ample active N sites, well-
735 distributed porous structure and high graphitization. The resultant NDHC-9 possessed
736 a uniform dodecahedron (Fig. 9b), suggesting that the encapsulation of PR enabled the
737 carbon framework more stable in pyrolysis. Besides, many macro- and meso-pores
738 presented in the inner and outside of NDHC-9 (Fig. 9c), resulting in more exposed
739 graphitic N active sites.

740 The nano-cavity of MOFs can afford good space to accommodate guest species to
741 fabricate the guest@MOFs, which can be employed as platforms for host-guest
742 chemistry researches and precursors for functional materials preparation. The rational
743 encapsulation of guest species into the pore channels of MOFs can formulate versatile
744 derivatives as required. A novel designed cage-containing MOF as a host and
745 dicyandiamide (DCDA) and iron precursors as introduced guests was used for
746 synthesizing N-Fe-MOF catalysts by a high-temperature route (Fig. 10a-c) [168]. In
747 this study, the morphologies and properties of prepared samples greatly relied on the
748 heating temperature. When heated at 800 ℃ , graphitized carbon structures together
749 with Fe_3O_4, residual Fe, and Fe_3C crystallites were yielded (Fig. 10d). As the
750 temperature increased to 900 ℃ , carbon nanotube structures with visible metal particles
751 at the end appeared due to the release of large amounts of carbon nitride gases (e.g.
752 $C_2N_2^+$, $C_3N_2^+$, $C_3N_3^+$) generated from decomposed N-containing polymer evolved from
753 DCDA. During treated at 1000 ℃ , the graphene/graphene tube-like nanocomposites

754 became dominant because of the direct graphitization of DCDA and catalytic unzipping
755 of *in situ* generated graphene tubes. However, further elevating the heating temperature
756 to 1100 ℃ resulted in unevenness morphology along with numerous agglomerated
757 particles.

758 Likely, in Pan's research, the active site K^+ was *in suit* introduced into the channels
759 of bio-MOF-1 precursors through an ion-exchange strategy to prepare N-doped
760 hierarchical porous carbons [169]. Bio-MOF-1 possesses a rigid anionic skeleton with
761 $Me_2NH_2^+$ cations as counter ions in the pores, which could be easily exchanged with
762 K^+. During the carbonization process, the K^+ exchanged into the bio-MOF-1 scaffolds
763 exerted an great influence in the porosity development, where carbon scaffold was
764 removed by potassium carbonate, and then the formed K_2CO_3 decomposed into K_2O
765 and CO_2, which was closely related to the generation of additional microporosity. The
766 KBM-700 derived from K@bio-MOF-1 showed the highest pore volume (0.55 $cm^3\ g^{-1}$)
767 and specific surface area (1129 $m^2\ g^{-1}$), nearly two-fold larger than that of the bio-
768 MOF-1-derived BM-700 (0.50 $cm^3\ g^{-1}$, 682 $m^2\ g^{-1}$, respectively). These results
769 suggested the good distribution of K^+ in the bio-MOF-1 framework led to homogeneous
770 and effective chemical activation without any additional activating agent.

771 These methods associated with the pre-synthetic modulation abovementioned are
772 not completely independent. In some cases, they can be utilized simultaneously to
773 dramatically enhance the performance of materials. For example, Koo and co-workers
774 constructed Pd@ZnO-WO_3 nanofibers (NFs) by electrospinning and then by

calcination in air for toluene sensing (Fig. 11), where ZIF-8-derived Pd-loaded ZnO nanocubes were functionalized on the inside and outside of the WO_3 NFs [170]. At first, Pd nanoparticles encapsulated in ZIF-8 cavities to construct metal@MOF templates, and then the as-prepared Pd@ZIF-8 particles were directly employed to decorate the ammonium metatungstate hydrate/polyvinylpyrrolidone composite nanofibers (AMH/PVP NFs). At last, the final product was acquired by calcination of Pd@ZIF-8/AMH/PVP composite NFs at 500 °C under air flow for 1 h. The well-distributed Pd and Zn in the Pd@ZnO-WO_3 NFs resulted in homogeneous sensitization both internal and external of the WO_3 matrix. Moreover, the formed mesopores within the WO_3 scaffold were on account of the burning-out of the organic ligands in MOFs. Multi-heterojunctions were created within the one dimensional composite NFs by the formation of ZnO-WO_3 and Pd-ZnO interfaces. Liu et al. fabricated a unique Fe@N-doped graphene-like carbon by using g-C_3N_4 and NH_2-MIL-53(Fe) as the precursors for 4-aminobenzoic acid ethyl ether and sulfamethoxazole (SMX) removal [171]. The g-C_3N_4 and NH_2 groups as N source not only endowed the obtained samples with the stability of framework morphology and phase composition but the remarkable improvement of PMS activation performance. Besides, the addition of g-C_3N_4 also increased the surface area.

3.4 Post-synthetic treatment

Post-synthetic treatment is a wonderful strategy to modify derivatives of MOFs with diverse functionalities, in which the MOFs after pyrolysis could form favorable

796 nanocomposites through integrating with other advance nanomaterials. Selecting
797 different active atoms or compounds to combine with MOF-derived materials for on
798 demand seems to be more conducive to the target reaction. Typically, hierarchical
799 porous carbon nanoplates (HPCN) were prepared by a one-step calcination method of
800 MOF-5, and then the obtained HPCN further encapsulated by active sulfur to prepare
801 HPCN-S composite [172]. HPCN with outstanding conductivity, large surface area and
802 well-distributed pore-size was proved to immobilize sulfur by capillary force of its
803 pores and as an impressive candidate to improve the sulfur utilization. The HPCN-S
804 composite with well-defined 3D porous plate nanostructure exhibited enhanced
805 electrochemical performance and excellent cycling stability.

806 More recently, hollow tubular-like carbon coated metal sulfide (C-$Cu_{2-x}S$) by
807 using a copper-based MOF as precursor was designed through sulfidation and
808 calcination, Subsequently, C-$Cu_{2-x}S$ mixed with graphitic carbon nitride (g-C_3N_4) upon
809 heating to form a novel three-component heterojunction (C-$Cu_{2-x}S$@g-C_3N_4) [173]. As
810 we know, g-C_3N_4 has the fast recombination rate of photogenerated electron-hole pairs
811 and limited visible light adsorption [174-176]. Such features restrict its further
812 development and wide application. The combination of Cu_2S and carbon layers with
813 strong synergy showed satisfactory light-absorbing property and effective charge
814 separation, facilitating the photocatalytic activity.

815 Jang et al. first introduced a method to prepare n-SnO_2 nanocubes (HNCs) with
816 hollow polyhedron through combining MOF-templated route with galvanic

817 replacement reaction (GRR) (Fig. 12) [177]. During this process, n-SnO_2 HNCs were
818 yielded from p-n transition of ZIF-67-derived p-type Co_3O_4 (p-Co_3O_4) hollow cubes.
819 In detail, Pd NPs were embedded in ZIF-67 network and then the formed MOF@Pd
820 was calcined for 1 h under 400 °C to acquire PdO loaded Co_3O_4 HNCs. For the GRR
821 procedure, Sn^{2+} ions were induced into the mesoporous of PdO loaded Co_3O_4 HNCs,
822 where the Co_3O_4 surface was dissolved into solution and Sn^{2+} ions were transformed
823 into SnO_2 by the precipitation, leading to the formation of Co_3O_4-PdO loaded n-SnO_2
824 HNCs. The successful functionalization of n-SnO_2 HNCs by co-catalysts (PdO NPs and
825 discrete Co_3O_4 islands) showed enhanced acetone sensing compared with the general
826 ZIF-67 templated p-Co_3O_4 hollow structures.

827 Obviously, many monomers or complexes can be utilized to form hybrids with
828 MOF-derived produce in a variety of ways, such as impregnation of guest into
829 framework cavity, load with support and so on. Integrating calcinated products with
830 other substances can improve their dispersity and stability as well as inhibit the leaching
831 of toxic metal ions to some extent. Within such kind of composites, each component
832 with special function possesses enhanced performance compared to individual
833 counterparts, which can greatly improve the reaction activity. It is worthy of expecting
834 that more functional nanomaterials can be synthesized and designed for on demand by
835 using calcinated MOFs as one of the component units, which could afford great
836 opportunity to construct fascinating hybrid structures with unique characteristics and
837 ideal functions for environmental field. However, note that much more endeavor should

be paid to simplify the post-methods procedures, minimize the damage to the structures of MOF derivatives, and adopt eco-friendly approaches.

4. Environmental applications of MOF-derived nanomaterials

With the rapid development of urbanization and industrialization, the earth is suffering unprecedented destruction. Global warming, resources depletion, and species loss are the grave warnings to mankind by our planet, which has become a high priority global concern. Protecting the environment has been regarded as an greatly urgent and important task for each of us. MOF-derived nanomaterials with numerous advantages have been applied in many areas successfully such as supercapacitor [178], lithium-ion battery [179], drug delivery [180], etc. Nowadays, these hybrids as excellent function materials show amazing potential in environment-related fields. The use of these materials for environmental remediation and contaminant detection is an exciting progress, as evidenced by a growing body of researches. In this section, MOF-derived nanomaterials for wastewater treatment, air purification, and target pollutant sensing are discussed emphatically.

4.1 MOF-derived nanomaterials for wastewater treatment

4.1.1 Adsorption

Enormous efforts have been devoted to removing environmental pollutants from water, and various technologies used for controlling wastewater pollution have emerged, such as chemical oxidation, coagulation-flocculation, membrane technology, and adsorption [181-183]. Among them, adsorption method is a priority option owing to a

859 comprehensive consideration of operational feasibility, cost rationalization, procedures
860 simplification, and removal efficiency. MOF-derived nanomaterials as a new type
861 adsorbent are advantageous in this process. Furthermore, scalable fabrication provides
862 more possibilities for the industrial-level production. Some representative MOF-
863 derived adsorbents and their corresponding performance are listed in Table 1.

864 Noticeably, understanding the adsorption mechanism is important not only for
865 knowing the basics of adsorption but also for improvement of the adsorption technology
866 and further development for commercialization. For physical adsorption, van der Waals
867 interaction usually regarded as primary mechanism when there are no specific
868 adsorption sites to form any chemical interaction between adsorbate and adsorbent
869 [184]. In general, the porosity and surface area of the adsorbents commonly affect the
870 adsorption capacity by van der Waals interaction. With respect to chemical adsorption,
871 the effect of solution pH on the adsorption is often employed to comprehend the
872 probable adsorption mechanisms, as pH has a profound influence on the status of
873 adsorbent and adsorbate [185]. Electrostatic interaction has been frequently utilized to
874 elucidate the adsorption of organics/aromatics from water, which is greatly related to
875 the dissociation constants of adsorbate and the zero-potential point of adsorbent [186].
876 The presence of various functional groups on adsorbent or adsorbate is very important
877 for H-bonding. The direction of the H-bond (H-donor and H-acceptor) can be
878 determined *via* investigating the effect of solution pH on the adsorption. Typically, the
879 H atoms in the ample acidic groups especially carboxylic and phenolic groups on

adsorbent can serve as H-donors to promote the targets adsorption through H-bonding with the O-atoms or N-atoms [187]. π-π interaction as another vital mechanism for adsorption occurs between the aromatic ring of aromatic compounds and the graphitic layer of carbons [188]. Hydrophobic interaction should be considered when adsorbent and adsorbate both are hydrophobic. Besides, the surface complexation is significant for the adsorption process of metal ions, during which the presence of numerous functional groups in adsorbent can effectively bind with metal cations to form surface complexes [189]. Actually, these interactions usually take place synergistically. In short, exploring the adsorption mechanism is essential to improve the adsorptive performance.

Carbonaceous nanomaterials derived from MOFs are widely used as adsorbents because of their high porosity, adjustable pore volume, large surface area, uniformed pore size distribution and heteroatomic doping. For example, a highly porous carbon derived from bio-MOF-1 was applied in the adsorptive process for removing four pharmaceuticals and pharmaceutical and personal care products (PPCPs) [190]. The maximum adsorption ability for acidic clofibric acid (CLFA; 540 mg g^{-1}) and basic atenolol (ATNL; 552 mg g^{-1})over BMDC-12 h were almost 2 and 10 times those of the commercial AC, making it superior to most reported adsorbents. ATNL adsorption can be explained by electrostatic interaction, and CLAF adsorption is dominated by H-bonding, in which CLAF and porous carbon serve as H-acceptor and H-donor, respectively. Similarly, ZIF-8-derived carbonaceous materials (MDC-1000) reported by Ahmed et al. exhibited incredible BET surface area (1964 m^2 g^{-1}) and pore volume

(1.32 cm^3 g^{-1}), which were much better than that of parent MOF and AC [191]. The maximum adsorption capacities of MDC-1000 for SMX were 435 mg g^{-1}, almost 20-fold higher than that of original MOF and 4-flod higher than that of AC. H-bonding can be adopted to reveal the adsorption mechanism based on the effect of the solution pH and the zeta potential of MDC.

In addition, pyrolysis of MOFs with additional carbon sources can extremely enhance the adsorption ability due to the increased specific surface area and optimal porous structure. As a typical example, Xu et al. synthesized three MOF-derived N-doped porous carbons for MB adsorption by carbonized ZIF-8 (carbon-Z), ZIF/sucrose (carbon-ZS) and ZIF/dicyandiamide (carbon-ZD), respectively [192]. Carbon-ZD not only possessed an incredible BET specific surface area of 1796.5 m^2 g^{-1} but also a micro/mesoporous structures, while other two materials only contained the microporous. In this process, micropore was advantageous for MB molecules adsorption and mesopore was conducive to MB diffusion and adsorption. Owing to high electronegativity of nitrogen, the N-doped carbon-ZD enabled the surface charge of carbon matrix redistributed, which extremely promoted the surface affinity for MB pollutant. As a result, carbon-ZD showed the best adsorption capacity of as high as 1148.2 mg g^{-1}, by comparison of carbon-Z (505.3 mg g^{-1}) and carbon-ZS (791.3 mg g^{-1}).

In contrast to carbons, the examples of pure metal compounds as adsorbents came from MOFs were relatively less owing to their limitations such as inevitable

aggregation and low activity after reuse. A novel porous Al_2O_3 microsphere (P-Al_2O_3 MSs) was applied to immobilize radionuclides (U(VI) and Eu(III)) from wastewater, which showed ultrafast and high adsorption in this process and performed much better than the commercial γ-Al_2O_3 nanomaterials [193]. As shown in Fig. 13a-c, P-Al_2O_3 displayed a smooth surface and the hierarchical structures with high surface homogeny. The optimal adsorption capacity of P-Al_2O_3 MSs reached 316.87 mg g^{-1} and 223.37 mg g^{-1} for U(VI) and Eu(III) within 25 min, respectively (Fig. 13d and e). The rapidly adsorption could be benefited from the porous characteristics of P-Al_2O_3 and thus resulted in the easy collision between binding sites with target ions. The coexisting cation ions exhibited an obvious decrease to Eu(III)/ U(VI) adsorption capacity, while a slight influence indicated by anions ions except CO_3^{2-} and PO_4^{3-}, which could generate complexes with UO_2^{2+} and Eu_3 in many water body (Fig. 13f and g). The numerous hydroxy groups were found to play a vital role for the capture of radionuclides to P-Al_2O_3 because these functional groups were capable of binding target ions and forming surface complexes. Li et al. reported porous ZrSulf for the adsorptive removal of Hg(II) and its uptake capacity reached 824 mg g^{-1}, because of the accessibility of sulfur-based functionality and the formation of covalent bond with sulfur-based functionality combined with Na by ion exchange, making it superior to majority of other reported porous adsorbents [105].

Combined solid particles with carbon materials can attain the enhanced advantages than individuals and effectively overcome the aggregation of nanoparticles. Lv et al.

943 reported a hollow sphere NiOx/Ni@C400 composite with chestnut shell-like structure
944 by Ni-MOF-template method (Fig. 14a), which showed excellent adsorption amount to
945 As(V) (454.94 mg g^{-1}), higher than that of parent Ni-MOF (133.93 mg g^{-1}) and other
946 obtained samples at different pyrolysis temperature (Fig. 14b) [194]. The favorable
947 adsorption ability could be attributed to the high specific surface area as well as the
948 abundant oxygen-containing functional groups of resulting adsorbents. Two aspects
949 involved in surface complexation (As-O bond) and electrostatic interaction were
950 confirmed as the main adsorption mechanism. The as-synthesized samples not only
951 exhibited a good applicability in a wide pH range from 1 to 10 and hardly were affected
952 when coexisting with other anions (Fig. 14c and d), but also a good separating ability
953 due to the high magnetization intensity. Furthermore, Xiong et al. prepared magnetic
954 carbon-αFe/Fe_3C 910 and used it for tetracycline (TC) adsorption [195]. The obtained
955 samples showed increased BET surface area (171.715 m^2 g^{-1}), pore volume (0.312 cm^3
956 g^{-1}) and mesoporous volume (0.260 cm^3 g^{-1}) than original Zn-MIL-53(Fe) (46.990 m^2
957 g^{-1}, 0.105 cm^3 g^{-1} and 0.086 cm^3 g^{-1}, respectively). These improved physical properties
958 provided more active adsorption sites and weakened the steric hindrance effect, thus
959 facilitating the adsorption process. Pore filling effect controlled the physical adsorption
960 due to the homogeneous pore size distribution, while electrostatic interaction induced
961 by the change of pH value played a dominant part in chemical adsorption.

962 A number of adsorption mechanisms such as acid-base, electrostatic, hydrophobic,
963 H-bonding and π-π interaction can be adopted to explain the uptake process where H-

bond interaction is suggested as the primary reason for the high adsorption [196-198]. Based on the above discussion, those derivatives with unique structures require special attention. Besides, the adsorptive efficiency was mainly dependence on the heteroatom doping (e.g. N and/or O species) and the surface properties (e.g. BET area, pore volume and porosity) of adsorbents on the basis of large studies [199, 200], which may be regulated by adding external template or activating agent. However, the effect of heteroatoms was not distinctly verified, more deep studies are need for the understand of adsorption mechanism. Large surface area and pore volume can facilitate material transfer and provide more exposure of active adsorption sites, thus enhancing the capture capacity. The pore size has an important effect on adsorption ability, which partly depends on the species of target pollutants. For example, micropore is beneficial to the MB adsorption, while mesopore is advantageous to TC capture [195, 201]. However, the control method of pore size is still unclear. Notably, the micropore-dominated porous structure has an intrinsic drawback of limited diffusion [202]. In short, developing nanomaterials with admirable functionalities using MOFs as precursors could provide an effective pathway to increase their adsorption competitiveness in both academic research and industrial application.

4.1.2 Catalytic degradation

Recently, MOF-derived nanomaterials have been employed as great catalysts towards versatile catalytic process for contaminants elimination. The large surface area of MOF derivatives provides more exposure possibilities of active sites. The tunable

pore size and retained morphology contribute to optimize the catalytic performance. Such advantages of MOF-derived hybrids can promote the catalytic efficiency dramatically and make them as highly attractive candidates for environmental catalytic reactions. In general, photocatalysis, Fenton-like catalysis and PS/PMS activation are studied extensively, thus the following description mainly develop around these catalytic processes. Table 2 summarizes some representative works in catalysis.

In recent years, MOF-derived nanocomposites as emerging heterogeneous catalysts show promising performance in photocatalysis. These hybrids possess great competitive strength no matter in composition or structure compare to traditional photocatalysts. Specifically, MOF with diverse metal center can be directly converted into semiconductors such as metal oxide and metal sulfides. In addition, the doped heteroatom of derivatives can be obtained from organic linkers with no need for extra additions. With respect to their structure, ultrahigh porosity and distinctive monophony accelerate the contact between reactant and charge carriers, thereby effectively restricting the recombination of photoinduced electron-hole pairs. Under UV/visible light irradiation, excitons e^-_{CB}/h^+_{VB} are formed by the absorbed photons in conduction band (CB) and valance band (VB) of photocatalysts respectively. In the case of thermodynamics, the photo-generated electrons could effectively reduce oxygen molecules into $\bullet O^{2-}$ and the holes left in VB can react with H_2O or OH^- to generate •OH. On the other hand, the holes, with strong oxidative capacity, can directly induced the photo-oxidation of target contaminants [203]. These highly active species play an

1006 important role in the photocatalytic degradation process. A large number of researches
1007 have proved that improving the optical and electronic characteristics of photocatalysts
1008 such as enhancing the light harvest ability, prolonging the lifetime of the separated e^-/h^+
1009 pairs, and facilitating the transfer of charge carriers are of great significance for the
1010 photocatalytic process [204-207].

1011 ZnO particles or clusters are suggested as the suitable photocatalysts due to their
1012 high electron mobility and thermal stability [208]. Considering that, Liang et al.
1013 synthesized carbon and nitrogen co-doped ZnO from ZIF-8 for MB degradation under
1014 solar-simulated light [209]. The obtained sample achieved almost complete removal of
1015 target pollutant within 90 min, better than commercial ZnO. The optimization could be
1016 attributed to their well-crystalline and proper contents of carbon/nitrogen dopants.
1017 Besides, the oxygen vacancy also played a positive role in the photooxidation process
1018 *via* inhibiting the recombination of electrons and holes. Xiao et al. used Zn-free MOF
1019 like MIL-53(Al) or MIL-125(Ti) to prepare ZnO nanosheets for MO photodegradation
1020 [210]. After calcination at 400 °C, MIL125-ZnO^{400} exhibited a nanoplate or flaky
1021 structure with a little amount of ultrafine nanosheets. Differently, MIL53-ZnO^{400}
1022 showed the same shape but with much more ultrafine nanosheets (Fig. 15a and b).
1023 While ZnO-TF^{400} (prepared without addition of any MOFs) presented the six square
1024 prism morphology (Fig. 15c). These Zn-free MOF not only served as a sacrifcial
1025 template but also as a provider of doping metal atom. The resultant ZnO showed low
1026 content of Al or Ti < 2%, and their properties were significantly different depending on

1027 the type of MOF precursor, which affected the morphology, the specific surface area,
1028 the pore characteristics and the oxygen defects of as prepared ZnO. The MIL53-ZnO^{400}
1029 and MIL125-ZnO^{400} showed a better photocatalytic activity with removal rate of 98.15%
1030 and 96.89% than ZnO-TF^{400} (83.10%) prepared without MOF as well as a higher rate
1031 constant within 60 min irradiation (Fig. 15d and e). Such a method opens a new route
1032 of broad scope for the synthesis of metal oxides by MOF-template.

1033 Based on the better properties of multiple components heterojunction materials, a
1034 visible-light-active CoP/Fe_2P@mC was prepared and utilized for RhB degradation
1035 [211]. The nanocomposite with suitable bandgap structure showed enhanced visible
1036 light harvesting ability. In this process, the CoP/Fe_2P@mC catalyst displayed 97%
1037 degradation efficiency for dye molecular, much higher than that of Co/Fe-MOF (9%),
1038 CoO_x/FeO_x@mC (4%), CoP@mC (49%), and Fe_2P@mC (17%) nanocomposites.
1039 CoP/Fe_2P@mC with the highest photodegradation ability exerted powerful synergistic
1040 effect for RhB destruction through combing the rapid electron transfer of CoP@mC,
1041 effective electron-hole separation of Fe_2P@mC, and the excellent adsorption ability of
1042 mesoporous carbon. Moreover, the TOC removal rate of RhB achieved around 67.4%
1043 by CoP/Fe_2P@mC. The catalyst dosages increased from 50 mg L^{-1} to 200 mg L^{-1} not
1044 only can promote the degradation rate, but also increase the reactive sites and
1045 photocurrent responses [212]. Likely, a novel tube 0.3%-MWCNT@MIL-68(In)-
1046 derived CInS-2 achieved the highest photocatalytic activity (100%) for TC degradation
1047 driven by visible light within 120 min, much higher than that of the pure hollow In_2S_3

derived from MOF (61.7%) and conventional In_2S_3 bulk (47.1%), demonstrating the dramatic enhancement of photodegradation kinetics by introduction of MWCNT [213]. MWCNTs as electron acceptor and In_2S_3 hollow tube as active center could promote the separation of electron-hole pairs and shorten the transfer distance of charge carriers, respectively, which resulted in the boosted degradation efficiency of TC under visible light.

To sum up, research on photocatalytic degradation of organic pollutants is springing up obviously owing to the rapid development of nanomaterials. MOF-derived nanomaterials play a vital role in the fabrication of photocatalysts because of their devisable architectures and remarkable semiconductor behavior. Combination of the MOF derivatives with other materials such as metal nanoparticles, plasmonic metals, and carbons to construct heterojunction is a pivotal way to exert their synergy and further promote the photocatalytic activity. Additionally, morphology control and heteroatomic doping also provide impressive approaches to develop the highly efficient photocatalysts for environmental remediation [214, 215]. Although tremendous outstanding explorations have been devoted to achieving the high efficiency and satisfied reusability of photocatalysts from MOFs, there still have lots of room for improvement in practical application. Hence, more systematic and comprehensive researches for developing industrial-level MOF-derived photocatalysts are urgently needed.

Recent years, Fenton-like catalysis as an advance oxidation technology for degradation of recalcitrant organic contaminants in wastewater has been a topic of much interest. In Fenton-like process, the *in situ* produced hydroxyl radicals are the highly active species and main oxidation agent for the degradation of organic pollutants. Generally, metal ions at low valence states can activate H_2O_2 decomposition to produce •OH radicals for continuous decomposition of targets, and then the high valence metal ions are reduced by H_2O_2 to achieve the redox cycle, which guarantees the catalytic reactions work consecutively. Besides, the presence of secondary metals in catalysts may provoke the rapid transformation of two metallic redox pairs in conjunction with the catalytical decomposition of the H_2O_2, thereby facilitating the efficiency of the electrolytic system [216]. Upon the introduction of light radiation, the photo-excited e^- can not only react with H_2O_2 to generate •OH but also accelerate the recycling of metal species. In the electro-Fenton system, the active •OH radicals can be yielded through reaction between cathodically produced H_2O_2 and metal ions on the catalyst surface [217]. Such a reaction of *in situ* generated H_2O_2 can enhance the efficiency of the subsequent oxidation process and lower the costs of H_2O_2 consumption as well. MOF-derived nanomaterials with permanent porosity, large surface area, tailored texture and well-designed structure possess enormous potential in this research field, which open up infinite opportunities for the rapid progress of heterogeneous catalysts for Fenton-like systems.

Among the various kinds of reported derivatives from MOFs, transition metal-based catalysts (e.g. Fe, Co, and Cu) show great potential in heterogeneous Fenton-like system [218-220]. For example, Li et al. constructed porous Fe_3O_4/C octahedral with magnetism by a two-step calcination of MIL-101 (Fe) for MB removal (Fig. 16a) [221]. The MB degradation efficiency reached 100% in 60 min in the present of Fe_3O_4/C and H_2O_2, whereas, only 67% degradation efficiency was reached during 120 min by the singular Fe_3O_4 NPs prepared from precipitation, indicating a synergistic effect between Fe_3O_4 and graphitic carbon layer (Fig. 16b and c). The mesoporous structure of Fe_3O_4/C provided abundant active sites and porous channels for full contact in both catalyst and MB molecule, leading to the improved Fenton-like catalytic behavior. Firstly, the graphitic carbon layer and porous structure absorbed organic contaminants to the catalysts surface through π-π stacking interactions. Then the absorbed pollutant were diffused on the Fe_3O_4 surface by mesoporous channels and induced Fenton-like system with Fe^{3+}/Fe^{2+}. Besides, the good recyclability and stability of Fe_3O_4/C could be ascribed to the protection of the graphitic carbon layer.

Furthermore, the introduction of other metals into Fe-containing MOF-derived materials could induce the generation of more free radicals through a powerful synergistic effect, further accelerating the catalytic degradation of organic pollutants in water body [20, 222, 223]. For instance, Bao et al. prepared a novel $CuFe_2O_4$/Cu@C catalyst consisting of $CuFe_2O_4$ (64.84%), Cu (3.80%), and C (31.36%) to degrade MB [223]. The removal efficiency of MB reached 100% within 15 min when

1109 $CuFe_2O_4$/Cu@C as a catalyst, owing to the formation of more hydroxyl radicals, while
1110 only 56% was attained by Fe_3O_4@C. These phenomena suggested the effective synergy
1111 of Cu^0 in the generation of hydroxyl radicals, which resulted in excellent MB
1112 degradation. Similarly, He et al. reported hollow Fe-Pd@C nanomaterials with core-
1113 shell structure for strengthened Fenton catalysis, which achieved rapid (within 10 min)
1114 and effective degradation of phenol (95% mineralization rate) [20]. Low contents of Pd
1115 NPs in Fe-Pd@C (mass ratio of the original material: Fe/Pd = 100:1) promoted the fast
1116 redox cycle of Fe^{3+}/Fe^{2+}, hence enhancing the catalytic activity and pH endurance of
1117 the nanomaterials.

1118 The integration of external energy also can improve the catalytic activity of MOF-
1119 derived heterogeneous catalysts in Fenton-like process for wastewater treatment. Using
1120 Prussian blue (PB) nanocubes as precursors, Wang and co-workers constructed SnO_2-
1121 encapsulated α-Fe_2O_3 (Fe_2O_3@SnO_2) nanocubes as photo-Fenton catalysts for RhB
1122 removal [224]. The resulting samples displayed excellent degradation efficiency (up to
1123 99.7%) in 60 min, much better than that of commercial Fe_3O_4 and α-Fe_2O_3 (both lower
1124 than 30%). This was mainly ascribed to the indirect contribution of SnO_2 shells to the
1125 simultaneous optimization on microstructure and crystalline phase of Fe_2O_3. Nearly
1126 complete removal was attained after 30 min in the presence of catalyst, H_2O_2 and visible
1127 light simultaneously, illuminating the synergy between individual in heterogeneous
1128 catalytic photo-Fenton reaction was responsible for the effective degradation of target

pollutants. Besides, the radical-based oxidation process was inferred as the dominant route for RhB degradation where •OH worked as the main reactive species.

Liu et al. reported CMOF@PCM electro-Fenton catalysts from three pyrolyzed Fe-MOFs (MIL-88(Fe), MIL-101(Fe) and MIL-100(Fe)) for the degradation of napropamide at neutral pH in aqueous solution [225]. In this electro-Fenton reaction system, the relative removal efficiency of napropamide decreased by the order of CMIL-100@PCM (82.3%) > CMIL-88@PCM (64.1%) > CMIL-101@PCM (60.56%). The best catalytic ability with degradation efficiency of 97% within 60 min was observed when using CMIL-100@PCM25 as catalyst. Low leaching concentration of reactive Fe (approximately 6.5 ppb) from CMIL-100@PCM exhibited the excellent durability of this system. Besides, the porous with narrow distribution in CMOF@PCMs resulted in an easy accessibility to the active Fe^{2+}/Fe^{3+} catalytic centers. The optimization of the availability of Fe^{2+} sites by porous CMOFs allowed to induce the initial oxidation of Fe^{2+} to Fe^{3+} and •OH in the presence of H_2O_2.

Importantly, however, in spite of several classes of MOF-derived nanomaterials are able to degrade organic contaminants effectively in Fenton-like system, while research in this area is still at an early stage, more derivatives or their composites with great potential should be investigated. The combination of photo- or electro-energies with pyrolytic MOFs to catalyzed Fenton-like process is currently an vibrant research area for this technology [226]. Up till now, iron leaching cannot be avoided completely even though enormous attempts have been devoted. Moreover, the continuous loss

during supernatant discharge and the limited working pH range hinder their practical use. Thus, a large amount of improvements are required for their flexibility with real wastewater.

Recently, employing catalysts to activate PS/PMS have been frequently studied to treat wastewater pollution due to their strong oxidizing ability and high selectivity. MOF-derived nanocomponents with favorable structural and compositional properties as emerging catalysts are intensively used in this process. The possible mechanisms responsible for PS/PMS activation towards the removal of organic contaminants in MOF-derived nanomaterials are involved in radicals and non-radical pathway. As for metal oxides, the catalytic degradation is dominated by radicals (commonly as $SO_4^{\bullet-}$ and •OH). In this oxidation process, the breakage of the peroxide bond (–O–O–) of PS/PMS can be induced to generate $SO_4^{\bullet-}$ which can degrade and partly decompose the pollutant molecules into CO_2 and H_2O, and the residual transform into small molecule intermediates [227]. With respect to metal/carbon hybrids and carbon materials, non-radicals (mainly as $^1O_2$ and electron-transfer) catalytic process could be induced to activate PS/PMS and further degrade organic pollutants. Graphitic N atoms in carbons can trigger electron transfer from carbon atoms to neighboring graphitic nitrogen by breaking the chemical inertness of the sp^2-hybridized carbon configuration, thus producing positively charged active sites [228]. The efficiency of non-radical oxidation process is primarily dependent on the conductivity, graphitic degree and N-

doping of carbonaceous catalysts. However, non-radical pathway has not revealed completely and more deep researches are required to make it clear.

Transition metal catalysts particularly the multiple metal oxides with versatile advantages such as being highly redox active in catalytic process, ferromagnetic and multifunctional (e.g. antibacterial, etc.) are regarded as the dominant and superb catalysts for promoting PS/PMS activation [229-231]. For instance, Li and colleagues reported hollow porous $Fe_xCo_{3-x}O_4$ nanocages through pyrolyzing the pre-designed precursors of Fe_yCo_{1-y}-Co PBAs nanospheres for BPA removal with PMS activation [232]. In their work, the Fe doping amount was demonstrated significantly influence the final morphology of $Fe_xCo_{3-x}O_4$. The particle size increased to 160 nm from about 80 nm and the shape gradually became more uniform as the increase of Fe amount. $Fe_{0.8}Co_{2.2}O_4$ showed the most uniform nanocages, which achieved 95% BPA degradation efficiency during 60 min when the simultaneous presence of $Fe_{0.8}Co_{2.2}O_4$ nanocages and PMS. The B-site Co^{II} on the surface of catalyst was confirmed as the primary factor for the superior activity. Similarly, a magnetic core-shell Co_3O_4@Fe_2O_3 almost removed 100% norfloxacin (NOR) within 45 min, while Fe_2O_3/PMS system could not degrade NOR effectively and Co_3O_4/PMS system only showed a moderate performance for NOR elimination [233].

In addition, transition-metal nitrogen carbon materials are attractive alternatives because of their high efficiency and lower adsorption energy [234]. For instance, Zhang et al. constructed yolk-shell structured CoN/N-C@SiO_2 as nanoreactor with dual active

sites through nitridation of parent ZIF-67@SiO_2 for TC degradation (Fig. 17a) [235]. The *in-situ* formed N-doped carbon layer not only acted as catalytic sites but promoted electron transfer. Benefiting from the structural and composition modulation (Fig. 17b), the CoN/N-C@SiO_2 nanoreactor degraded about 95% TC in 30 min witnin a broad pH working range (Fig. 17c and d). Specifically, the microenvironment in the yolk-shell structure and the hydrophilic SiO_2 shell improved the catalytic stability and offered driving force to promote reaction rate; dual active sites referred to the CoN core and N-doped carbon layer performed the synergic action of non-radicals and radicals during PMS activation. The CoN/N-C@SiO_2-500 exhibited excellent removal performance towards various organic pollutants and a slight decrease in the presence of four anions (Fig. 17e and f), suggesting the great potential in practical use. Liu et al. synthesized nitrogen-doped porous Co@C nanoboxes (Co@NC) from ZIF-67 for p-chloroaniline (PCA) degradation with PS activation [236]. A complete removal of high concentration PCA within 2 min was achieved, which could be explained by the formation of radical species (mainly sulfate radicals and hydroxyl radicals) and non-radical species. Notably, the porous and hollow carbon nanobox architecture offered large surface areas, benefiting the target molecule adsorption and further oxidization. Unfortunately, the cobalt leaching was inevitable even though the prepared materials implemented etching treatment to remove away excess metallic cobalt.

To avoid secondary pollution for environment, metal-free catalysts are required to eliminate the organic contaminants. Nitrogen-doped graphene derived from MOF acted

as a PMS facilitator and displayed almost 100% phenol removal within 30 min [237]. The high specific surface area, pore volume, nitrogen atoms doping as well as the structure of graphene all can account for the fascinating degradation efficiency of target pollutant. During the process of PMS activation, singlet oxygen exerted a dominant impact on the removal process. In addition, the pH effect on phenol decomposition also investigated and the results indicated the degradation efficiency was better in alkaline conditions, which could promote the SO_5^{2-} generation and further produce more singlet oxygen. In Zhang's work, N-doped hierarchical carbon catalysts showed 98% of BPA removal efficiency in 5 min, which surpassed many other PMS activators [167]. In this process, a singlet oxygen-dominated non-radical mechanism was proposed.

MOF-derived carbonaceous materials are superior catalysts for wastewater treatment under PMS/PS presence in which radical and non-radical pathway both play a significant role in destructing environmental pollutants. Most of these derivatives show an incredible improvement in performances than pristine MOFs owing to their expanded surface areas, ultrahigh porosity and heteroatom introduction. Among them, metal/carbon hybrids and carbon materials seem to have better stability and more eco-friendly. Undesirably, the formed ClO_3^-/BrO_3^- and halogenated disinfection byproducts in catalytic process are potentially toxic as well as excess SO_4^{2-} and residual PMS in water have an adverse effect on environment [238-240], more simple and efficient methods should be used for overcoming these obstacles.

For wastewater treatment, just like the discussed-above, MOF-derived nanomaterials can not only serve as selective adsorbents of contaminants but also act as platforms for environmental pollutants degradation through catalytic processes. In most cases, both characters of MOFs can synergistically function in the degradation. Specifically, MOF derivatives could adsorb large amount of target molecules in solution owing to their high surface area and suitable pore sizes, enabling these adsorbed contaminants with better access to the surface sites on catalysts. The close distances between targets and catalytic sites improve the utilization efficiency of active species before them disappearance. Besides, the increased local concentration of pollutant molecules facilitates the catalytic activity as well. Characterized by the excellent degradation efficiency, favorable mineralization rate and good stability, MOF-derived nanostructured catalysts show promising potential in this area. Well-designed structure such as hierarchical porous and hollow core-shell are advantageous to the facilitated mass/electron transport and highly exposed active sites. In order to avoid secondary pollution and control cost, the selection of the compositions of MOF precursors needs to be more judicious. In general, environmentally friendly metal nodes and relatively simple organic ligands are more popular. Notably, a large number of researches at present have been concentrated on the removal of dyes, BPA and phenols, while the studies concerned with other emerging contaminants such as PPCPs, pesticides and perfluorinated compounds are rare. In spite of some favorable achievements have been realized for the elimination of organic contaminants by using

MOF-derived materials as heterogeneous catalysts, issues related to the large-scale preparation and efficient recycling impose restrictions on their industrial applications. To overcome these challenges still has a long way to go. How to successfully apply the outcomes of the laboratory to the commercial field is the key question for researchers to ponder in the future work.

4.2 MOF-derived nanomaterials for air purification

4.2.1 CO_2 capture and separation

Enormous carbon dioxide emission produced by anthropogenic activities especially fossil fuel combustion poses a severe threat to the natural environment. The resulting greenhouse effect leads to climate change and environmental deterioration, further exerting a negative influence on animal survival and human health. In order to alleviate the ever-increasingly serious damage, developing technology to adsorption CO_2 effectively is receiving growing concern around the world. MOF-derived nanoporous materials as sorbents provide an advisable choice for CO_2 capture, as already proved by many publications [241-243]. Notably, physisorption occurs mainly in the pore channels and surface of adsorbents, where ultrahigh porosity and large surface area of adsorbents are beneficial to improve the CO_2 uptake capacity [242]. Microporous structure plays an important role in CO_2 adsorption at ambient pressure, but mesopore and macropore structure have a less enhancement effect for it. Besides, heteroatoms doping into carbon framework such as O-doped and N-doped has a prominent impact on CO_2 uptake ability [244, 245]. For the pyrrole and amine group-

functionalized adsorbents, CO_2 molecules can interact with the N and H atoms on the surface through Lewis acid-base and H-bond [246]. Specifically, upon adsorption, CO_2 as acidic gas locates in close proximity to basic N active site in pyridine group owing to Lewis acid-base interaction where the lone pair electron of N atom provides the electronic change for the carbon atom in CO_2 as well as the steric hindrance effect within CO_2 and functional group [247]; the H atom in hydroxyl group react with the O atom in CO_2 cause the H-bond interaction.

Recently, nanoporous carbons (MUCT) were synthesized from MOF-5 and urea [248]. The optimal sample MUC900 indicated the best CO_2 uptake ability of 3.71 mmol g^{-1} at 273 K (1 atm). The CO_2 capture was improved thanks to the high nitrogen amounts, microporous surface area, and C–OH groups of porous carbons. The interaction of CO_2 with functional groups was facilitated by the hydroxyls through electrostatic potentials as well as hydrogen-bonding interactions, hence contributing to the increasing CO_2 capture of MUCT samples. Later on, MOF-5-derived carbon materials achieved CO_2 uptake capacity of 2.43 mmol g^{-1} at 298 K and 1 bar [249]. The calculated total pore volume, micropore volume as well as BET surface area of the prepared porous structure were equal to 1.84 cm^3 g^{-1}, 0.59 cm^3 g^{-1} and 1884 m^2 g^{-1}, respectively, higher than those of pristine MOF-5 (0.33 cm^3 g^{-1}, 0.24 cm^3 g^{-1} and 477 m^2 g^{-1}, respectively). The CO_2 uptake decreased persistently with the increasing temperature (from 298 K to 373 K). Conversely, the increasing pressure value (from 0 up to 40 bar) resulted in higher CO_2 capture. In Zou's work, the high CO_2 adsorption

capacity (4.76 mmol g^{-1} at 273 K) of the ZIF-68-derived N-doped carbons was influenced by the surface area as well as governed by the local structure and doped N-species [163].

It is worth noting that high selective CO_2 adsorption from mixed gases and high CO_2 capture ability at low pressure are of great practical significance for industrial-level application. Early on, the 24h@500°C derived from ZIF-8 displayed favorable CO_2 adsorption of 1.79 mmol g^{-1} at 1 bar and 25 °C, more than twice of initial ZIF-8 (0.7 mmol g^{-1}) [250]. Benefitting from the interaction of the lone-pair electrons on nitrogen, the basic N-containing functional groups exhibited high affinity towards acidic CO_2, which could account for the improved CO_2 capture [251, 252]. Importantly, the 24h@500°C exhibited a significantly enhanced CO_2 selectively over N_2, two-fold higher than that of the original ZIF-8. Pan et al. developed the KBM-700 with large nitrogen amount (10.16%) and pore volume with microsize (73%) by calcination of K^+@bio-MOF-1, which displayed enhanced performance in CO_2 capture (4.75 mmol g^{-1}) at 1 bar and 298 K than the BM-700 (3.52 mmol g^{-1}) without K^+ introduction, where the N functional groups and microporosity played a dominant part [169]. The BM-T presented a large number of mesopores, while the dominance of micropores indicated in the KBM-T. The CO_2 over N_2 selectivity of KBM-700 was much higher than that of BM-700, such a great improvement could contribute to the well-designed micropore structure as well as the narrow distribution of pore size owing to K^+ activation.

Wang and colleagues synthesized oxygen-doped nanoporous carbonaceous material by thermal treatment of pristine MIL-100Al, MIL-100Al/F127 composite, and MIL-100Al/KOH mixture, namely AAC-1, AAC-2 and AAC-3, respectively [253]. The obtained AAC-2W (washing with HCl) showed the highest CO_2 adsorption even at different temperatures, which was 4.8 mmol g^{-1} at 298 K and 6.5 mmol g^{-1} at 273 K. The incredible CO_2 uptake ability could be put down to the well-defined porous structure and adequate oxygen incorporation. The ultrahigh porosity offered sufficient space to take in gas molecules and the surface polarity and basicity afforded by abundant functional groups strengthened the bonding force with acidic CO_2. Importantly, the high CO_2 adsorption amounts of 1.72 and 1.74 mmol g^{-1} at 298 K and 0.2 bar was also observed when AAC-1W and AAC-2W as sorbents, suggesting a desirable performance even under low CO_2 partial pressure environment. Benefiting from the higher quadrupole moment and polarizability, the highest CO_2/N_2 selectivity was attained by AAC-1 at 298 K and 1 bar, as well as the highest CO_2/CH_4 selectivity was achieved by AAC-2 in the same circumstances. The great distinction of CO_2 capture over CH_4 and N_2 capture capacity demonstrated the good binary separation selectively of these derivatives, in favor of a real application for flue gas and natural gas separation.

MOFs with permanent porosity have been broadly employed in CO_2 uptake while the reports related to their derivatives are relatively limited. The highest CO_2 capture capacity of 4.8 mmol g^{-1} at 298 K 1 bar was achieved by Wang's group, comparable

with the 4.75 mmol g^{-1} at the same conditions in Pan's work, suggesting the good contribution of additional activating agents for enhanced performance. Owing to the predominant role of micropore in CO_2 adsorption, many attempts to construct the microporous structure and modulate micropore volume should be made. Remarkably, improving the selectivity of CO_2 capture in binary even polynary gas system as well as enhancing the adsorption ability at low pressure are important for practical applications.

4.2.2 VOCs degradation

VOCs, as a typical pollutant in atmospheric environment, are defined as organic compounds that begin to boil at below or equal to 250 ℃ [254, 255]. VOCs have a wide range of types, including acetone, acetic acid, toluene and benzene. These varieties of VOCs mainly emitted from industrial processes and human activities cause severe harm to human health and the ecological environment because of their toxicity and environmental persistence [256-258]. Moreover, VOCs are the primary precursors of secondary aerosols and photochemical smog, which have adversity effects on human survival and sustainable development [259, 260]. Inspired by rigorous regulations of air pollution control, many techniques have been applied for the abatement of VOCs, such as plasma process, adsorption, catalytic combustion and photocatalysis [261-263]. MOF-derived metal oxides or their hybrids (e.g. Mn-based, Ce-based, Cr-based, Ti-based, etc.) are deemed to be the potential catalysts for VOCs elimination due to their superiorities.

Recently, Chen et al. reported a series of three-dimensional penetrating mesoporous Pt@M-Cr_2O_3 for toluene combustion [263]. Particularly, the unique structure of three-dimensional penetrating mesoporous channels is useful for facilitating the contact possibility of toluene molecules with active sites, thereby showing higher reactivity in catalysis of toluene oxidation [264, 265]. In comparison with M-Cr_2O_3 derived from MIL-101-Cr, the catalytic activity of Pt@M-Cr_2O_3 was improved remarkably after Pt loading, indicating the promotion of Pt NPs in catalytic activity. The 0.82Pt@M-Cr_2O_3 catalyst (Pt = 0.824 wt.%) showed the best degradation performance for toluene combustion at 145 ℃. It is worth pointing out that the synergic effect among more lattice defects, smaller-size and well-dispersed Pt nanoparticles, high ratio of Pt^0/Pt^{2+}, large surface area and distinct architecture of 0.82Pt@M-Cr_2O_3 contributed to the strongest catalytic ability to toluene oxidation. The combustion of toluene by 0.82Pt@M-Cr_2O_3 was achieved through fast transformation to aldehydic and subsequently benzoate and form CO_2 and H_2O at final.

Supported noble metal catalysts display outstanding catalytic oxidation activities for VOCs at low temperatures [266, 267]. However, expensive price and low reserve impede their further development in practice. Therefore, exploiting transition metal oxides catalysts derived from MOFs with low cost and high performance are attracted more attention [268-270]. For instance, Sun and co-workers prepared MnO_x-CeO_2-MOF through heating Ce/Mn-MOF-74 and used it for toluene oxidation [271]. The obtained catalysts showed the T_{50} and T_{90} (corresponding to the toluene conversion of

50% and 90%, respectively) of 210 and 220 °C as well as the apparent activation energy of 82.9 KJ mol^{-1}. These parameters were lower than those of MnO_x-MOF, MnOx-CeO_2-CP and MnO_x-D, which were prepared by directly pyrolysis of MOF-74 without Ce, co-precipitation and thermal decomposition of MnOOH, respectively. The introduction of Ce into MnOx framework was conducive to the enhancement of catalytic performance in toluene degradation owing to the rich oxygen vacancies, large surface area, good oxygen mobility, excellent low-temperature reducibility and considerable Mn^{4+} contents in surface, which exerted an important effect on catalytic process.

Non-thermal plasma (NTP) technology has great potential to remove diluted VOCs whereas it possess some shortcomings including low CO_2 selectivity and formation of unwanted by-products. Combining the advantages of NTP and heterogeneous catalysis can overcome these limitations and efficiency enhance the VOC removal. Feng's group developed a novel method for toluene removal by MOF-derived porous tri-metallic oxide catalyst ($MnCoNiO_x$, MCNO) combined with NTP technology [272]. MCNO composite showed much higher BET surface area (59.82 m^2 g^{-1}) and total pore volume (0.350 m^3 g^{-1}) than NiO_x (11.24 m^2 g^{-1}, 0.046 m^3 g^{-1}), CoO_x (4.98 m^2 g^{-1}, 0.090 m^3 g^{-1}) and MnO_x (7.69 m^2 g^{-1}, 0.110 m^3 g^{-1}). As expected, the toluene degradation efficiency achieved 75.7% by NTP-MCNO, better than that of NTP alone (42.9%), NTP-MnO_x (59.3%), NTP-CoO_x (70.9%) and NTP-NiO_x (65.0%). The highest degradation efficiency attained by MCNO catalyst was 99.72% with the

specific input energy of 444 J L^{-1}. The as-synthesized samples and NTP performed well in synergy and thus resulted in good catalytic activity of toluene elimination. Furthermore, semiconductor photocatalytic oxidation is a promising approach to degrade VOCs into innocuous CO_2 and H_2O. In recent, TiO_2@C-N(30) photocatalysts derived from NH_2-MIL-125 showed the best mineralization efficiency of 51.9% and removal rate of 62.4% for styrene under visible light irradiation within 240 min (Fig. 18a and b) [81]. In this reaction system, TiO_2@C-N(x) formed $\bullet O^{2-}$ and •OH radicals with powerful oxidation capacity owing to the generated anatase-rutile phase junction and the effective interface interaction between the N-doped mesoporous carbon shell and TiO_2 core, which endowed it with superior photocatalytic activity and remarkable mineralization efficiency for photocatalytic degradation of styrene (Fig. 18c).

4.2.3 Radionuclide adsorption and separation

The continuous growth of human population and the rapid development of industrialization have intensified the demand for energy. For the past few years, the massive consumption of nonrenewable fossil-fuel resources such as petroleum products (4%), natural gas (22%) and coal/peat (41%) and the limited contribution from renewable energy sources (3.5%) such as wind, solar and hydro pose a pressing task for mankind about the exploitation of new primary energy sources [273, 274]. Actually, nuclear power as a cheap and feasible alternative has been utilized in electricity production [275]; however, radioactive gaseous pollutant (e.g. Kr, and Xe) are inevitable products in this process. These hazardous gases are generated from the pre-

treatment/shipping procedures of high- or low-level waste and cause damage to living things [276]. Although cryogenic distillation has been used to concentrate Xe and Kr from air, its high energy consumption and high cost are undesirable. Alternatively, MOF-derived porous nanomaterials with more economical and energy-efficient have great potential for the adsorption separation of Xe and Kr at low pressure and room temperature.

For example, Zhong et al. employed ZIF-8/xylitol as precursors to synthesize carbon-ZX and further studied Xe capture and separation [277]. Xe adsorption ability of carbon-ZX reached up to 4.42 mmol g^{-1} at 298 K and 1 bar, which was significant promotion compared to carbon-Z (directly carbonization of ZIF-8 without xylitol) of 3.17 mmol g^{-1} and parent ZIF-8 of 1.21 mmol g^{-1}. Moreover, carbon-ZX displayed the best selectivity for both Xe/N_2 and Xe/CO_2 gas mixtures in comparison of carbon-Z and original ZIF-8. The asymmetrical charge distribution on the N-doped porous carbon framework and removal of excluded effects from hydrogen atoms on aromatic rings were beneficial for the enhancement of affinity both in resultant material and Xe molecular as well as the electrostatic attraction between the surface charges and polarizable Xe molecules, which give rise to the outstanding performance of carbon-ZX.

Later on, Gong's group reported on a series of nanoporous carbons using ZIF-11 and FA as precursors for Xe/Kr separation at dilute conditions [278]. It is noting that the Xe capture capacity of these prepared materials and commercial AC are greatly

relevant to their micropore size which is less than 1 nm. The Z11CBF-1000-2 showed much higher BET surface area (1020 m^2 g^{-1}) and micropore volume (pore diameter < 1 nm, 0.316 cm^3 g^{-1}) than other resulting samples and AC. The Xe uptake of Z11CBF-1000-2 was 4.87 mmol g^{-1} at 298 K and 1 bar, which was not only better than that of parent ZIF-11 (1.22 mmol g^{-1}), but also CC3 (2.32 mmol g^{-1}) [279], Ni-MOF-74 (4.16 mmol g^{-1}) [280], carbon-ZX (4.42 mmol g^{-1}) [277] and Ag@MOF-74-Ni (4.81 mmol g^{-1}) [281] in other reported studies. The excellent performance could be attributed to their microporous structure with narrow pore-size distribution (5–8 Å) that proper for Xe capture. Such a candidate may provide an outstanding choice for adsorption and separate Xe in used nuclear-fuel reprocessing facilities and motivate further work in this area.

Currently, the research associated with this area is relatively narrow but the great potential of MOF-derived nanomaterials for radionuclide adsorption and separation can be gained from above efficient results. The surface properties like BET surface area, pore volume and porosity play an important effect on the adsorption and separation of radionuclide, which could be regulated by adding second carbon source. Moreover, tuning the pore width to adapt to the gas molecule is also important for the improvement of the capture ability and selectivity.

4.3 MOF-derived nanomaterials for target-specific sensing

4.3.1 Gaseous pollutants sensing

As is well-known that long-run exposure to gaseous pollutants, such as VOCs, H_2S, formaldehyde, NO_x, etc., can induce many diseases to humans, further causing damage to health and even death. For example, excess dispersion of *n*-butanol in air may lead to dizziness, headache, somnolence and dermatitis [282]. Acetone released into environment may cause skin and eye irritation, narcosis and nausea [283]. In addition, H_2S gas with more than 100 ppm may impact human's nervous system while above 250 ppm can directly lead to death as well as NO_2 gas in 60 min period beyond 106 ppb may result in serious health problems [284-286]. From the perspective of environmental protection and public health, it is imperative to exploit gas sensors with satisfactory capabilities for the determination of these harmful gases, especially detecting sub-ppm level from industrial emission sources and/or low concentration at workplace and residential conditions. Sensing materials are the critical portion for gas sensor, which intensively affect the sensing performance in practice. As far as we know, the gas-sensing mechanism of a metal oxides-based sensors is based on the varying resistance resulted from the reaction of target gas with sensing material surface. When sensors are exposed to air, the oxygen molecules are chemisorbed on the surface of the metal oxides. These O_2 can capture free electrons from CB of semiconductors, resulting in the generation of negatively charged oxygen species (O_2^-, O^-, and O_2^-). Consequently, an electron depletion layer with high resistance will be produced on the

surface of metal oxides. Once reductive gas molecules are introduced, the pre-adsorbed oxygen species could react with targeted gases, and then the captured electrons will be released to the metal oxide semiconductors, finally decreasing the resistance of the sensors. MOF-derived materials with porous structures offer excellent flexibility in the aspect of selectivity and sensitivity. Gas sensors based on MOF-derived metal oxide semiconductors are promising materials in gas detection in light of their diverse morphologies, high response as well as easy integration.

A mass of the gas sensors based on MOF-derived nanomaterials perform well in VOCs detection [287-289]. For instance, Li et al. constructed the hierarchical hollow ZnO nanocages by direct pyrolysis of MOF-5 (Fig. 19a-c), which showed ppb level sensitivity with 15.3 ppm^{-1} to 50 ppb acetone at 300 °C, and sub-ppm level sensitivity with 2.3 ppm^{-1} to 0.1 ppm benzene at 400 °C, better than singular ZnO nanoparticles (1.5 ppm^{-1} and 0.9 ppm^{-1}, respectively) [290]. The unique architectures with interpenetrated ZnO NPs within porous shells presented a relative lower potential barrier than agglomeration singular ZnO NPs and afforded large number of channels with mesoporous and macroporous for promoting the diffusion and surface reaction of targeted gases (Fig. 19d and e). Moreover, the distinct hierarchical structure with highly BET surface area and sufficient exposed reaction locations provided more surface oxygen vacancies, thus gaining the significantly enhanced sensing performance. Afterwards, this group reported another study, where core-shell Au@ZnO nanoparticles derived from Au@MOF-5 performed good gas-sensing response and

selectivity towards acetone with sub-ppm concentration range at 300 °C operation temperature (Fig. 19f-i) [291]. The sensitivity value of Au@ZnO (3.42 ppm^{-1}) was 11-fold higher than that of the singular ZnO nanoparticles (0.313 ppm^{-1}) towards 1 ppm acetone at 300 °C. Besides, Au@ZnO sensor exhibited better selectivity towards acetone than other interference gases at 300 ℃ . The enhanced gas-sensing properties were mainly dependent on the electronic and chemical sensitization of Au NPs because of the formation of Schottky junction within Au-ZnO core-shell architectures (Fig. 19j and k). Both of above cases illuminated the importance of architecture-property relationships in gas sensing materials.

The single-phase binary metal oxides provide more options to tune the chemical composition [292-294]. As an example, Yin et al. synthesized a series of mesoporous In/Ga oxides (IGOs) with hexagonal morphology by calcinating In/Ga-centered MIL-68 for ethanol sensing [293]. Among them, the response value of IGO(In/Ga molar ratio = 3:2) and IGO(In/Ga molar ratio = 1:1) to 300 ppm ethanol reached up to 81 and 101, respectively, which was higher than that of In_2O_3 at the value of 11. In addition, the IGO(3:2) and IGO(1:1) displayed a detection limit of 2 ppm and exhibited more than 2.6 times higher response to ethanol than other gases (CH_3COCH_3, CH_3CHO, CH_3OH, CH_4, CO, NO_2 and H_2) at 300 ppm. The excellent gas-sensing performance could be ascribed to their comparatively large specific surface area and high oxygen vacancy concentration. Similarly, porous $NiFe_2O_4$ crystalline nanocubes derived from PBA

showed a response value of 1.9 and a detection limit of 0.52 ppm to acetone gas at a low working temperature of 160 ℃ [294].

As for H_2S gas sensor, Co_3O_4-1 derived from ZIF-67 showed superior performance for H_2S sensing at operating temperature of 241 ℃ and the detection limit was measured as 1 μg L^{-1} (signal/noise (S/N) = 3)[295]. Meanwhile, seventeen interferences except carbon disulfide showed no effect on the detection of H_2S even if their concentration was almost 12 times higher than H_2S gas. It is worth mentioning that the active Co^{3+} cations and large specific surface area could account for the high catalytic performance of Co_3O_4-1. Such a remarkable sensing material may offer a promising alternative in routine analysis. In addition, PB nanocubes derived hollow Fe_2O_3 nanoboxes with hierarchically porous structure displayed a high response (resistance ratio) of 1.23 to 0.25 ppm at 200 ℃ [296]. The obataied sensing materials with fully reversible response to 5 ppm of H_2S at a low working temperature of 50 °C illustrated its potential for operating at near room temperature, which was conducive to environment monitoring indoor and outdoor.

For gaseous formaldehyde sensing, Co_3O_4-350 derived from Co_5-based MOF showed an operating temperature of 170 ℃ , a limit of detection of 10 ppm and long-run stability of one month, making it superior to most reported Co_3O_4 materials for the formaldehyde detection and even a majority of Co_3O_4-based composites [297]. The extremely effective properties could ascribed to its unique pore structure, larger surface area and hierarchical structure. With respect to NO_2 detection, MIL-68-derived

1542 In_2O_3/MoS_2 nanocomposite was successfully constructed by layer-by-layer self-
1543 assembly method [298]. As shown in Fig. 20a-d, the MoS_2 particles were loaded on the
1544 surface of In_2O_3 hollow microtubes and both of them had good contact with each other.
1545 The In_2O_3/MoS_2 composites exhibited superior response value towards 100 ppm NO_2
1546 than that of individual In_2O_3 sensor and displayed much higher selectivity to NO_2 than
1547 six other interfering gases (C_2H_6O, CH_2O, NH_3, C_3H_6O, C_6H_6 and H_2S, 10 ppm) as well
1548 as outstanding long-run stability of one month. Moreover, the sensor may need
1549 humidity compensation under the circumstance of different relative humidity because
1550 its response value dropped with the ambient humidity increasing. The significantly
1551 improved NO_2 sensing behavior were endorsed by the formation of n-n heterojunction
1552 at interface between In_2O_3 hollow microtubes and MoS_2 NPs and the distinct structure
1553 (Fig. 20e and f).

1554 At present, most studies about gaseous environmental pollutants focus on the
1555 VOCs detection, especially acetone. Other harmful gases such as H_2S, HCHO and NO_x
1556 need to be given more attention in the future. Hierarchical and hollow porous structure
1557 and formed heterojunction are beneficial to the diffusion and surface reaction of
1558 targeted gases. The highly specific surface area and sufficient active sites also can
1559 afford the enhanced sensing performance. Generally speaking, gaseous pollutants
1560 usually exist in the environment at low concentration, especially sub-ppm level in
1561 residential or working place. Therefore, it is valuable and challengeable to develop
1562 excellent sensing materials for the trace amounts of hazardous gases detection. MOF

derivatives show great potential in sensing materials because they have much advantageous in texture adjustment, morphology control, and component selection, which highly determine the detecting properties of gas sensors.

4.3.2 Organic pollutants sensing

Many harmful chemicals are released into natural waters including surface water, groundwater and seawater through industrial, agricultural, medical, domestic drainage and animal manure, which threaten the survival of marine plants and animals, and of course include human beings, thus working severe damage to the ecological environment. Some toxic pollutants, even at an extremely low concentration in ambient water, can cause irreversible harm to living things [299]. Currently, the accepted standard techniques, including capillary electrophoresis [300], chemiluminescence [301], liquid chromatography-mass spectrometry [302], and high performance liquid chromatography (HPLC) [303], commonly have the shortcomings of sophisticated instruments and cumbersome operations [304-306]. From this viewpoint, special attentions are given to the sensing platform on the basis of MOF-derived materials because of their numerous advantages.

A novel electrochemical sensing platform based on Mn-MOF-derived MnO_2/Mn_3O_4 and Ti_3C_2 MXene/Au NPs composites was reported for pesticide detection [307]. The 3D MnO_2/Mn_3O_4 hierarchical microcuboids combined with Ti_3C_2 MXene/Au NPs composite with high surface area, excellent electrochemical performance and good environmental biocompatibility yielded synergistic signal

amplification effect. The reported sensor possessed a low detection limit of 1.34×10^{-13} M under the optimum conditions, along with a fine linearity of R = 0.995. Similarly, single hierarchical CuO material derived from Cu-BTC with high photocurrent conversion efficiency was employed to detect malathion by photoelectrochemical (PEC) method [308]. The constructed sensor in this work showed a detection limit of 8.6×10^{-11} mol L^{-1} within the linear range of 1.0×10^{-10}-1.0×10^{-5} mol L^{-1}.

Aside from single metal oxides, metal oxide/porous carbon composites are used extensively owing to the combination of individual advantages. Wang et al. proposed electrochemical sensors comprising $FeO_x/TiO_2@mC_{700}$ NPs derived from bimetallic Fe/Ti-based MOFs for 4-nitrophenol (4-NP) detection [309]. Benefiting from the hierarchically micro/mesoporous structure and highly specific surface area of 158.2 m^2 g^{-1}, the synthesized materials possessed rapid mass transport and plentiful available active sites. The combination of good catalytic activity of FeO_x and TiO_2 and excellent electronic conductivity of mesoporous carbon resulted in high detection ability. $FeO_x/TiO_2@mC_{700}$/GCE sensor showed a low detection limit of 0.183 μM (S/N = 3) towards 4-NP in a wide concentration range of 5 to 310 μM, and exhibited outstanding selectivity for 100 μM 4-NP compared with other interferences. Feng et al. reported plasmon Au coupling with $In_2O_3@g\text{-}C_3N_4$ nanostructures (AuInCN) for TC detection by PEC aptasensor first time [310]. The as-prepared materials showed remarkable PEC performance due to the fast separation and transfer of electron-hole pairs by $In_2O_3@g\text{-}C_3N_4$ (InCN) heterojunction as well as the enhanced light harvest and photoelectron

transfer by Au nanoparticles. In this study, the PEC aptasensor presented long-term stability, acceptable reproducibility, good selectivity and high recovery value in actual samples for TC detection and exhibited a detection limit of 3.3 pmol L^{-1} (S/N = 3) with a broad concentration range of 0.01 nmol L^{-1}-500 nmol L^{-1}. These favorable results clarified the AuInCN composite with good visible light PEC response give a novel platform for target-specific sensing in environment.

4.3.3 Heavy metal ions sensing

The continuous decrease of freshwater resulted by serious pollution from industrial wastewater has become a high priority global concern. In particular, heavy-metal contamination in water supply systems has been receiving growing attention. Generally, heavy metal ions such as Pb^{2+}, As^{2+}, Cd^{2+} and Hg^{2+} are known as the extremely harmful contaminants in the biosphere, and pose a detrimental risk to ecosystem even trace amounts due to their considerable toxicity, high stability and easy to accumulation through food chains [311-314]. In the past few decades, great attention has been paid to the detection of heavy metal ions in a variety of matrices and consequently, tremendous outstanding explorations have been developed to converting MOFs or their composites into sensing materials for metals detection by electrochemical method.

The first example of using MOF-derived sensing platform to determine heavy metal ions was reported by Xiao's group in 2014 [315]. Nafion-bismuth/nitrogen doped microporous carbon (NMC) composite with good reproducibility and stability was

employed as electrode modifying material for simultaneous detection of trace Cd^{2+} and Pb^{2+} in aqueous solution. The highly specific surface area of 941 m^2 g^{-1}, large nitrogen amounts of 25.0 at.%, satisfied dispersibility and good electrical conductivity of NMC composite, as well as the synergy between Nafion and bismuth film were responsible for the enhanced signals in the simultaneous sensing of Cd(II) and Pb(II). The detection limits of Cd(II) (1.5 μg L^{-1}, S/N = 3) and Pb(II) (0.05 μg L^{-1}, S/N = 3) were 2-fold and 200-fold lower than the allowed concentration in drinking water by the World Health Organization (WHO) [316], which afforded a promising prospective for the metals sensing platform in practice. Such a remarkable sensing material possibly paves an innovative pathway for the construction of the sensitive platform based on heteroatom-doped modified electrode for the trace detection of heavy metal ions.

Zhao et al. reported a well-design Ag/Au HPNSs@FO as electrochemical sensing system for As(III) detection, which showed excellent performance due to the combination of advantages of the plasmonic and ultramicroelectrode property [317]. The as-obtained Ag/Au HPNSs@FO presented uniformity and porous structure and the thin layers of Fe oxide (FO) showed crystallinity and nanoporosity (Fig. 21a-g). The porous FO was introduced by pyrolyzing MIL-100 grown on the Ag/Au porous nanoshells (Ag/Au HPNSs) and as assisted adsorbent contributed to the improvement of As(III) sensing. The detection limit was calculated to be 0.01 ppb, much lower than the guideline values of drinking water proposed by the WHO [316]. Besides, the Ag/Au HPNSs@FO displayed good long-term stability after 1000 cycles and high detection

selectivity in the existence of various co-existing metal ions (Fig. 21h and i), demonstrating the potential application in practical water system. Benefitting from the highly micro-reactive sites of the plasmonic Ag/Au HPNSs and good adsorption ability towards As(III) of Fe oxide, the ultra-sensitive detection of As(III) with extremely low concentrations (about 1 ppt and even lower concentrations) was achieved by Ag/Au HPNSs@FO system, which raised an effective approach to boost the commercialization for ultra-trace As(III) detection and the construction of As(III) sensing platform.

Of note, heavy metals could affect the catalytic activity of MOF-derived nanomaterials. Based on this unique property, many sensing platforms with high sensitivity and selectivity for the colorimetric detection of heavy metal ions are established. Taking HKUST-1-derived CuS particles (PCuS) as example, Xiong et al. reported a novel peroxidase-mimicking system for Hg^{2+} determination using a colorimetric method [318]. The as-synthesized PCuS had intrinsic peroxidase-like activity and can oxidize 3,3′,5,5′-tetramethylbenzidine (TMB, a kind of chromogenic agent) in the presence of H_2O_2. Upon the addition of Hg^{2+}, the catalytic activity of PCuS was greatly inhibited, which could ascribed to the formation of HgS in conjunction with the highly specific binding sites on the PCuS surface, causing the blocked active sites. This study could enlighten new thoughts and provide deeper understanding for heavy metal ions monitoring by using MOF-derived materials as peroxidase-mimicking detector. In the research of Wang's group, conversely, a trace amount of Cr(VI)

dramatically accelerated the TMB oxidation without H_2O_2 because of Cr(VI)-boosted oxidation, leading to a color change of TMB in a very short time [319].

Emphasis in section 4 has been made on the environmental applications of MOF-derived nanomaterials. Among various reported technologies, adsorption and catalysis have been extensively studied and utilized for the removal of pollutants in aquatic solution. In the air purification, MOF-derived nanomaterials with the ultrahigh porosity and adjustable pore sizes show remarkable capture ability and high selectivity for CO_2 from flue gas and natural gas. Radionuclide (mainly Xe and Kr) adsorption and separation from gas mixtures are also covered in this section. Though rare articles have been issued to illustrate Xe/Kr separation using MOF-derived materials, the potential of these derivatives as adsorbents to separate noble gases (Xe and Kr) has been presented in the limited studies. As for targeted pollutants detection, MOF-derived hybrids can serve as sensing materials to construct sensing platform for the determination of gaseous pollutants, organic pollutants and heavy metal ions. The sensitivity, stability, reproducibility and selectivity of the prepared sensing materials have been discussed in detail. Moreover, the control of selectivity, which more relies on the properties of sensing materials, is still a main challenge in sensors. Therefore, more in-depth investigations are required to further optimize the sensing performance.

5. Summary and perspectives

Over the last few decades, the extremely rapid development of global economy is accompanied by unprecedented destruction of the environment. The search of advance

materials with suitable properties has become a impressing method to mitigate the ever-increasing concerns related to the environment pollution. Recent research progress in MOFs has demonstrated they can function as ideal precursors or sacrificial templates for the preparation of various nanomaterials, including metal compounds (e.g. metal oxides/chalcogenides/phosphides/carbides and their composites), carbons with or without heteroatom doping (e.g. S, B, P, O and N), as well as metal/carbon composites. To date, MOF-derived hybrids with versatile compositions, morphologies and properties have been acquired successfully and subsequently utilized in wide fields. Particularly, nanostructured materials derived from MOFs are impressing candidates for environmental cleaning and monitoring owing to their superiorities in synthesis and performance.

In the future, many issues still need to be investigated at the lab-scale, especially on the basis of obtaining a fundamental understanding of adsorption/catalytic/sensing mechanism and the relationship between structure of MOF derivatives and their performance, which could provide a guidance for the predesign and development of MOF-derived nanomaterials. Of course, to realizing environmental protection in real, further development should be made on MOF derivatives to meet their commercial demonstrations. Researchers must focus on the simplification of synthesis procedures and cost optimization while seeking routes to improving their stability, selectivity and reusability. Therefore, attention must be paid to the fabrication of MOF derivatives with

unique properties to maximize their efficiencies and ensure their industrial applications under various harsh conditions.

Though amazing progress have been developed, advanced materials derived from MOFs are still in infancy and some challenges remain to be solved. Numerous efforts are needed to realize the practical usage of MOF-derived nanostructures. Here, we present several bottlenecks and perspectives for future work in this field.

(1) In view of environmental protection, MOF precursors with eco-friendly metal nodes are more worthy of consideration in future work. The pH endurance, recyclability and resistance to the concentrations of chemicals present in the contaminated environment of adsorbents/catalysts are required to further improvement by wide investigations. Additionally, the good separability of these materials are important, which can be achieved by applying affordable gravitational (centrifugal) or endowing them with magnetism. Adsorption ability is greatly related to the heteroatom doping (e.g. N and/or O species) and the surface properties (e.g. BET area, pore volume and porosity), while the contribution of heteroatoms was not distinctly demonstrated. Besides, N-doped carbons derived from MOFs have abundant adsorption sites whereas they are usually hydrophobic. Thus, such studies are impressive and important for enhancement of adsorption capacity. For catalysis, many researches currently have been concentrated on the removal of dyes, BPA and phenols. The studies concerned with other emerging contaminants such as PPCPs, pesticides and perfluorinated compounds are in urgent need. Moreover, researchers are supposed to identify precisely

the specific active sites in catalytic process especially those with well-dispersed active species, which can be achieved by some advance technologies such as density functional theory (DFT). As for air purification, the selective capture of target gas from mixed gas system are of great important, many attempts to prepare the MOF derivatives with well-designed structure and favorable surface properties should be made. In regard to sensing, most studies about gaseous environmental pollutants focus on the VOCs detection, especially acetone. Other harmful gases such as H_2S, HCHO and NO_x need to be given more attention in the future. Moreover, further development is necessary in the functional properties of MOF-derived nanomaterials to achieve the trace detection in water and air and important fundamental and mechanistic researches are imperative to fully explore their real potentials.

(2) Most studies have the tendency to choose the widely used and common type of MOFs as precursors/sacrificial templates, such as ZIFs, MILs and PBAs. More alternative MOFs should be explored especially those with exclusively designed characteristics to gain the optimization in performance. Moreover, most of the reported investigations have focused on converting MOFs into carbonaceous materials, metal oxides and their composites, while reports on metal chalcogenides, metal phosphides and metal carbides are relatively rare due to the narrow understanding of their reaction mechanism.

(3) Pyrolytic treatment is the most widely used method for the preparation of MOF derivatives, while the harsh synthesis conditions such as long reaction time and high

temperature lead to the increased operational cost. In addition, high-temperature calcination in the synthesis may cause the destruction of inherited ordered structure and porous morphology, further weaken their reaction activity. Ligand extraction method and mechanochemical synthesis (solvent-free) seen to be better choices owing to the mild reaction conditions. However, only a few examples were reported, thus further investigation is needed. Taking production cost and benefit into consideration, operative, low cost but effective synthetic methods are eager to be introduced for the development of MOF-derived nanomaterials with enhanced performance.

(4) The morphology and structure of MOF derivatives determine their performance in a specific domain to some extent, which are greatly related to the reaction conditions such as heating rate/time, pyrolysis temperature and gas atmosphere. However, the transformation process from MOFs to their derivatives is unclear owing to the limited knowledge of the evolution mechanism. More systematic researches are highly needed to realize the precise control of synthetic routes for the preparation of fine nanostructures. Emerging technologies such as X-ray absorption fine structure, X-ray absorption near edge structure and aberration-corrected high-angle annular dark-field imaging scanning transmission electron microscopy are helpful to understand these mechanisms.

(5) To date, the long-term efficiencies of MOF derivatives in practice still leaves much to be desired, hampering their possible commercial applications. Hence, significant efforts are required to improve these functional materials for real

environmental cleanup. Besides, the high price and low productivity of MOF precursors also hinder their large-scale preparation in industry. To bridge the gap between lab-scale and industrial production, the closer cooperation between scientists and factory's workers should be promoted.

In conclusion, MOF derivatives, without any doubt, have emerged as the exciting advance materials in environment-related fields, where opportunities and challenges coexist. With sustained efforts devoted to this topic, there is plenty of space to achieve the real industrial application of MOF-derived nanomaterials in the field of environmental remediation and monitoring.

Acknowledgments

This work was supported by the National Natural Science Foundation of China (No. 51521006, 51709101, 51879101, 51508177, 51579098, 51779090), the National Program for Support of Top–Notch Young Professionals of China (2014), the Program for Changjiang Scholars and Innovative Research Team in University (IRT-13R17), and Hunan Provincial Science and Technology Plan Project (2018SK20410, 2017SK2243, 2016RS3026), and the Fundamental Research Funds for the Central Universities (531119200086, 531118010114, 531107050978, 541109060031).

References

[1] L. Jing, S.V. Kershaw, Y. Li, X. Huang, Y. Li, A.L. Rogach, M. Gao, Chemical reviews, 116 (2016) 10623-10730.
[2] F. Lu, D. Astruc, Coordination Chemistry Reviews, 356 (2018) 147-164.
[3] H. Wang, Z. Zeng, P. Xu, L. Li, G. Zeng, R. Xiao, Z. Tang, D. Huang, L. Tang, C. Lai, Chemical Society Reviews, 48 (2019) 488-516.

[4] J. Yu, H. Feng, L. Tang, Y. Pang, G. Zeng, Y. Lu, H. Dong, J. Wang, Y. Liu, C. Feng, Progress in Materials Science, (2020) 100654.
[5] J. Xie, L. Gong, S. Zhu, Y. Yong, Z. Gu, Y. Zhao, Advanced Materials, 31 (2019) 1802244.
[6] S. Yao, P. Ren, R. Song, Y. Liu, Q. Huang, J. Dong, B.T. O'Connor, Y. Zhu, Advanced Materials, (2019) 1902343.
[7] Z. Wu, Y. Wang, X. Liu, C. Lv, Y. Li, D. Wei, Z. Liu, Advanced Materials, 31 (2019) 1800716.
[8] Y. Yang, Z. Zeng, G. Zeng, D. Huang, R. Xiao, C. Zhang, C. Zhou, W. Xiong, W. Wang, M. Cheng, Applied Catalysis B: Environmental, 258 (2019) 117956.
[9] Y. Wu, H. Pang, Y. Liu, X. Wang, S. Yu, D. Fu, J. Chen, X. Wang, Environmental pollution, 246 (2019) 608-620.
[10] H. Yi, M. Li, X. Huo, G. Zeng, C. Lai, D. Huang, Z. An, L. Qin, X. Liu, B. Li, Critical reviews in biotechnology, 40 (2020) 99-118.
[11] L. Qin, H. Yi, G. Zeng, C. Lai, D. Huang, P. Xu, Y. Fu, J. He, B. Li, C. Zhang, Journal of hazardous materials, 380 (2019) 120864.
[12] M. Shen, Y. Zhang, Y. Zhu, B. Song, G. Zeng, D. Hu, X. Wen, X. Ren, Environmental Pollution, 252 (2019) 511-521.
[13] Y. Wang, Y. Zhu, Y. Hu, G. Zeng, Y. Zhang, C. Zhang, C. Feng, Small, 14 (2018) 1703305.
[14] L. Yu, S. Ruan, X. Xu, R. Zou, J. Hu, Nano Today, 17 (2017) 79-95.
[15] K. He, Z. Zeng, A. Chen, G. Zeng, R. Xiao, P. Xu, Z. Huang, J. Shi, L. Hu, G. Chen, Small, 14 (2018) 1800871.
[16] Z. Huang, K. He, Z. Song, G. Zeng, A. Chen, L. Yuan, H. Li, L. Hu, Z. Guo, G. Chen, Chemosphere, 211 (2018) 573-583.
[17] B. Song, M. Chen, S. Ye, P. Xu, G. Zeng, J. Gong, J. Li, P. Zhang, W. Cao, Carbon, 144 (2019) 1-7.
[18] Y. Fu, L. Qin, D. Huang, G. Zeng, C. Lai, B. Li, J. He, H. Yi, M. Zhang, M. Cheng, Applied Catalysis B: Environmental, 259 (2019) 117740.
[19] L. Qin, Z. Zeng, G. Zeng, C. Lai, A. Duan, R. Xiao, D. Huang, Y. Fu, H. Yi, B. Li, Applied Catalysis B: Environmental, 259 (2019) 118035.
[20] D. He, H. Niu, S. He, L. Mao, Y. Cai, Y. Liang, Water research, 162 (2019) 151-160.
[21] Q. Wang, D. Astruc, Chemical reviews, 120 (2019) 1438-1511.
[22] J. Cui, Y. Li, Z. Guo, H. Zheng, Chemical Communications, 49 (2013) 555-557.
[23] S. Kitagawa, R. Kitaura, S.i. Noro, Angewandte Chemie International Edition, 43 (2004) 2334-2375.
[24] Z. Wang, H. Wang, Z. Zeng, G. Zeng, P. Xu, R. Xiao, D. Huang, X. Chen, L. He, C. Zhou, Applied Catalysis B: Environmental, 267 (2020) 118700.
[25] D. Li, H.-Q. Xu, L. Jiao, H.-L. Jiang, EnergyChem, 1 (2019) 100005.
[26] W. Zhang, Y. Hu, J. Ge, H.-L. Jiang, S.-H. Yu, Journal of the American Chemical Society, 136 (2014) 16978-16981.
[27] W. Raza, D. Kukkar, H. Saulat, N. Raza, M. Azam, A. Mehmood, K.-H. Kim, TrAC Trends in Analytical Chemistry, 120 (2019) 115654.
[28] S.S. Kaye, A. Dailly, O.M. Yaghi, J.R. Long, Journal of the American Chemical Society, 129 (2007) 14176-14177.
[29] Y.V. Kaneti, J. Tang, R.R. Salunkhe, X. Jiang, A. Yu, K.C.W. Wu, Y. Yamauchi, Advanced materials, 29 (2017) 1604898.
[30] L. Shi, D. Benetti, F. Li, Q. Wei, F. Rosei, Applied Catalysis B: Environmental, 263 (2020) 118317.
[31] B.N. Bhadra, A. Vinu, C. Serre, S.H. Jhung, Materials Today, 25 (2019) 88-111.
[32] X. Cao, C. Tan, M. Sindoro, H. Zhang, Chemical Society Reviews, 46 (2017) 2660-2677.
[33] L. Oar-Arteta, T. Wezendonk, X. Sun, F. Kapteijn, J. Gascon, Materials Chemistry Frontiers, 1 (2017) 1709-1745.
[34] G. Zou, H. Hou, P. Ge, Z. Huang, G. Zhao, D. Yin, X. Ji, Small, 14 (2018) 1702648.
[35] S. Kitagawa, Chemical Society Reviews, 43 (2014) 5415-5418.

[36] B. Li, H.M. Wen, Y. Cui, W. Zhou, G. Qian, B. Chen, Advanced Materials, 28 (2016) 8819-8860.
[37] K. Shen, X. Chen, J. Chen, Y. Li, ACS Catalysis, 6 (2016) 5887-5903.
[38] A. Mahmood, W. Guo, H. Tabassum, R. Zou, Advanced Energy Materials, 6 (2016) 1600423.
[39] Q. Gao, J. Xu, X.-H. Bu, Coordination Chemistry Reviews, 378 (2019) 17-31.
[40] S. Dhaka, R. Kumar, A. Deep, M.B. Kurade, S.-W. Ji, B.-H. Jeon, Coordination Chemistry Reviews, 380 (2019) 330-352.
[41] R.R. Salunkhe, Y.V. Kaneti, Y. Yamauchi, ACS nano, 11 (2017) 5293-5308.
[42] W. Zhao, G. Wan, C. Peng, H. Sheng, J. Wen, H. Chen, ChemSusChem, 11 (2018) 3473-3479.
[43] Z. Xie, H. Tang, Y. Wang, ChemElectroChem, 6 (2019) 1206-1212.
[44] Z. Chen, H. Qing, K. Zhou, D. Sun, R. Wu, Progress in Materials Science, 108 (2019) 100618.
[45] X. Li, X. Yang, H. Xue, H. Pang, Q. Xu, EnergyChem, 2 (2020) 100027.
[46] Z. Liang, R. Zhao, T. Qiu, R. Zou, Q. Xu, EnergyChem, 1 (2019) 100001.
[47] W. Chaikittisilp, K. Ariga, Y. Yamauchi, Journal of Materials Chemistry A, 1 (2013) 14-19.
[48] W. Yang, X. Li, Y. Li, R. Zhu, H. Pang, Advanced Materials, 31 (2019) 1804740.
[49] C. Wang, J. Kim, V. Malgras, J. Na, J. Lin, J. You, M. Zhang, J. Li, Y. Yamauchi, Small, 15 (2019) 1900744.
[50] Y. Kinoshita, I. Matsubara, T. Higuchi, Y. Saito, Bulletin of the Chemical Society of Japan, 32 (1959) 1221-1226.
[51] B.F. Hoskins, R. Robson, Journal of the American Chemical Society, 111 (1989) 5962-5964.
[52] O.M. Yaghi, G. Li, H. Li, Nature, 378 (1995) 703-706.
[53] B. Rungtaweevoranit, C.S. Diercks, M.J. Kalmutzki, O.M. Yaghi, Faraday Discussions, 201 (2017) 9-45.
[54] Y. Luo, M. Ahmad, A. Schug, M. Tsotsalas, Advanced Materials, 31 (2019) 1901744.
[55] B. Liu, H. Shioyama, T. Akita, Q. Xu, Journal of the American Chemical Society, 130 (2008) 5390-5391.
[56] H.-L. Jiang, B. Liu, Y.-Q. Lan, K. Kuratani, T. Akita, H. Shioyama, F. Zong, Q. Xu, Journal of the American Chemical Society, 133 (2011) 11854-11857.
[57] Y. Yang, Z. Lun, G. Xia, F. Zheng, M. He, Q. Chen, Energy & Environmental Science, 8 (2015) 3563-3571.
[58] B. Liu, X. Zhang, H. Shioyama, T. Mukai, T. Sakai, Q. Xu, Journal of Power Sources, 195 (2010) 857-861.
[59] M. Hu, J. Reboul, S. Furukawa, N.L. Torad, Q. Ji, P. Srinivasu, K. Ariga, S. Kitagawa, Y. Yamauchi, Journal of the American Chemical Society, 134 (2012) 2864-2867.
[60] M.J. Katz, Z.J. Brown, Y.J. Colón, P.W. Siu, K.A. Scheidt, R.Q. Snurr, J.T. Hupp, O.K. Farha, Chemical Communications, 49 (2013) 9449-9451.
[61] G.-C. Li, P.-F. Liu, R. Liu, M. Liu, K. Tao, S.-R. Zhu, M.-K. Wu, F.-Y. Yi, L. Han, Dalton Transactions, 45 (2016) 13311-13316.
[62] K.J. Lee, J.H. Lee, S. Jeoung, H.R. Moon, Accounts of chemical research, 50 (2017) 2684-2692.
[63] C. Sun, Q. Dong, J. Yang, Z. Dai, J. Lin, P. Chen, W. Huang, X. Dong, Nano Research, 9 (2016) 2234-2243.
[64] H. Zhang, T. Wang, J. Wang, H. Liu, T.D. Dao, M. Li, G. Liu, X. Meng, K. Chang, L. Shi, Advanced Materials, 28 (2016) 3703-3710.
[65] X. Zhao, H. Yang, P. Jing, W. Shi, G. Yang, P. Cheng, Small, 13 (2017) 1603279.
[66] W. Xia, A. Mahmood, R. Zou, Q. Xu, Energy & Environmental Science, 8 (2015) 1837-1866.
[67] X. Han, W.-M. Chen, X. Han, Y.-Z. Tan, D. Sun, Journal of Materials Chemistry A, 4 (2016) 13040-13045.

[68] S.J. Yang, S. Nam, T. Kim, J.H. Im, H. Jung, J.H. Kang, S. Wi, B. Park, C.R. Park, Journal of the American Chemical Society, 135 (2013) 7394-7397.
[69] F. Bai, Y. Xia, B. Chen, H. Su, Y. Zhu, Carbon, 79 (2014) 213-226.
[70] T.Y. Ma, S. Dai, M. Jaroniec, S.Z. Qiao, Journal of the American Chemical Society, 136 (2014) 13925-13931.
[71] L. Zhang, C. Feng, S. Gao, Z. Wang, C. Wang, Catalysis Communications, 61 (2015) 21-25.
[72] X. Li, W. Zhang, Y. Liu, R. Li, ChemCatChem, 8 (2016) 1111-1118.
[73] A.J. Amali, J.-K. Sun, Q. Xu, Chemical communications, 50 (2014) 1519-1522.
[74] D.K. Yadav, V. Ganesan, F. Marken, R. Gupta, P.K. Sonkar, Electrochimica Acta, 219 (2016) 482-491.
[75] Y. Shu, Y. Yan, J. Chen, Q. Xu, H. Pang, X. Hu, ACS applied materials & interfaces, 9 (2017) 22342-22349.
[76] T. Zeng, M. Yu, H. Zhang, Z. He, J. Chen, S. Song, Catalysis Science & Technology, 7 (2017) 396-404.
[77] X. Li, A.I. Rykov, B. Zhang, Y. Zhang, J. Wang, Catalysis science & technology, 6 (2016) 7486-7494.
[78] X. Li, X. Huang, S. Xi, S. Miao, J. Ding, W. Cai, S. Liu, X. Yang, H. Yang, J. Gao, Journal of the American Chemical Society, 140 (2018) 12469-12475.
[79] H. Li, J. Tian, Z. Zhu, F. Cui, Y.-A. Zhu, X. Duan, S. Wang, Chemical Engineering Journal, 354 (2018) 507-516.
[80] C.W. Abney, K.M. Taylor-Pashow, S.R. Russell, Y. Chen, R. Samantaray, J.V. Lockard, W. Lin, Chemistry of Materials, 26 (2014) 5231-5243.
[81] H. Liu, Y. Ma, J. Chen, M. Wen, G. Li, T. An, Applied Catalysis B: Environmental, 250 (2019) 337-346.
[82] T. Devic, C. Serre, Chemical Society Reviews, 43 (2014) 6097-6115.
[83] J.H. Cavka, S. Jakobsen, U. Olsbye, N. Guillou, C. Lamberti, S. Bordiga, K.P. Lillerud, Journal of the American Chemical Society, 130 (2008) 13850-13851.
[84] C. Serre, F. Millange, C. Thouvenot, M. Noguès, G. Marsolier, D. Louër, G. Férey, Journal of the American chemical society, 124 (2002) 13519-13526.
[85] K.S. Park, Z. Ni, A.P. Côté, J.Y. Choi, R. Huang, F.J. Uribe-Romo, H.K. Chae, M. O'Keeffe, O.M. Yaghi, Proceedings of the National Academy of Sciences, 103 (2006) 10186-10191.
[86] X. Yang, J. Cai, X. Wang, Y. Li, Z. Wu, W.D. Wu, X.D. Chen, J. Sun, S.-P. Sun, Z. Wang, Environmental Science & Technology, 54 (2020) 3714-3724.
[87] S. Li, L. Xie, M. He, X. Hu, G. Luo, C. Chen, Z. Zhu, Sensors and Actuators B: Chemical, 310 (2020) 127828.
[88] W. Zhang, X. Jiang, Y. Zhao, A. Carné-Sánchez, V. Malgras, J. Kim, J.H. Kim, S. Wang, J. Liu, J.-S. Jiang, Chemical science, 8 (2017) 3538-3546.
[89] G. Huang, F. Zhang, X. Du, J. Wang, D. Yin, L. Wang, Chemistry–A European Journal, 20 (2014) 11214-11219.
[90] X. Tao, W. Cong, L. Huang, D. Xu, Journal of Alloys and Compounds, 805 (2019) 1060-1070.
[91] M. Cheng, Y. Liu, D. Huang, C. Lai, G. Zeng, J. Huang, Z. Liu, C. Zhang, C. Zhou, L. Qin, Chemical Engineering Journal, 362 (2019) 865-876.
[92] Y. Jiang, J. Gao, Q. Zhang, Z. Liu, M. Fu, J. Wu, Y. Hu, D. Ye, Chemical Engineering Journal, 371 (2019) 78-87.
[93] R. Das, P. Pachfule, R. Banerjee, P. Poddar, Nanoscale, 4 (2012) 591-599.
[94] X.Y. Yu, L. Yu, H.B. Wu, X.W. Lou, Angewandte Chemie International Edition, 54 (2015) 5331-5335.
[95] K. Cho, S.H. Han, M.P. Suh, Angewandte Chemie International Edition, 55 (2016) 15301-15305.
[96] W. Zhao, Y. Zheng, L. Cui, D. Jia, D. Wei, R. Zheng, C. Barrow, W. Yang, J. Liu, Chemical Engineering Journal, 371 (2019) 461-469.
[97] W. Sun, C. Cai, X. Tang, L.-P. Lv, Y. Wang, Chemical Engineering Journal, 351 (2018) 169-176.
[98] J. Wang, B. Wang, X. Liu, J. Bai, H. Wang, G. Wang, Chemical Engineering Journal, 382 (2019) 123050.

[99] Y.-J. Tang, H.-J. Zhu, L.-Z. Dong, A.-M. Zhang, S.-L. Li, J. Liu, Y.-Q. Lan, Applied Catalysis B: Environmental, 245 (2019) 528-535.
[100] Q. Wang, Z. Liu, H. Zhao, H. Huang, H. Jiao, Y. Du, Journal of Materials Chemistry A, 6 (2018) 18720-18727.
[101] Z. Shi, Y. Wang, H. Lin, H. Zhang, M. Shen, S. Xie, Y. Zhang, Q. Gao, Y. Tang, Journal of Materials Chemistry A, 4 (2016) 6006-6013.
[102] L. Song, T. Wang, L. Li, C. Wu, J. He, Applied Catalysis B: Environmental, 244 (2019) 197-205.
[103] H.B. Wu, B.Y. Xia, L. Yu, X.-Y. Yu, X.W.D. Lou, Nature communications, 6 (2015) 1-8.
[104] C. Abney, J. Gilhula, K. Lu, W. Lin, Advanced Materials, 26 (2014) 7993-7997.
[105] J. Li, X. Li, A. Alsaedi, T. Hayat, C. Chen, Journal of colloid and interface science, 517 (2018) 61-71.
[106] S.G. Peera, J. Balamurugan, N.H. Kim, J.H. Lee, Small, 14 (2018) 1800441.
[107] Y. Song, T. Qiang, M. Ye, Q. Ma, Z. Fang, Applied Surface Science, 359 (2015) 834-840.
[108] W. Teng, N. Bai, Z. Chen, J. Shi, J. Fan, W.-x. Zhang, Chemical Engineering Journal, 346 (2018) 388-396.
[109] P. Zhang, F. Sun, Z. Xiang, Z. Shen, J. Yun, D. Cao, Energy & Environmental Science, 7 (2014) 442-450.
[110] D. Yuan, J. Chen, S. Tan, N. Xia, Y. Liu, Electrochemistry Communications, 11 (2009) 1191-1194.
[111] J. Hu, H. Wang, Q. Gao, H. Guo, Carbon, 48 (2010) 3599-3606.
[112] J. Carrasco, J. Romero, G. Abellán, J. Hernandez-Saz, S. Molina, C. Marti-Gastaldo, E. Coronado, Chemical Communications, 52 (2016) 9141-9144.
[113] K. Jayaramulu, K.K.R. Datta, K. Shiva, A.J. Bhattacharyya, M. Eswaramoorthy, T.K. Maji, Microporous and Mesoporous Materials, 206 (2015) 127-135.
[114] H. Sun, C. Kwan, A. Suvorova, H.M. Ang, M.O. Tadé, S. Wang, Applied Catalysis B: Environmental, 154 (2014) 134-141.
[115] Z. Liu, G. Zhang, Z. Lu, X. Jin, Z. Chang, X. Sun, Nano Research, 6 (2013) 293-301.
[116] S. Li, X. Zhang, Y. Huang, Journal of hazardous materials, 321 (2017) 711-719.
[117] Z.-F. Huang, J. Song, K. Li, M. Tahir, Y.-T. Wang, L. Pan, L. Wang, X. Zhang, J.-J. Zou, Journal of the American Chemical Society, 138 (2016) 1359-1365.
[118] Y.Z. Chen, C. Wang, Z.Y. Wu, Y. Xiong, Q. Xu, S.H. Yu, H.L. Jiang, Advanced Materials, 27 (2015) 5010-5016.
[119] Y. Chen, S. Ji, Y. Wang, J. Dong, W. Chen, Z. Li, R. Shen, L. Zheng, Z. Zhuang, D. Wang, Angewandte Chemie International Edition, 56 (2017) 6937-6941.
[120] S.J. Yang, J.H. Im, T. Kim, K. Lee, C.R. Park, Journal of hazardous materials, 186 (2011) 376-382.
[121] N.L. Torad, M. Hu, S. Ishihara, H. Sukegawa, A.A. Belik, M. Imura, K. Ariga, Y. Sakka, Y. Yamauchi, Small, 10 (2014) 2096-2107.
[122] R.V. Jagadeesh, K. Murugesan, A.S. Alshammari, H. Neumann, M.-M. Pohl, J. Radnik, M. Beller, Science, 358 (2017) 326-332.
[123] L. Zou, M. Kitta, J. Hong, K. Suenaga, N. Tsumori, Z. Liu, Q. Xu, Advanced Materials, 31 (2019) 1900440.
[124] Q. Duan, X. Li, Z. Wu, A. Alsaedi, T. Hayat, C. Chen, J. Li, Journal of colloid and interface science, 533 (2019) 700-708.
[125] Z. Zhang, N. Sun, W. Wei, Y. Sun, RSC advances, 8 (2018) 21460-21471.
[126] M.H. Yap, K.L. Fow, G.Z. Chen, Green Energy & Environment, 2 (2017) 218-245.
[127] M.Z. Hussain, G.S. Pawar, Z. Huang, A.A. Tahir, R.A. Fischer, Y. Zhu, Y. Xia, Carbon, 146 (2019) 348-363.
[128] L. Zou, C.-C. Hou, Z. Liu, H. Pang, Q. Xu, Journal of the American Chemical Society, 140 (2018) 15393-15401.
[129] C.C. Hou, L. Zou, Q. Xu, Advanced Materials, 31 (2019) 1904689.
[130] L. Shang, H. Yu, X. Huang, T. Bian, R. Shi, Y. Zhao, G.I. Waterhouse, L.Z. Wu, C.H. Tung, T. Zhang, Advanced Materials, 28 (2016) 1668-1674.

[131] F.-X. Bu, M. Hu, L. Xu, Q. Meng, G.-Y. Mao, D.-M. Jiang, J.-S. Jiang, Chemical Communications, 50 (2014) 8543-8546.
[132] D. Cai, B. Liu, D. Wang, L. Wang, Y. Liu, B. Qu, X. Duan, Q. Li, T. Wang, Journal of Materials Chemistry A, 4 (2016) 183-192.
[133] L. Yu, H.B. Wu, X.W.D. Lou, Accounts of chemical research, 50 (2017) 293-301.
[134] M.J. Wang, Z.X. Mao, L. Liu, L. Peng, N. Yang, J. Deng, W. Ding, J. Li, Z. Wei, Small, 14 (2018) 1804183.
[135] Y.-F. Huang, X.-Y. Sun, S.-H. Huo, Y. Li, C. Zhong, Applied Surface Science, 466 (2019) 637-646.
[136] X.-Z. Song, F.-F. Sun, S.-T. Dai, X. Lin, K.-M. Sun, X.-F. Wang, Inorganic Chemistry Frontiers, 5 (2018) 1107-1114.
[137] C. Wang, Y.V. Kaneti, Y. Bando, J. Lin, C. Liu, J. Li, Y. Yamauchi, Materials Horizons, 5 (2018) 394-407.
[138] T. Zeng, X. Zhang, S. Wang, H. Niu, Y. Cai, Environmental science & technology, 49 (2015) 2350-2357.
[139] H. Chen, K. Shen, J. Chen, X. Chen, Y. Li, Journal of Materials Chemistry A, 5 (2017) 9937-9945.
[140] M. Zhang, C. Wang, C. Liu, R. Luo, J. Li, X. Sun, J. Shen, W. Han, L. Wang, Journal of Materials Chemistry A, 6 (2018) 11226-11235.
[141] R. Zhang, T. Zhou, L. Wang, T. Zhang, ACS applied materials & interfaces, 10 (2018) 9765-9773.
[142] Z. Ye, J.A. Padilla, E. Xuriguera, E. Brillas, I. Sirés, Applied Catalysis B: Environmental, (2020) 118604.
[143] K.-Y.A. Lin, H.-A. Chang, B.-J. Chen, Journal of Materials Chemistry A, 4 (2016) 13611-13625.
[144] Y. Su, S. Li, D. He, D. Yu, F. Liu, N. Shao, Z. Zhang, ACS Sustainable Chemistry & Engineering, 6 (2018) 11989-11998.
[145] E. Cho, J.J. Lee, B.-S. Lee, K.-W. Lee, B. Yeom, T.S. Lee, Chemosphere, 244 (2020) 125589.
[146] W. Ren, J. Gao, C. Lei, Y. Xie, H. Cai, Q. Ni, J. Yao, Chemical Engineering Journal, 349 (2018) 766-774.
[147] F. Ye, Q. Song, Z. Zhang, W. Li, S. Zhang, X. Yin, Y. Zhou, H. Tao, Y. Liu, L. Cheng, Advanced Functional Materials, 28 (2018) 1707205.
[148] B. Chen, Z. Yang, G. Ma, D. Kong, W. Xiong, J. Wang, Y. Zhu, Y. Xia, Microporous and Mesoporous Materials, 257 (2018) 1-8.
[149] J.-S. Li, S.-L. Li, Y.-J. Tang, K. Li, L. Zhou, N. Kong, Y.-Q. Lan, J.-C. Bao, Z.-H. Dai, Scientific reports, 4 (2014) 1-8.
[150] A. Aijaz, N. Fujiwara, Q. Xu, Journal of the American Chemical Society, 136 (2014) 6790-6793.
[151] H. Sun, Y. Wang, S. Liu, L. Ge, L. Wang, Z. Zhu, S. Wang, Chemical Communications, 49 (2013) 9914-9916.
[152] S. Wang, E. Iyyamperumal, A. Roy, Y. Xue, D. Yu, L. Dai, Angewandte Chemie International Edition, 50 (2011) 11756-11760.
[153] H. Jin, H. Zhou, D. He, Z. Wang, Q. Wu, Q. Liang, S. Liu, S. Mu, Applied Catalysis B: Environmental, 250 (2019) 143-149.
[154] J. Sheng, L. Wang, L. Deng, M. Zhang, H. He, K. Zeng, F. Tang, Y.-N. Liu, ACS applied materials & interfaces, 10 (2018) 7191-7200.
[155] A.A. Dubale, I.N. Ahmed, X.-H. Chen, C. Ding, G.-H. Hou, R.-F. Guan, X. Meng, X.-L. Yang, M.-H. Xie, Journal of materials chemistry A, 7 (2019) 6062-6079.
[156] B. Liu, L. Ye, R. Wang, J. Yang, Y. Zhang, R. Guan, L. Tian, X. Chen, ACS applied materials & interfaces, 10 (2018) 4001-4009.
[157] A. Aijaz, T. Akita, H. Yang, Q. Xu, Chemical Communications, 50 (2014) 6498-6501.
[158] W. Ma, N. Wang, T. Tong, L. Zhang, K.-Y.A. Lin, X. Han, Y. Du, Carbon, 137 (2018) 291-303.
[159] M.W. Logan, S. Ayad, J.D. Adamson, T. Dilbeck, K. Hanson, F.J. Uribe-Romo, Journal of Materials Chemistry A, 5 (2017) 11854-11863.

[160] F. Liu, W. Xiong, J. Liu, Q. Cheng, G. Cheng, L. Shi, Y. Zhang, Colloids and Surfaces A: Physicochemical and Engineering Aspects, 556 (2018) 72-80.
[161] X. Wang, W. Chen, L. Zhang, T. Yao, W. Liu, Y. Lin, H. Ju, J. Dong, L. Zheng, W. Yan, Journal of the American Chemical Society, 139 (2017) 9419-9422.
[162] A. Almasoudi, R. Mokaya, Journal of Materials Chemistry, 22 (2012) 146-152.
[163] Q. Wang, W. Xia, W. Guo, L. An, D. Xia, R. Zou, Chemistry–An Asian Journal, 8 (2013) 1879-1885.
[164] H.J. An, B.N. Bhadra, N.A. Khan, S.H. Jhung, Chemical Engineering Journal, 343 (2018) 447-454.
[165] J. Wang, S. Kaskel, Journal of Materials Chemistry, 22 (2012) 23710-23725.
[166] Y. Gong, X. Zhao, H. Zhang, B. Yang, K. Xiao, T. Guo, J. Zhang, H. Shao, Y. Wang, G. Yu, Applied Catalysis B: Environmental, 233 (2018) 35-45.
[167] M. Zhang, R. Luo, C. Wang, W. Zhang, X. Yan, X. Sun, L. Wang, J. Li, Journal of Materials Chemistry A, 7 (2019) 12547-12555.
[168] Q. Li, P. Xu, W. Gao, S. Ma, G. Zhang, R. Cao, J. Cho, H.L. Wang, G. Wu, Advanced materials, 26 (2014) 1378-1386.
[169] Y. Pan, Y. Zhao, S. Mu, Y. Wang, C. Jiang, Q. Liu, Q. Fang, M. Xue, S. Qiu, Journal of Materials Chemistry A, 5 (2017) 9544-9552.
[170] W.-T. Koo, S.-J. Choi, S.-J. Kim, J.-S. Jang, H.L. Tuller, I.-D. Kim, Journal of the American Chemical Society, 138 (2016) 13431-13437.
[171] C. Liu, L. Liu, X. Tian, Y. Wang, R. Li, Y. Zhang, Z. Song, B. Xu, W. Chu, F. Qi, Applied Catalysis B: Environmental, 255 (2019) 117763.
[172] G. Xu, B. Ding, L. Shen, P. Nie, J. Han, X. Zhang, Journal of Materials Chemistry A, 1 (2013) 4490-4496.
[173] C.Y. Hu, J. Zhou, C.Y. Sun, M.m. Chen, X.L. Wang, Z.M. Su, Chemistry–A European Journal, 25 (2019) 379-385.
[174] C. Zhou, Z. Zeng, G. Zeng, D. Huang, R. Xiao, M. Cheng, C. Zhang, W. Xiong, C. Lai, Y. Yang, Journal of hazardous materials, 380 (2019) 120815.
[175] W. Wang, Z. Zeng, G. Zeng, C. Zhang, R. Xiao, C. Zhou, W. Xiong, Y. Yang, L. Lei, Y. Liu, Chemical Engineering Journal, 378 (2019) 122132.
[176] B. Song, Z. Zeng, G. Zeng, J. Gong, R. Xiao, S. Ye, M. Chen, C. Lai, P. Xu, X. Tang, Advances in colloid and interface science, 272 (2019) 101999.
[177] J.-S. Jang, W.-T. Koo, S.-J. Choi, I.-D. Kim, Journal of the American Chemical Society, 139 (2017) 11868-11876.
[178] Y. Zhou, X. Li, J. Li, S. Yin, B. Shen, C. Li, P. Huo, H. Wang, Y. Yan, S. Yuan, Chemical Engineering Journal, 378 (2019) 122242.
[179] P. Wang, M. Shen, H. Zhou, C. Meng, A. Yuan, Small, 15 (2019) 1903522.
[180] N.L. Torad, Y. Li, S. Ishihara, K. Ariga, Y. Kamachi, H.-Y. Lian, H. Hamoudi, Y. Sakka, W. Chaikittisilp, K.C.-W. Wu, Chemistry Letters, 43 (2014) 717-719.
[181] Z. Luo, Y. He, D. Zhi, L. Luo, Y. Sun, E. Khan, L. Wang, Y. Peng, Y. Zhou, D.C. Tsang, Science of The Total Environment, 696 (2019) 133990.
[182] Y. He, Y. Xiang, Y. Zhou, Y. Yang, J. Zhang, H. Huang, C. Shang, L. Luo, J. Gao, L. Tang, Environmental research, 164 (2018) 288-301.
[183] Y. Zhou, Y. He, Y. Xiang, S. Meng, X. Liu, J. Yu, J. Yang, J. Zhang, P. Qin, L. Luo, Science of the Total Environment, 646 (2019) 29-36.
[184] I. Ahmed, N.A. Khan, S.H. Jhung, Inorganic Chemistry, 52 (2013) 14155-14161.
[185] M. Sarker, H.J. An, D.K. Yoo, S.H. Jhung, Chemical Engineering Journal, 338 (2018) 107-116.
[186] Z. Hasan, S.H. Jhung, Journal of hazardous materials, 283 (2015) 329-339.
[187] I. Ahmed, S.H. Jhung, Chemical Engineering Journal, 310 (2017) 197-215.
[188] M. Sarker, B.N. Bhadra, P.W. Seo, S.H. Jhung, Journal of hazardous materials, 324 (2017) 131-138.
[189] B.N. Bhadra, J.Y. Song, S.-K. Lee, Y.K. Hwang, S.H. Jhung, Journal of hazardous materials, 344 (2018) 1069-1077.
[190] B.N. Bhadra, S.H. Jhung, Microporous and Mesoporous Materials, 270 (2018) 102-108.

[191] I. Ahmed, B.N. Bhadra, H.J. Lee, S.H. Jhung, Catalysis Today, 301 (2018) 90-97.
[192] S. Xu, Y. Lv, X. Zeng, D. Cao, Chemical Engineering Journal, 323 (2017) 502-511.
[193] S. Huang, H. Pang, L. Li, S. Jiang, T. Wen, L. Zhuang, B. Hu, X. Wang, Chemical Engineering Journal, 353 (2018) 157-166.
[194] Z. Lv, Q. Fan, Y. Xie, Z. Chen, A. Alsaedi, T. Hayat, X. Wang, C. Chen, Chemical Engineering Journal, 362 (2019) 413-421.
[195] W. Xiong, Z. Zeng, G. Zeng, Z. Yang, R. Xiao, X. Li, J. Cao, C. Zhou, H. Chen, M. Jia, Chemical Engineering Journal, 374 (2019) 91-99.
[196] I. Ahmed, T. Panja, N.A. Khan, M. Sarker, J.-S. Yu, S.H. Jhung, ACS applied materials & interfaces, 9 (2017) 10276-10285.
[197] B.N. Bhadra, J.K. Lee, C.-W. Cho, S.H. Jhung, Chemical Engineering Journal, 343 (2018) 225-234.
[198] Z. Lv, H. Wang, C. Chen, S. Yang, L. Chen, A. Alsaedi, T. Hayat, Journal of colloid and interface science, 537 (2019) A1-A10.
[199] B.N. Bhadra, S.H. Jhung, Journal of hazardous materials, 340 (2017) 179-188.
[200] B.N. Bhadra, I. Ahmed, S. Kim, S.H. Jhung, Chemical Engineering Journal, 314 (2017) 50-58.
[201] Q. Wen, J. Di, Y. Zhao, Y. Wang, L. Jiang, J. Yu, Chemical Science, 4 (2013) 4378-4382.
[202] C. Wang, J. Kim, J. Tang, M. Kim, H. Lim, V. Malgras, J. You, Q. Xu, J. Li, Y. Yamauchi, Chem, 6 (2020) 19-40.
[203] J. Qin, J. Wang, J. Yang, Y. Hu, M. Fu, D. Ye, Applied Catalysis B: Environmental, 267 (2020) 118667.
[204] S. Ye, M. Yan, X. Tan, J. Liang, G. Zeng, H. Wu, B. Song, C. Zhou, Y. Yang, H. Wang, Applied Catalysis B: Environmental, 250 (2019) 78-88.
[205] H. Yi, M. Yan, D. Huang, G. Zeng, C. Lai, M. Li, X. Huo, L. Qin, S. Liu, X. Liu, Applied Catalysis B: Environmental, 250 (2019) 52-62.
[206] Y. Yang, C. Zhang, D. Huang, G. Zeng, J. Huang, C. Lai, C. Zhou, W. Wang, H. Guo, W. Xue, Applied Catalysis B: Environmental, 245 (2019) 87-99.
[207] Y. Zhang, J. Zhou, X. Chen, Q. Feng, W. Cai, Journal of Alloys and Compounds, 777 (2019) 109-118.
[208] K. Park, Q. Zhang, B.B. Garcia, X. Zhou, Y.H. Jeong, G. Cao, Advanced Materials, 22 (2010) 2329-2332.
[209] P. Liang, C. Zhang, H. Sun, S. Liu, M. Tadé, S. Wang, RSC Advances, 6 (2016) 95903-95909.
[210] H. Xiao, W. Zhang, Q. Yao, L. Huang, L. Chen, B. Boury, Z. Chen, Applied Catalysis B: Environmental, 244 (2019) 719-731.
[211] B. Hu, J.-Y. Yuan, J.-Y. Tian, M. Wang, X. Wang, L. He, Z. Zhang, Z.-W. Wang, C.-S. Liu, Journal of colloid and interface science, 531 (2018) 148-159.
[212] F. Zhang, Y. Zhang, G. Zhang, Z. Yang, D.D. Dionysiou, A. Zhu, Applied Catalysis B: Environmental, 236 (2018) 53-63.
[213] Y. Pi, S. Jin, X. Li, S. Tu, Z. Li, J. Xiao, Applied Catalysis B: Environmental, 256 (2019) 117882.
[214] N. Salehifar, Z. Zarghami, M. Ramezani, Materials Letters, 167 (2016) 226-229.
[215] Y. Yang, C. Zhang, C. Lai, G. Zeng, D. Huang, M. Cheng, J. Wang, F. Chen, C. Zhou, W. Xiong, Advances in colloid and interface science, 254 (2018) 76-93.
[216] Y. Lei, C.-S. Chen, Y.-J. Tu, Y.-H. Huang, H. Zhang, Environmental science & technology, 49 (2015) 6838-6845.
[217] Z. Ye, J.A. Padilla, E. Xuriguera, E. Brillas, I. Sirés, Applied Catalysis B: Environmental, 266 (2020) 118604.
[218] Y. Yao, H. Chen, C. Lian, F. Wei, D. Zhang, G. Wu, B. Chen, S. Wang, Journal of hazardous materials, 314 (2016) 129-139.
[219] J. Tang, J. Wang, Chemical Engineering Journal, 375 (2019) 122007.
[220] D. Chen, S. Chen, Y. Jiang, S. Xie, H. Quan, L. Hua, X. Luo, L. Guo, RSC Advances, 7 (2017) 49024-49030.

[221] W. Li, X. Wu, S. Li, W. Tang, Y. Chen, Applied Surface Science, 436 (2018) 252-262.
[222] K. Li, Y. Zhao, M.J. Janik, C. Song, X. Guo, Applied Surface Science, 396 (2017) 1383-1392.
[223] C. Bao, H. Zhang, L. Zhou, Y. Shao, J. Ma, Q. Wu, RSC Advances, 5 (2015) 72423-72432.
[224] N. Wang, Y. Du, W. Ma, P. Xu, X. Han, Applied Catalysis B: Environmental, 210 (2017) 23-33.
[225] K. Liu, M. Yu, H. Wang, J. Wang, W. Liu, M.R. Hoffmann, Environmental science & technology, 53 (2019) 6474-6482.
[226] M. Cheng, C. Lai, Y. Liu, G. Zeng, D. Huang, C. Zhang, L. Qin, L. Hu, C. Zhou, W. Xiong, Coordination Chemistry Reviews, 368 (2018) 80-92.
[227] C. Wang, H. Wang, R. Luo, C. Liu, J. Li, X. Sun, J. Shen, W. Han, L. Wang, Chemical Engineering Journal, 330 (2017) 262-271.
[228] N. Wang, W. Ma, Z. Ren, Y. Du, P. Xu, X. Han, Journal of Materials Chemistry A, 6 (2018) 884-895.
[229] G. Yilmaz, C.F. Tan, M. Hong, G.W. Ho, Advanced Functional Materials, 28 (2018) 1704177.
[230] J. Nai, X.W. Lou, Advanced Materials, 31 (2019) 1706825.
[231] W.-D. Oh, Z. Dong, T.-T. Lim, Applied Catalysis B: Environmental, 194 (2016) 169-201.
[232] X. Li, Z. Wang, B. Zhang, A.I. Rykov, M.A. Ahmed, L. Wang, Applied Catalysis B: Environmental, 181 (2016) 788-799.
[233] L. Chen, X. Zuo, S. Yang, T. Cai, D. Ding, Chemical Engineering Journal, 359 (2019) 373-384.
[234] R. Jiang, L. Li, T. Sheng, G. Hu, Y. Chen, L. Wang, Journal of the American Chemical Society, 140 (2018) 11594-11598.
[235] S. Zhang, H. Gao, X. Xu, R. Cao, H. Yang, X. Xu, J. Li, Chemical Engineering Journal, 381 (2020) 122670.
[236] Y. Liu, X. Chen, Y. Yang, Y. Feng, L. Wu, S. Mao, Chemical Engineering Journal, 358 (2019) 408-418.
[237] P. Liang, C. Zhang, X. Duan, H. Sun, S. Liu, M.O. Tade, S. Wang, Environmental Science: Nano, 4 (2017) 315-324.
[238] U. Von Gunten, Water research, 37 (2003) 1443-1467.
[239] H.V. Lutze, N. Kerlin, T.C. Schmidt, Water research, 72 (2015) 349-360.
[240] Y. Wang, J. Le Roux, T. Zhang, J.-P. Croué, Environmental science & technology, 48 (2014) 14534-14542.
[241] J. Liao, B. Jin, Y. Zhao, Z. Liang, Chemical Engineering Journal, 372 (2019) 1028-1037.
[242] S. Salehi, M. Anbia, Applied Organometallic Chemistry, 32 (2018) e4390.
[243] D.-D. Zhou, X.-W. Zhang, Z.-W. Mo, Y.-Z. Xu, X.-Y. Tian, Y. Li, X.-M. Chen, J.-P. Zhang, EnergyChem, 1 (2019) 100016.
[244] M. Nandi, K. Okada, A. Dutta, A. Bhaumik, J. Maruyama, D. Derks, H. Uyama, Chemical Communications, 48 (2012) 10283-10285.
[245] W. Xing, C. Liu, Z. Zhou, J. Zhou, G. Wang, S. Zhuo, Q. Xue, L. Song, Z. Yan, Nanoscale research letters, 9 (2014) 1-8.
[246] C. Chen, J. Kim, W.-S. Ahn, Fuel, 95 (2012) 360-364.
[247] G. Lim, K.B. Lee, H.C. Ham, The Journal of Physical Chemistry C, 120 (2016) 8087-8095.
[248] X. Ma, L. Li, R. Chen, C. Wang, H. Li, S. Wang, Applied Surface Science, 435 (2018) 494-502.
[249] W. Kukulka, K. Cendrowski, B. Michalkiewicz, E. Mijowska, RSC Advances, 9 (2019) 18527-18537.
[250] S. Gadipelli, W. Travis, W. Zhou, Z. Guo, Energy & Environmental Science, 7 (2014) 2232-2238.
[251] K.K. Tanabe, S.M. Cohen, Chemical Society Reviews, 40 (2011) 498-519.
[252] M.L. Foo, R. Matsuda, S. Kitagawa, Chemistry of materials, 26 (2013) 310-322.

[253] J. Wang, J. Yang, R. Krishna, T. Yang, S. Deng, Journal of Materials Chemistry A, 4 (2016) 19095-19106.
[254] S. Duncan, K.G. Sexton, B. Turpin, Indoor air, 28 (2018) 198-212.
[255] Y.M. Kim, S. Harrad, R.M. Harrison, Environmental science & technology, 35 (2001) 997-1004.
[256] D.R. Gentner, R.A. Harley, A.M. Miller, A.H. Goldstein, Environmental science & technology, 43 (2009) 4247-4252.
[257] O. Karatum, M.A. Deshusses, Chemical Engineering Journal, 294 (2016) 308-315.
[258] M.V. Gallegos, M.A. Peluso, E. Finocchio, H.J. Thomas, G. Busca, J.E. Sambeth, Chemical Engineering Journal, 313 (2017) 1099-1111.
[259] S.C. Kim, W.G. Shim, Applied Catalysis B: Environmental, 98 (2010) 180-185.
[260] N. Li, F. Gaillard, Applied Catalysis B: Environmental, 88 (2009) 152-159.
[261] Q. Wang, Z. Li, M.A. Bañares, L.T. Weng, Q. Gu, J. Price, W. Han, K.L. Yeung, Small, 15 (2019) 1903525.
[262] J. Zhao, Z. Tang, F. Dong, J. Zhang, Molecular Catalysis, 463 (2019) 77-86.
[263] X. Chen, S. Cai, J. Chen, W. Xu, H. Jia, J. Chen, Chemical Engineering Journal, 334 (2018) 768-779.
[264] H. Zhao, J. Ma, Q. Zhang, Z. Liu, R. Li, Industrial & Engineering Chemistry Research, 53 (2014) 13810-13819.
[265] Y. Rao, M. Trudeau, D. Antonelli, Journal of the American Chemical Society, 128 (2006) 13996-13997.
[266] X. Liu, J. Wang, J. Zeng, X. Wang, T. Zhu, RSC Advances, 5 (2015) 52066-52071.
[267] J. Li, W. Li, G. Liu, Y. Deng, J. Yang, Y. Chen, Catalysis Letters, 146 (2016) 1300-1308.
[268] X. Zhang, X. Lv, F. Bi, G. Lu, Y. Wang, Molecular Catalysis, 482 (2020) 110701.
[269] X. Chen, E. Yu, S. Cai, H. Jia, J. Chen, P. Liang, Chemical Engineering Journal, 344 (2018) 469-479.
[270] X. Chen, S. Cai, E. Yu, J. Chen, H. Jia, Applied Surface Science, 475 (2019) 312-324.
[271] H. Sun, X. Yu, X. Ma, X. Yang, M. Lin, M. Ge, Catalysis Today, (2019).
[272] X. Feng, C. Chen, C. He, S. Chai, Y. Yu, J. Cheng, Journal of hazardous materials, 383 (2020) 121143.
[273] K. Vellingiri, K.-H. Kim, A. Pournara, A. Deep, Progress in Materials Science, 94 (2018) 1-67.
[274] I. Statistics, Key world energy statistics, 2014.
[275] M.I. Hoffert, K. Caldeira, G. Benford, D.R. Criswell, C. Green, H. Herzog, A.K. Jain, H.S. Kheshgi, K.S. Lackner, J.S. Lewis, science, 298 (2002) 981-987.
[276] R.P. Rechard, G.A. Freeze, F.V. Perry, Reliability Engineering & System Safety, 122 (2014) 74-95.
[277] S. Zhong, Q. Wang, D. Cao, Scientific reports, 6 (2016) 21295.
[278] Y. Gong, Y. Tang, Z. Mao, X. Wu, Q. Liu, S. Hu, S. Xiong, X. Wang, Journal of Materials Chemistry A, 6 (2018) 13696-13704.
[279] L. Chen, P.S. Reiss, S.Y. Chong, D. Holden, K.E. Jelfs, T. Hasell, M.A. Little, A. Kewley, M.E. Briggs, A. Stephenson, Nature materials, 13 (2014) 954-960.
[280] P.K. Thallapally, J.W. Grate, R.K. Motkuri, Chemical communications, 48 (2012) 347-349.
[281] J. Liu, D.M. Strachan, P.K. Thallapally, Chemical Communications, 50 (2014) 466-468.
[282] Y. Chen, Z. Shen, Q. Jia, J. Zhao, Z. Zhao, H. Ji, RSC Advances, 6 (2016) 2504-2511.
[283] C. Grelet, C. Bastin, M. Gelé, J.-B. Davière, M. Johan, A. Werner, R. Reding, J.F. Pierna, F. Colinet, P. Dardenne, Journal of dairy science, 99 (2016) 4816-4825.
[284] Y. Li, W. Luo, N. Qin, J. Dong, J. Wei, W. Li, S. Feng, J. Chen, J. Xu, A.A. Elzatahry, Angewandte Chemie International Edition, 53 (2014) 9035-9040.

[285] N. Ramgir, S.K. Ganapathi, M. Kaur, N. Datta, K. Muthe, D. Aswal, S. Gupta, J. Yakhmi, Sensors and Actuators B: Chemical, 151 (2010) 90-96.
[286] W.H. Organization, Air quality guidelines: global update 2005: particulate matter, ozone, nitrogen dioxide, and sulfur dioxide, World Health Organization, 2006.
[287] D. Ding, Q. Xue, W. Lu, Y. Xiong, J. Zhang, X. Pan, B. Tao, Sensors and Actuators B: Chemical, 259 (2018) 289-298.
[288] M. Wang, T. Hou, Z. Shen, X. Zhao, H. Ji, Sensors and Actuators B: Chemical, 292 (2019) 171-179.
[289] M. Wang, T. Hou, X. Zhao, H. Yu, H. Ji, Materials Letters, 242 (2019) 83-86.
[290] W. Li, X. Wu, N. Han, J. Chen, X. Qian, Y. Deng, W. Tang, Y. Chen, Sensors and Actuators B: Chemical, 225 (2016) 158-166.
[291] W. Li, X. Wu, N. Han, J. Chen, W. Tang, Y. Chen, Powder technology, 304 (2016) 241-247.
[292] X.-Z. Song, Y.-L. Meng, Z. Tan, L. Qiao, T. Huang, X.-F. Wang, Inorganic chemistry, 56 (2017) 13646-13650.
[293] Y. Cui, W. Jiang, S. Liang, L. Zhu, Y. Yao, Journal of Materials Chemistry A, 6 (2018) 14930-14938.
[294] X.-F. Wang, W. Ma, F. Jiang, E.-S. Cao, K.-M. Sun, L. Cheng, X.-Z. Song, Chemical Engineering Journal, 338 (2018) 504-512.
[295] X. Dong, Y. Su, T. Lu, L. Zhang, L. Wu, Y. Lv, Sensors and Actuators B: Chemical, 258 (2018) 349-357.
[296] K. Tian, X.-X. Wang, Z.-Y. Yu, H.-Y. Li, X. Guo, ACS applied materials & interfaces, 9 (2017) 29669-29676.
[297] W. Zhou, Y.-P. Wu, J. Zhao, W.-W. Dong, X.-Q. Qiao, D.-F. Hou, X. Bu, D.-S. Li, Inorganic chemistry, 56 (2017) 14111-14117.
[298] Z. Yang, D. Zhang, H. Chen, Sensors and Actuators B: Chemical, 300 (2019) 127037.
[299] M. Aslam, I.M. Ismail, T. Almeelbi, N. Salah, S. Chandrasekaran, A. Hameed, Chemosphere, 117 (2014) 115-123.
[300] D. Moreno-González, A.M. Hamed, P. Gilbert-López, L. Gámiz-Gracia, A.M. García-Campaña, Journal of Chromatography A, 1510 (2017) 100-107.
[301] Y. He, R. Peng, Nanotechnology, 25 (2014) 455502.
[302] L.R. Guidi, F.A. Santos, A.C.S. Ribeiro, C. Fernandes, L.H. Silva, M.B.A. Gloria, Food chemistry, 245 (2018) 1232-1238.
[303] M. Mei, X. Huang, J. Yu, D. Yuan, Talanta, 134 (2015) 89-97.
[304] X. Pang, C. Cui, M. Su, Y. Wang, Q. Wei, W. Tan, Nano energy, 46 (2018) 101-109.
[305] X. Ren, H. Ma, T. Zhang, Y. Zhang, T. Yan, B. Du, Q. Wei, ACS applied materials & interfaces, 9 (2017) 37637-37644.
[306] S. Singh, N. Kumar, M. Kumar, A. Agarwal, B. Mizaikoff, Chemical engineering journal, 313 (2017) 283-292.
[307] D. Song, X. Jiang, Y. Li, X. Lu, S. Luan, Y. Wang, Y. Li, F. Gao, Journal of hazardous materials, 373 (2019) 367-376.
[308] Y. Cao, L. Wang, C. Wang, D. Su, Y. Liu, X. Hu, Microchimica Acta, 186 (2019) 481.
[309] M. Wang, Y. Liu, L. Yang, K. Tian, L. He, Z. Zhang, Q. Jia, Y. Song, S. Fang, Sensors and Actuators B: Chemical, 281 (2019) 1063-1072.
[310] Y. Feng, T. Yan, T. Wu, N. Zhang, Q. Yang, M. Sun, L. Yan, B. Du, Q. Wei, Sensors and Actuators B: Chemical, 298 (2019) 126817.
[311] C. Blöcher, J. Dorda, V. Mavrov, H. Chmiel, N. Lazaridis, K. Matis, Water Research, 37 (2003) 4018-4026.
[312] O. Gyliene, R. Rekertas, M. Šalkauskas, Water Research, 36 (2002) 4128-4136.
[313] D. Sud, G. Mahajan, M. Kaur, Bioresource technology, 99 (2008) 6017-6027.
[314] Z. Zhang, H. Ji, Y. Song, S. Zhang, M. Wang, C. Jia, J.-Y. Tian, L. He, X. Zhang, C.-S. Liu, Biosensors and Bioelectronics, 94 (2017) 358-364.
[315] L. Xiao, H. Xu, S. Zhou, T. Song, H. Wang, S. Li, W. Gan, Q. Yuan, Electrochimica Acta, 143 (2014) 143-151.
[316] W.H. Organization, Distribution and Sales, Geneva, 27 (2011).

[317] Z. Zhao, Z. Zhang, C. Li, H. Wu, J. Wang, Y. Lu, Journal of Materials Chemistry A, 6 (2018) 16164-16169.
[318] Y. Xiong, L. Su, H. Yang, P. Zhang, F. Ye, New Journal of Chemistry, 39 (2015) 9221-9227.
[319] Y. Wang, R.-P. Liang, J.-D. Qiu, Analytical Chemistry, 92 (2019) 2339-2346.

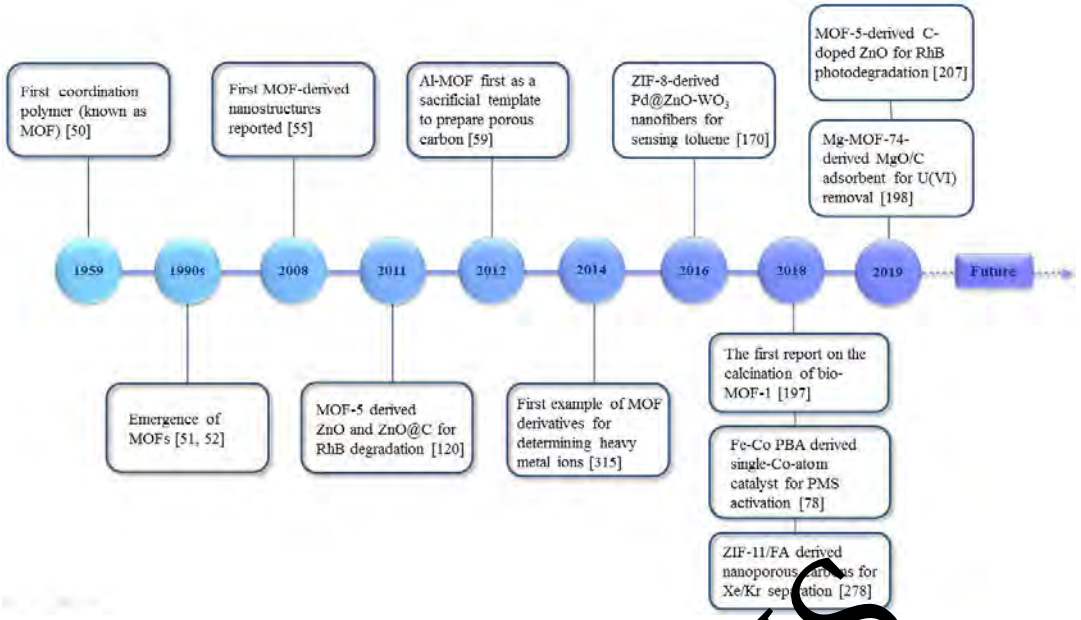

Fig. 1. Timeline of the important breakthroughs of MOF-derived nanomaterials in the environmental field.

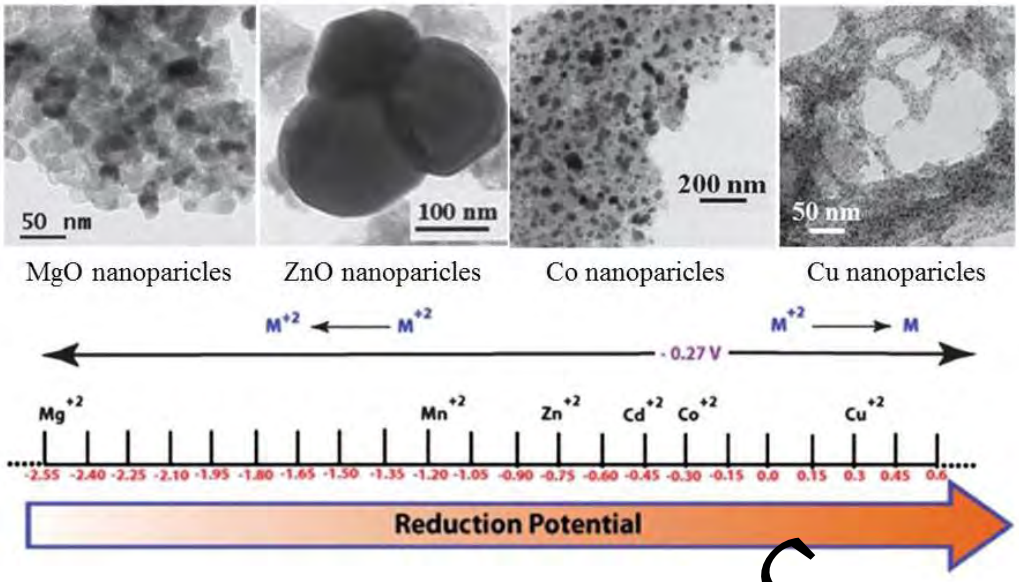

2382

2383 **Fig. 2.** The effect of reduction potential of metal atoms present in the MOFs on the formation of the

2384 metal/metal oxide nanoparticles. Metals having a reduction potential above -0.27 V undergo

2385 thermolysis in an N_2 atmosphere to give pure metal nanoparticles, whereas metals with reduction

2386 potential less than -0.27 V, even in an N_2 atmosphere, produces metal oxides only. Reproduced with

2387 permission from Ref. [93] Copyright 2012 The Royal Society of Chemistry.

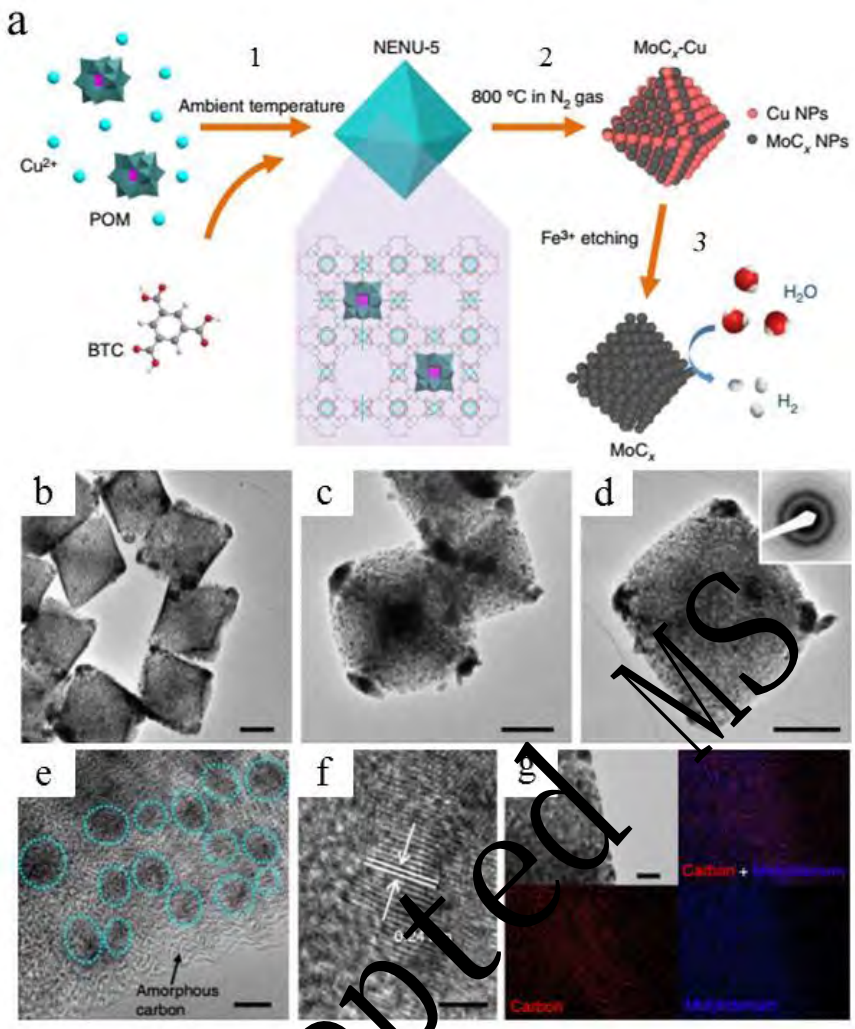

Fig. 3. (a) Schematic illustration of the synthesis procedure for porous MoC_x nano-octahedrons. (1) synthesis of NENU-5 nano-octahedrons with Mo-based POMs residing in the pores of HKUST-1 host. (2) formation of MoC_x-Cu nano-octahedrons after annealing at 800 °C. (3) removal of metallic Cu nanoparticles by Fe^{3+} etching to produce porous MoC_x nano-octahedrons. (b-d) TEM images of MoC_x nano-octahedrons (scale bar, 200 nm; inset in (c): SAED pattern). (e) magnified TEM image (scale bar, 5 nm), (f) HRTEM image (scale bar, 2 nm) and (g) elemental mapping (red: carbon; blue: molybdenum; scale bar, 50 nm) of porous MoC_x nano-octahedrons. Reproduced with permission from Ref. [103] Copyright 2015 Nature Publishing Group.

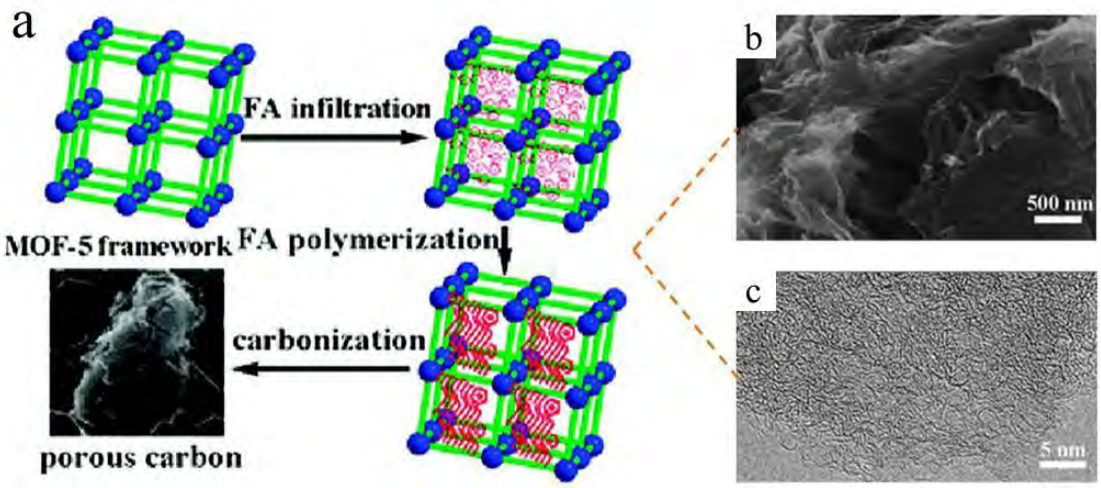

Fig. 4. (a) Schematic illustration of the synthesis procedure of NPC; (b) SEM and (c) HRTEM images of NPC. Reprinted with permission from Ref. [55] Copyright 2008 American Chemical Society.

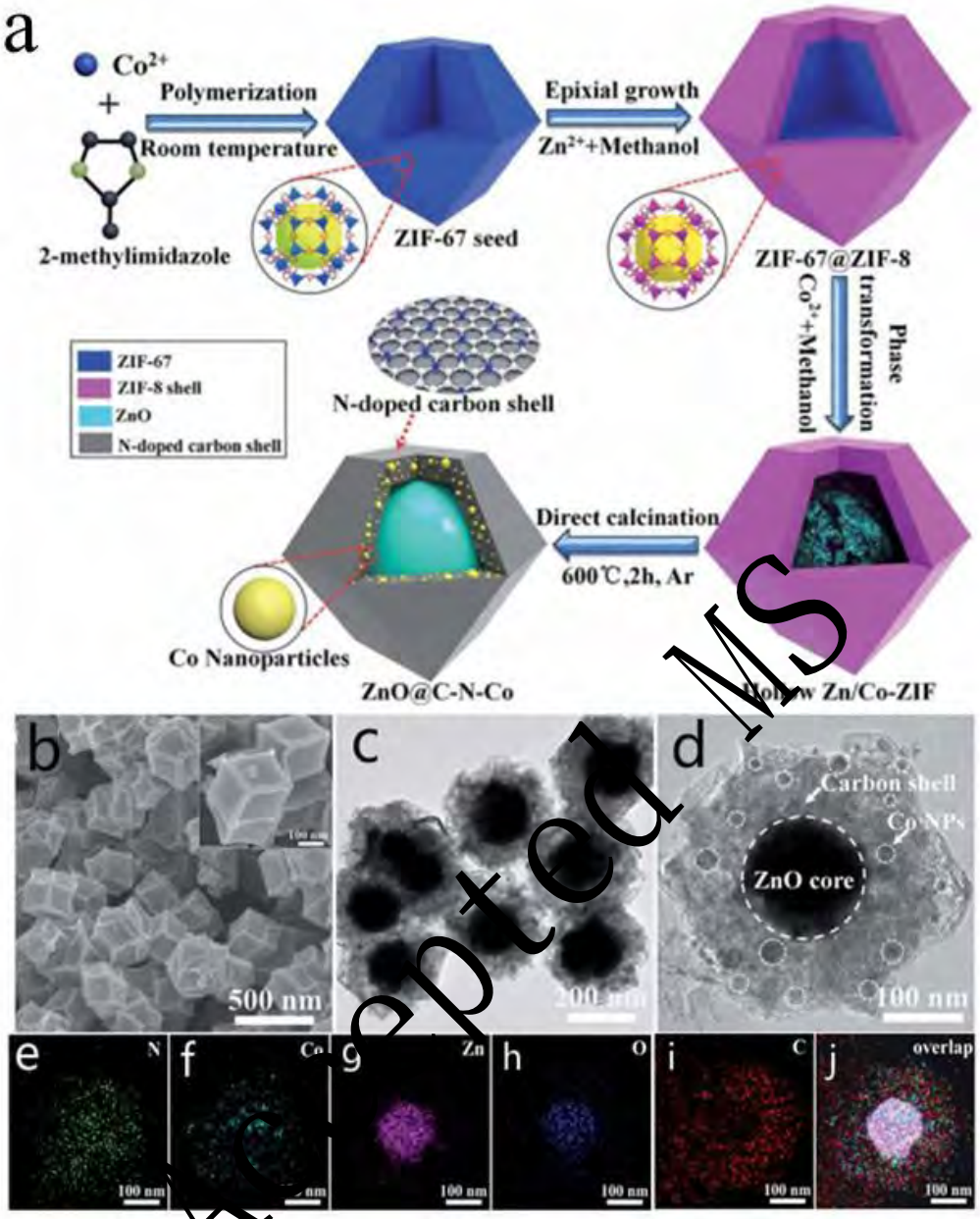

2401

2402 **Fig. 5.** (a) Schematic illustration of the preparation of core-shell ZnO@C-N-Co; (b) SEM image of

2403 the as-synthesized core-shell ZnO@C-N-Co (inset in (b): high magnification SEM image of

2404 ZnO@C-N-Co); (c) and (d) TEM images of ZnO@C-N-Co; (e–j) EDS mappings of the ZnO@C-

2405 N-Co. Reprinted with permission from Ref. [139] Copyright 2017 The Royal Society of Chemistry.

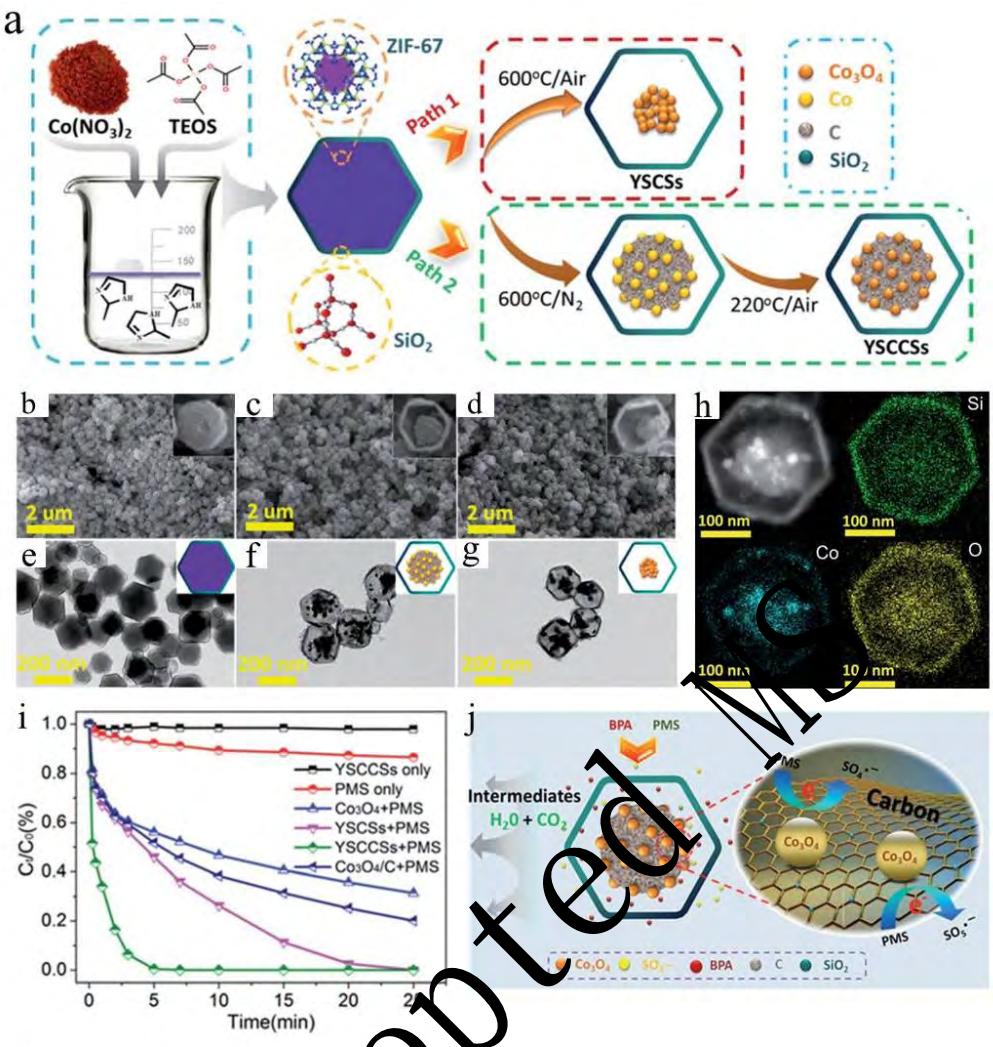

Fig. 6. (a) Illustration of the preparation process of the ZIF-67@SiO_2, YSCSs and YSCCSs. (b-d) SEM images of ZIF-67@SiO_2, YSCCSs and YSCSs (top-right inset: the enlarged SEM images of the broken structure); (e-g) TEM images of ZIF-67@SiO_2, YSCCSs and YSCSs (top-right insets: the corresponding schematic diagram); (h) EDX line scan and elemental mapping in the yolk-shell structure; (i) BPA degradation efficiency in different reaction systems within 25 min; (reaction conditions: BPA = 20 mg L^{-1}, PMS = 0.1 g L^{-1}, catalyst = 0.1 g L^{-1}, and T = 298 K). (j) the possible synergistic mechanisms of BPA degradation in the YSCCSs. Reprinted with permission from Ref. [140] Copyright 2018 The Royal Society of Chemistry.

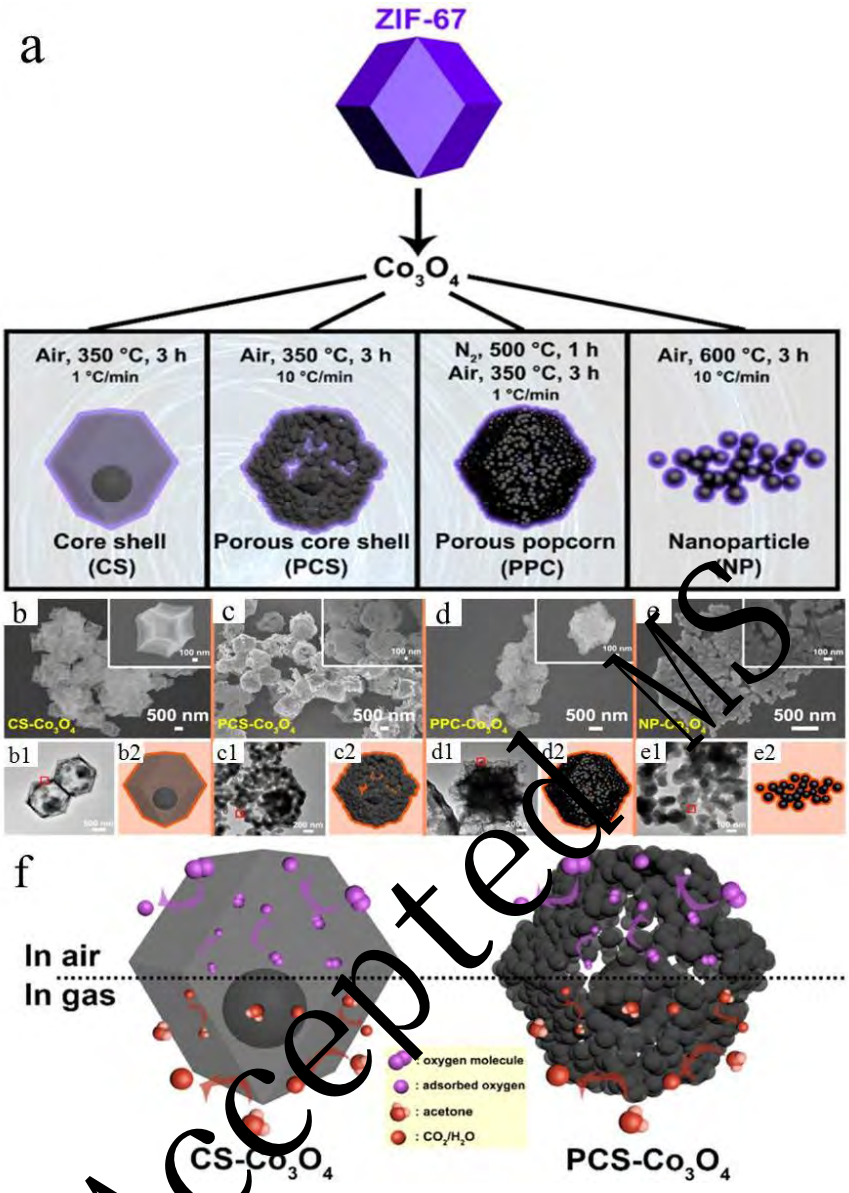

Fig. 7. (a) Schematic illustration of the formation of different Co_3O_4 structures. SEM images of the as-synthesized Co_3O_4 products derived from ZIF-67: (b) CS-Co_3O_4, (c) PCS-Co_3O_4, (d) PPC-Co_3O_4, and (e) NP-Co_3O_4; (b1-e1) TEM image of various Co_3O_4 structures; (b2-e2) corresponding ideal geometrical models of individual Co_3O_4 structures; (f) schematic of sensing mechanism of Co_3O_4 samples. Reprinted with permission from Ref. [141] Copyright 2018 American Chemical Society.

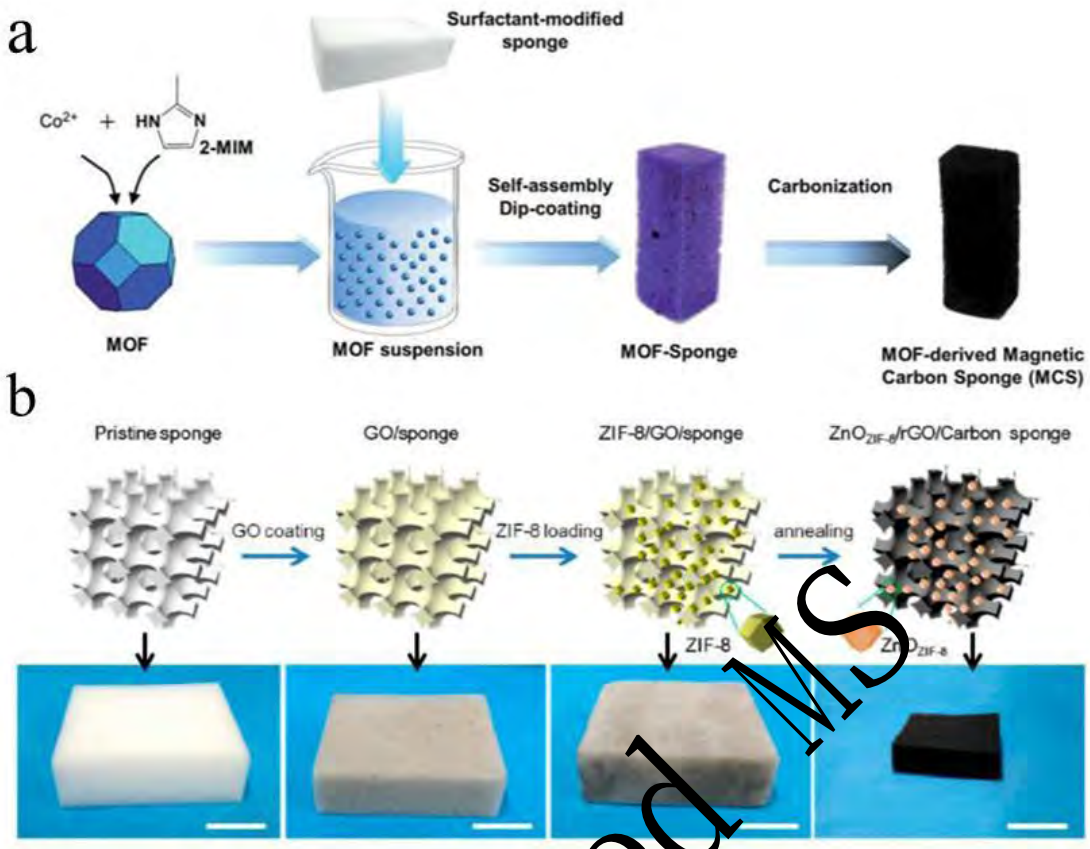

Fig. 8. (a) Preparation scheme of MCS. Reprinted with permission from Ref. [143] Copyright 2016 The Royal Society of Chemistry. (b) schematic illustration of the fabrication process. Reprinted with permission from Ref. [144] Copyright 2018 American Chemical Society.

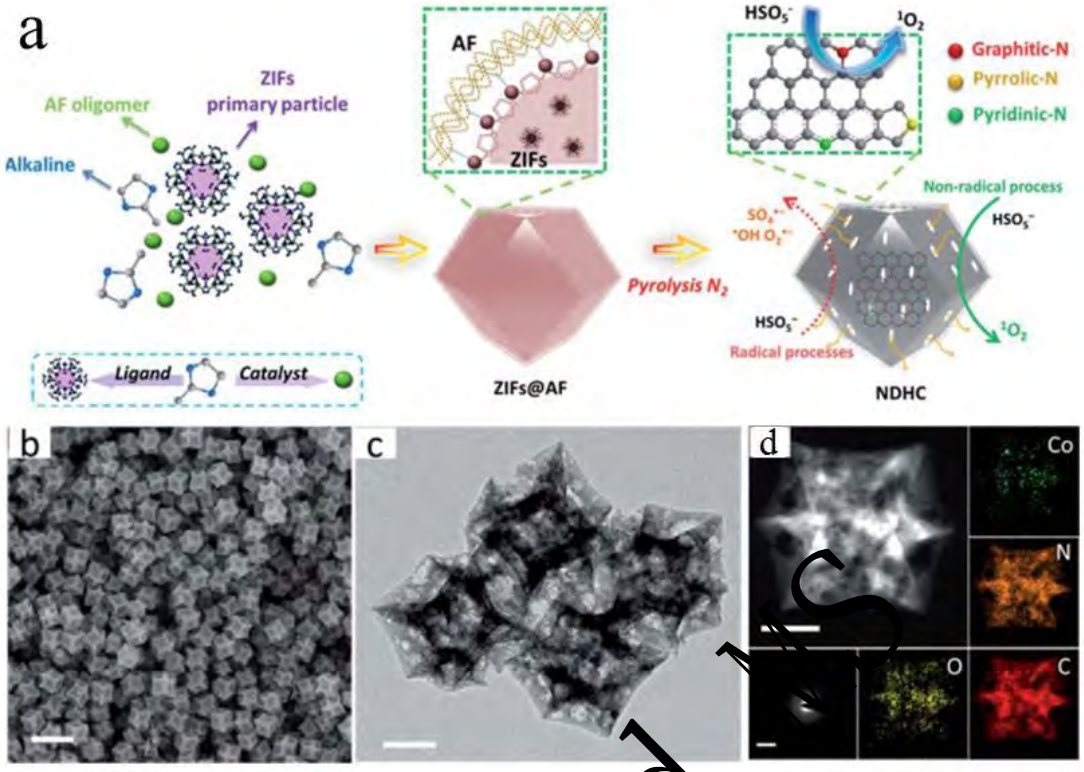

2425

2426 **Fig. 9.** (a) Illustration of the preparation process of NDHC; (b) SEM and (c) TEM images of NDHC-

2427 9; (d) the enlarged HAADF-STEM image, elemental maps. Reprinted with permission from Ref.

2428 [167] Copyright 2019 The Royal Society of Chemistry.

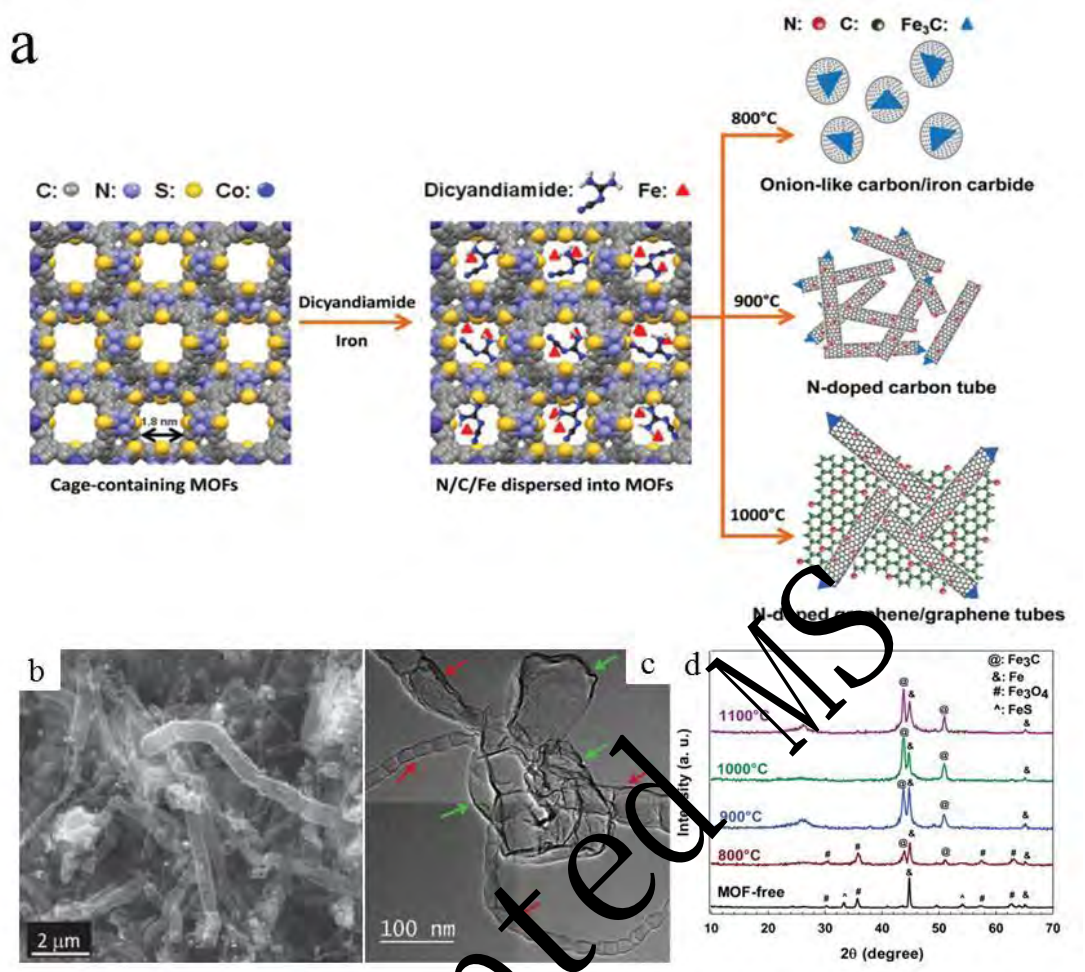

Fig. 10. (a) schematic illustration of formation of the carbon nanostructures found in the N-Fe-MOF catalysts synthesized at different heating temperatures; (b) SEM and (c) representative TEM images of the N-Fe-MOF catalyst prepared at 1000 °C with dominant graphene (green arrows) and graphenetube (red arrows) nanostructures; (d) X-Ray Diffraction (XRD) patterns of the MOF-free N-Fe and the N-Fe-MOF catalysts as a function of heating temperature. Reprinted with permission from Ref. [168] Copyright 2014 WILEY-VCH.

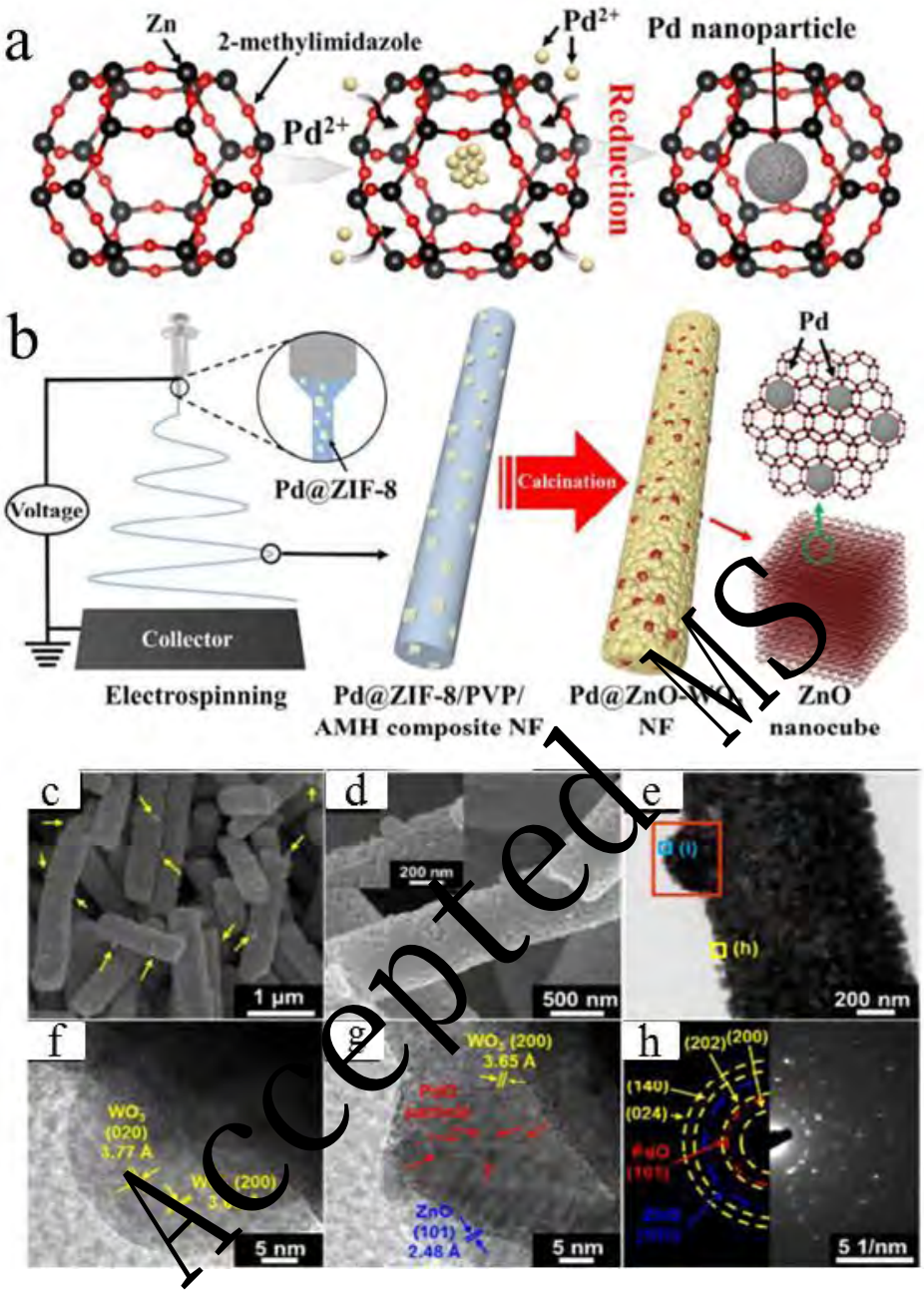

Fig. 11. Schematic illustration of (a) Pd NP encapsulation in the cavity of ZIF-8 and (b) synthetic process for the Pd@ZnO-WO_3 NFs; (c, d) SEM images of Pd@ZnO-WO_3 NFs (inset: magnified image of surface; (e) TEM image of Pd@ZnO-WO_3 NF; (f, g) HRTEM images of Pd@ZnO-WO_3 NF, and (h) SAED pattern of Pd@ZnOWO_3 NFs. Reprinted with permission from Ref. [170] Copyright 2016 American Chemical Society.

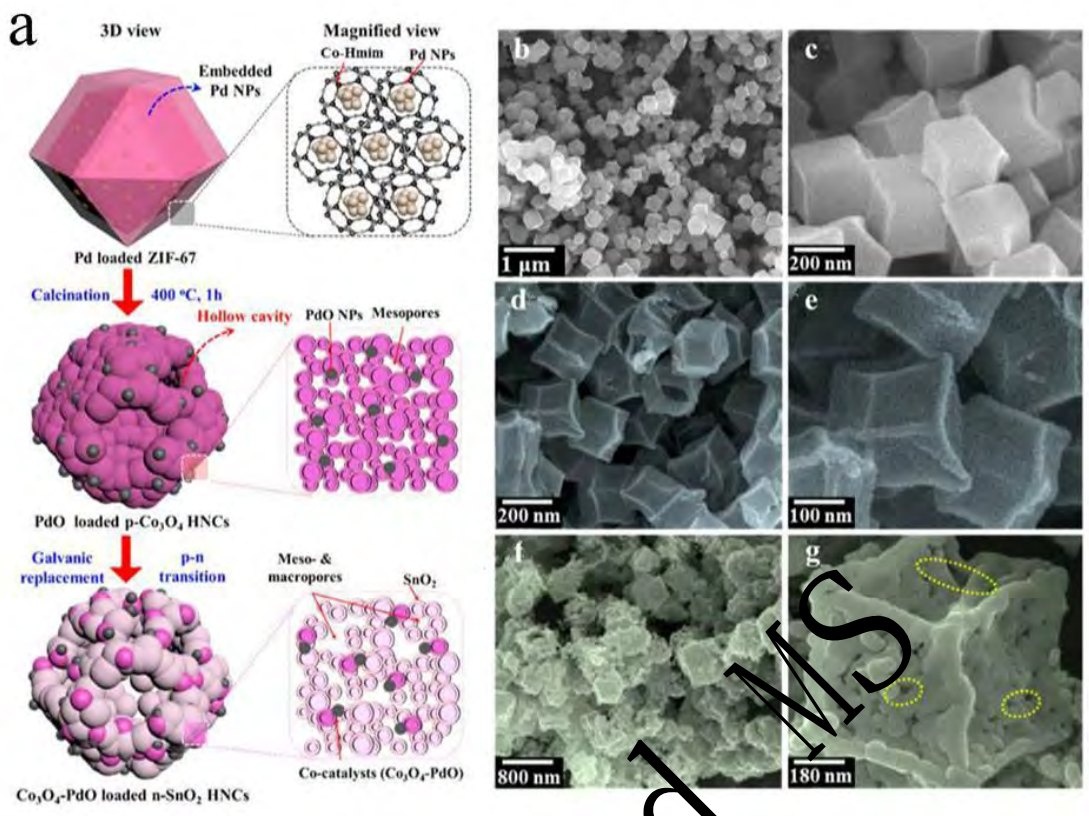

Fig. 12. Schematic illustration of synthetic process for the n-SnO_2 HNCs functionalized with Co_3O_4 and PdO. (b) SEM images of Pd NPs encapsulated ZIF-67. (c) magnified SEM images of Pd encapsulated ZIF-67. (d, e) SEM images of PdO loaded p-Co_3O_4 HNCs. (f, g) SEM images of Co_3O_4-PdO loaded n-SnO_2 HNCs. Reprinted with permission from Ref. [177] Copyright 2017 American Chemical Society.

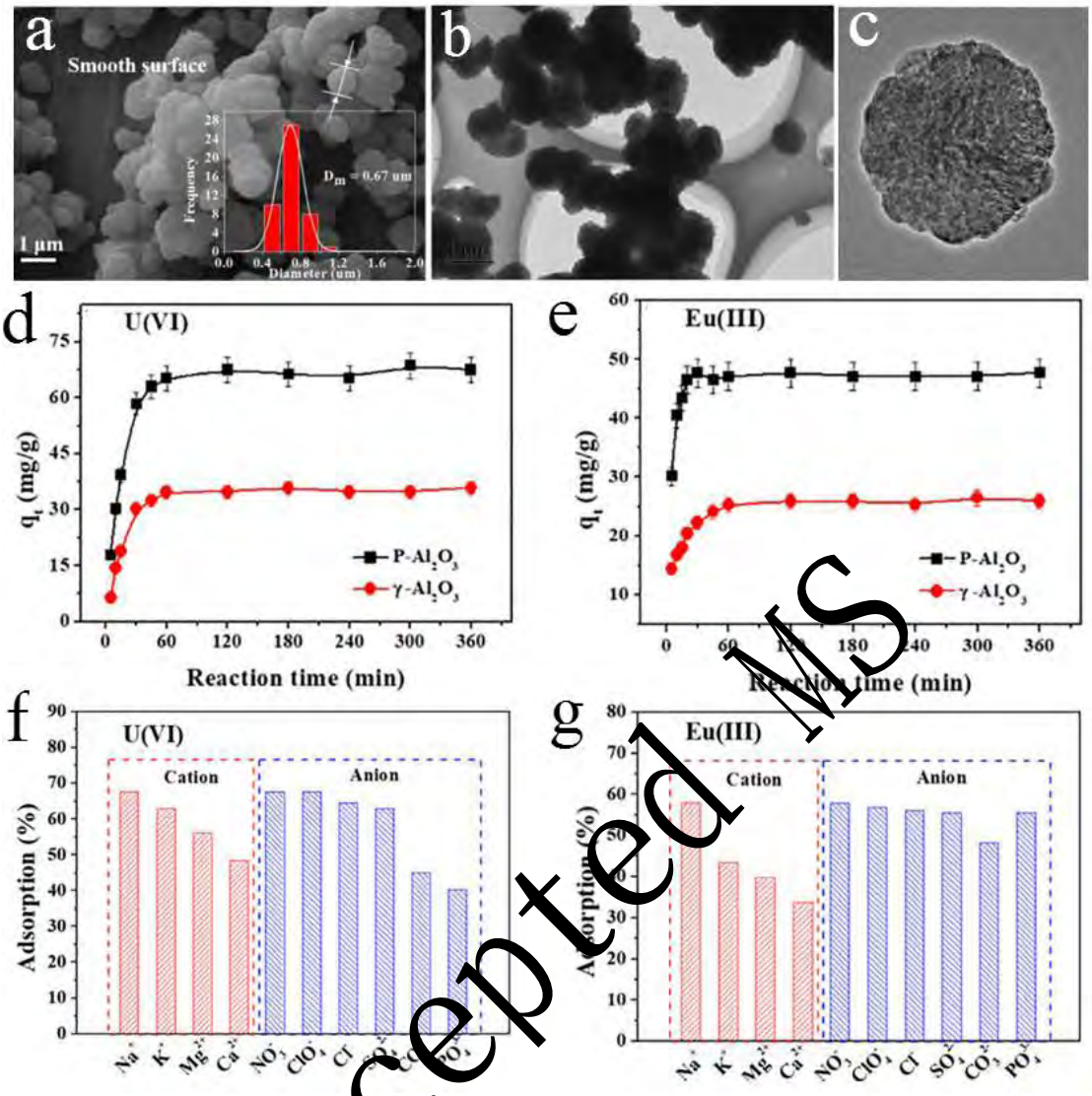

Fig. 13. (a) SEM images of P-Al_2O_3 (inset: the corresponding particle size distributions); (b) low magnification and (c) high magnification TEM images of P-Al_2O_3; adsorption kinetic curves of (d) U(VI) and (e) Eu(III) on γ-Al_2O_3 and P-Al_2O_3; effect of different cations and anions on the adsorption of (f) U(VI) and (g) Eu(III). (reaction conditions: T = 298 K; m/V = 0.1 g·L^{-1}; I = 0.01 M $NaNO_3$; pH = 5.0 for U(VI) and pH = 6.0 for Eu(III); C[U(VI)]initial = 10.0 mg·L^{-1}; and C[Eu(III)]initial = 10.0 mg·L^{-1}; the ionic strength is 0.01 M.). Reprinted with permission from Ref. [193] Copyright 2018 Elsevier.

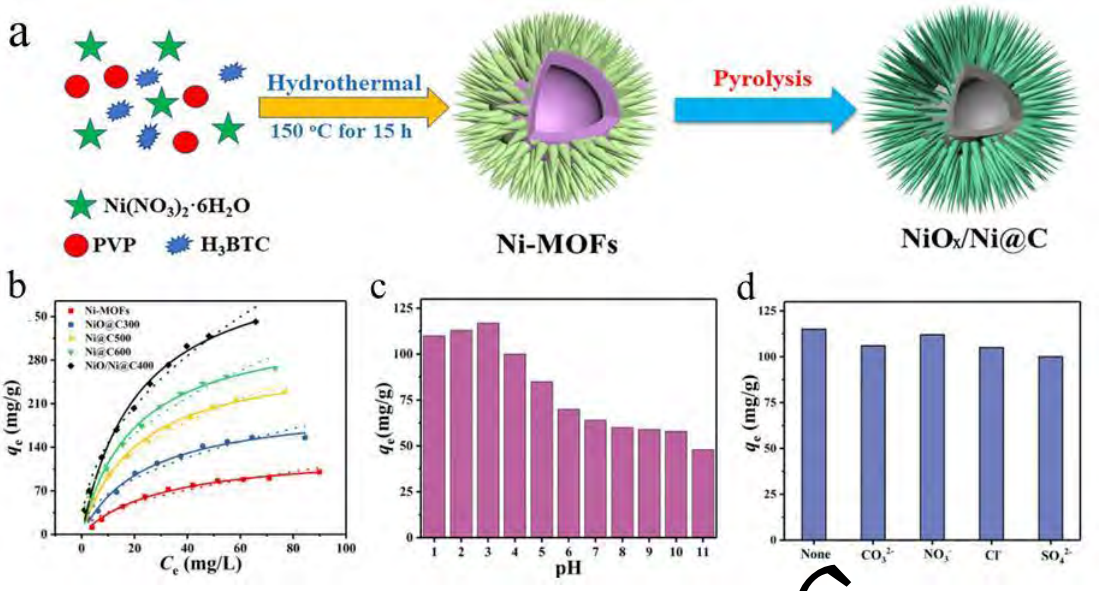

2456

2457 **Fig. 14.** (a) Schematic illustration of the synthesis of Ni-MOFs and NiOx/Ni@C; (b) adsorption

2458 isotherms of Ni-MOFs, NiO@C300, NiO/Ni@C400, Ni@C500 and Ni@C600 for As(V) removal;

2459 (c) pH effect on As(V) adsorption; (d) coexisting anion effects on As(V) adsorption (reaction

2460 conditions: pH = 3.0 ± 0.1, m/V = 0.15 g L^{-1}, C_0(As(V)) = 20 mg L^{-1}, anions concentration = 0.5 g

2461 L^{-1}, T = 298 K). Reprinted with permission from Ref. [194] Copyright 2019 Elsevier.

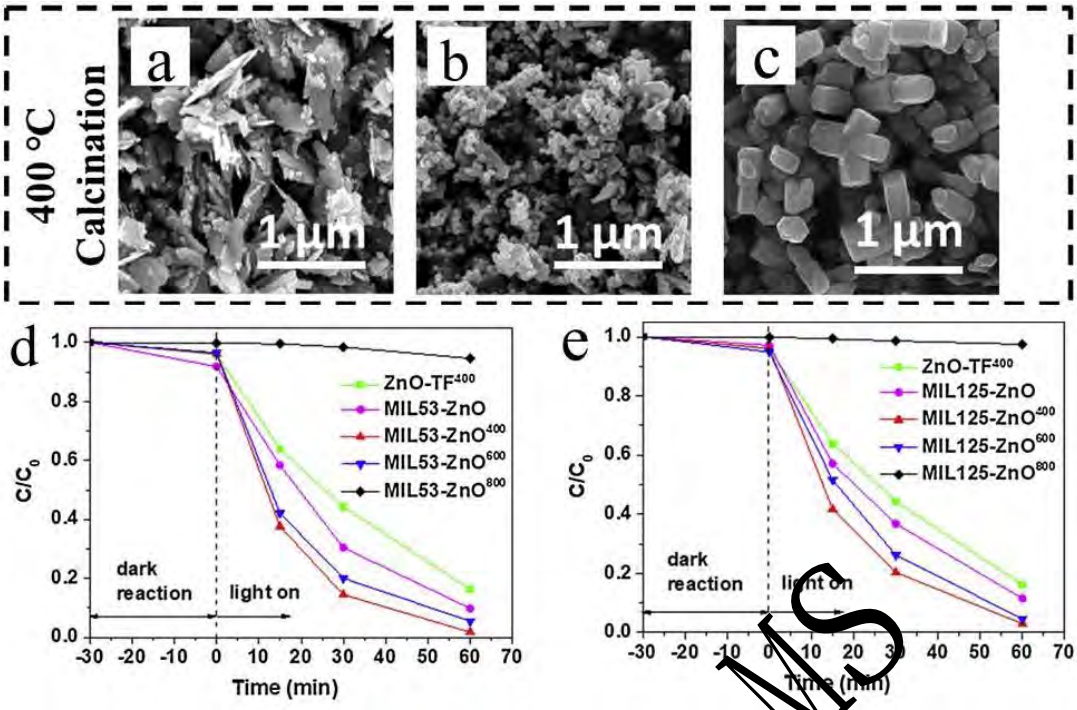

Fig. 15. SEM images of (a) MIL125-ZnO^{400}, (b) MIL53-ZnO^{400} and (c) ZnO-TF^{400}; photocatalytic degradation curves of MO on ZnO using (d) MIL-53(Al) and (e) MIL-125(Ti). Reprinted with permission from Ref. [210] Copyright 2019 Elsevier.

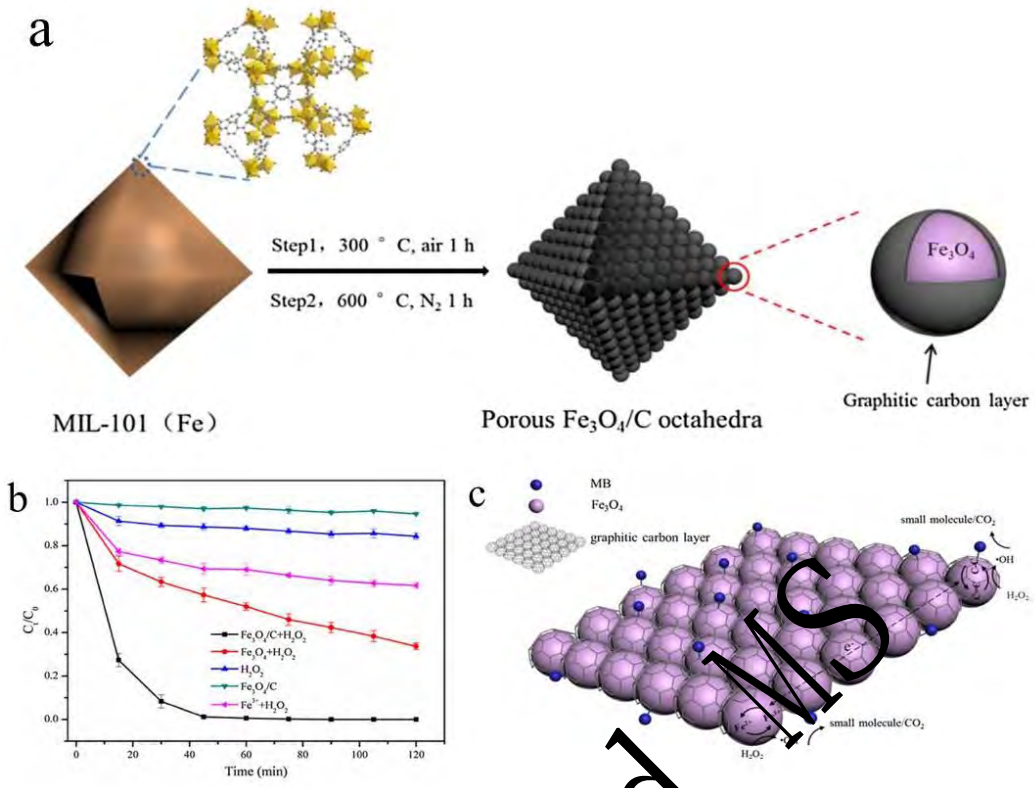

Fig. 16. (a) schematic illustration of the preparation process of MOF-derived magnetic porous Fe_3O_4/carbon octahedral; (b) MB removal efficiency under different conditions. (reaction conditions: $[MB]_0$ = 10 mg Lv, [catalyst] = 0.5 g L^{-1}, $[H_2O_2]$ = 90 mMol L^{-1}, pH = 3 and 30 ℃). (c) proposed mechanism for the heterogeneous Fenton-like reaction of the magnetic porous Fe_3O_4/carbon octahedra. Reprinted with permission from Ref. [221] Copyright 2017 Elsevier.

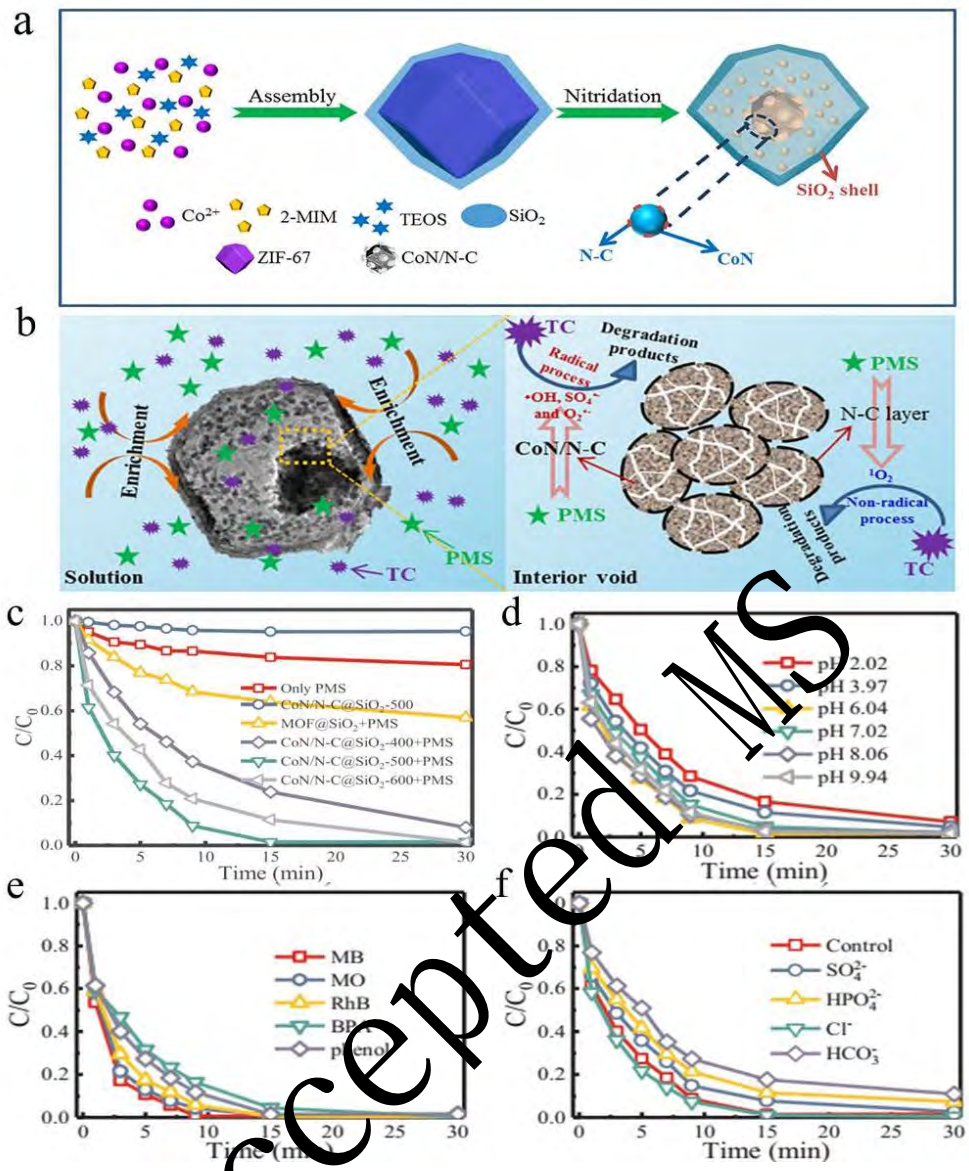

Fig. 17. (a) Schematic illustration of the fabrication procedure of the yolk-shell CoN/N-C@SiO_2 nanoreactor; (b) mechanisms for TC degradation by CoN/N-C@SiO_2-500 + PMS systems; the effect of (c) different catalysts and (d) initial pH value on TC degradation; (e) degradation of other organics in CoN/N-C@SiO_2-500 + PMS systems; (f) the effect of foreign ions on TC degradation. Reprinted with permission from Ref. [235] Copyright 2020 Elsevier.

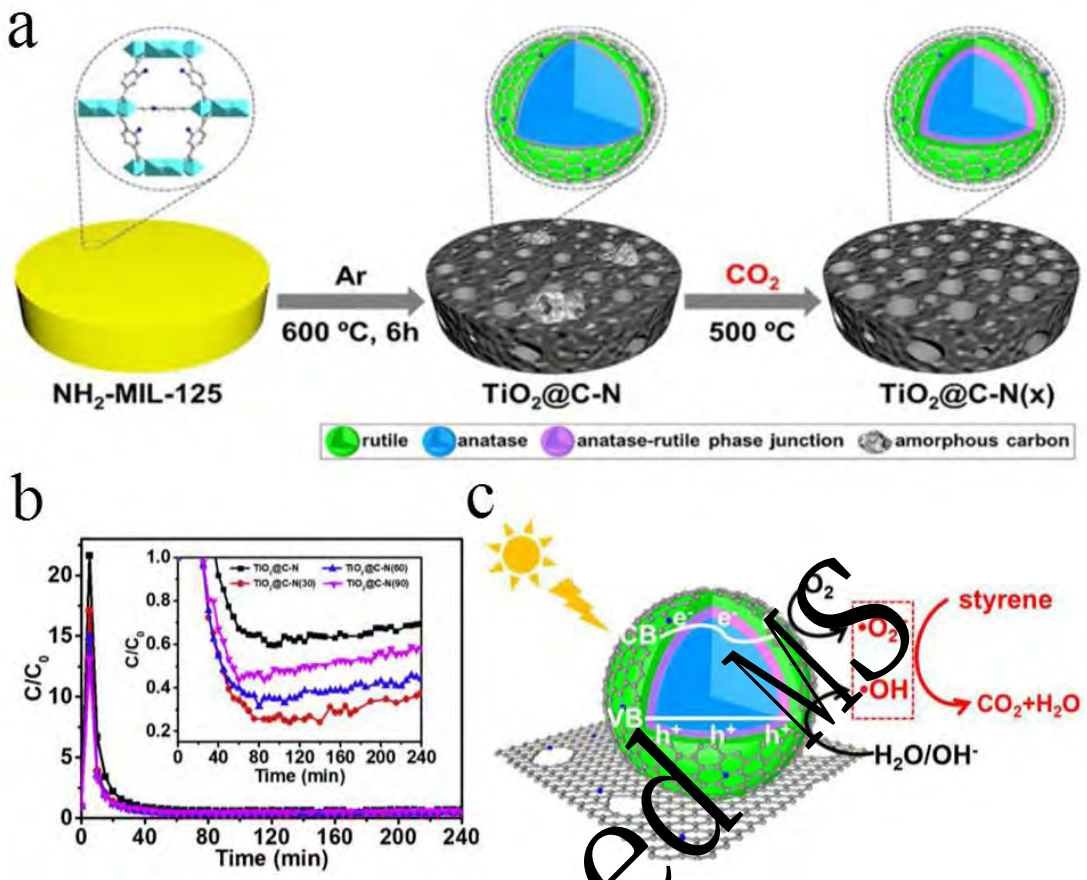

Fig. 18. (a) Illustration of the preparation strategy of TiO_2@C-N(x) nanocomposites. (b) evolution of styrene during the photocatalytic oxidation reaction by TiO_2@C-N and TiO_2@C-N(x) composites. (c) possible reaction mechanism for the photocatalytic oxidation of styrene over TiO_2@C-N(x) nanocomposites. Reprinted with permission from Ref. [81] Copyright 2019 Elsevier.

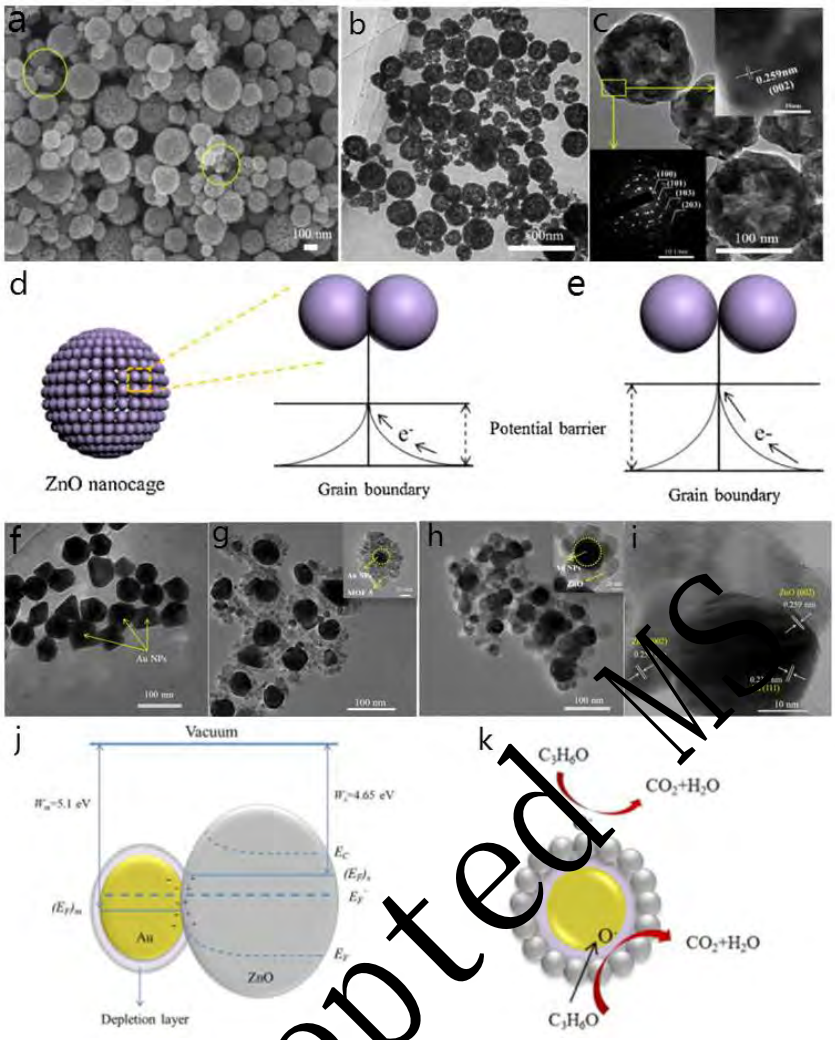

Fig. 19. (a) SEM and (b) TEM images of the as-synthesized hierarchical hollow ZnO nanocages; (c) HRTEM image of ZnO nanocages obtained at 450 ℃ (insets: lattice distance and SAED pattern); Schematic comparison of potential barrier between (d) melt ZnO nanoparticles within shells of hierarchical hollow ZnO nanocages and (e) singular ZnO nanoparticles. Reprinted with permission from Ref. [290] Copyright 2016 Elsevier. TEM images of (f) Au NPs; (g) Au@MOF-5 precursors; (h) Core-shell Au@ZnO nanoparticles; (i) HRTEM image of Au@ZnO nanoparticles; (j) energy band diagram of core-shell Au@ZnO nanoparticle. (k) redox process between acetone molecule and active oxygen species. Reprinted with permission from Ref. [291] Copyright 2016 Elsevier.

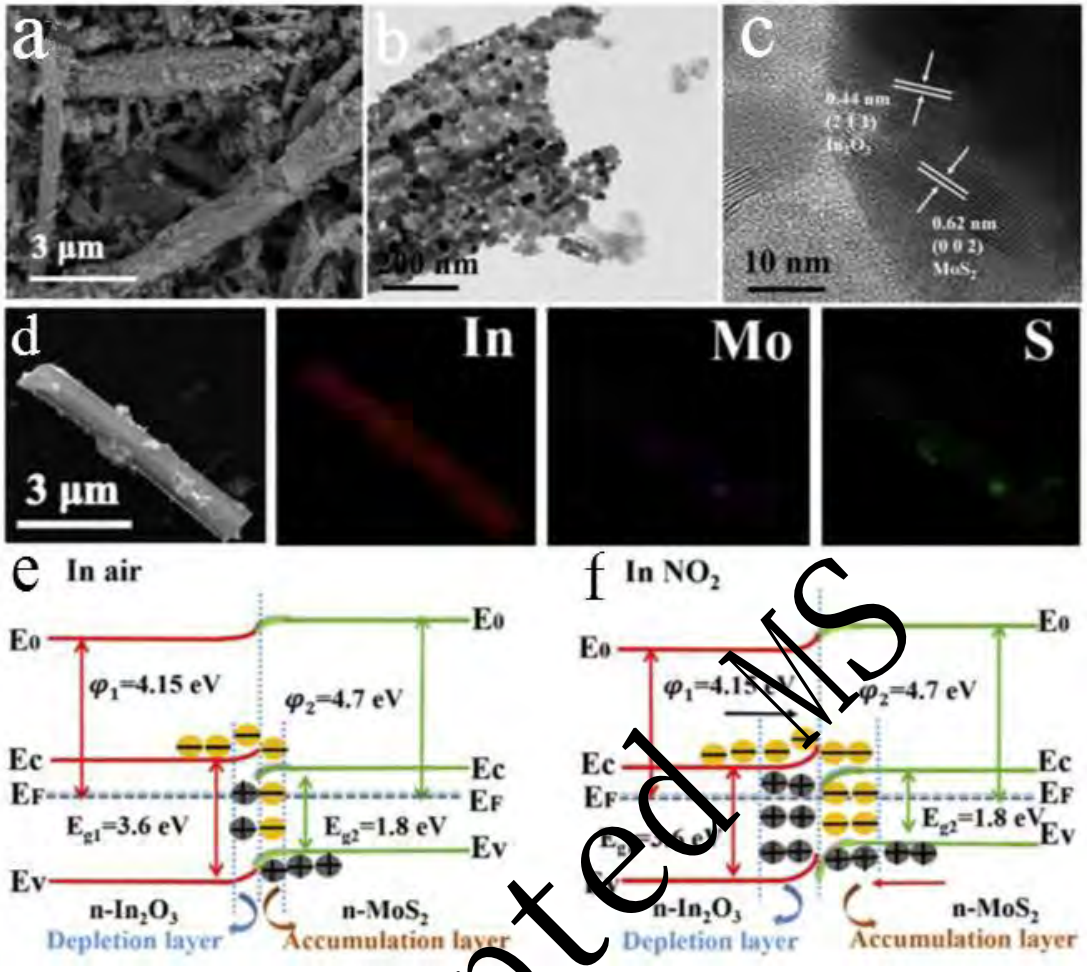

Fig. 20. (a) SEM and (b) TEM images of In_2O_3/MoS_2; (c) HRTEM micrograph of In_2O_3/MoS_2; (d) EDX mapping analysis of In_2O_3/MoS_2; Energy band structure diagram of In_2O_3/MoS_2 heterojunction in air (e) and in NO_2 (f). Reprinted with permission from Ref. [298] Copyright 2019 Elsevier.

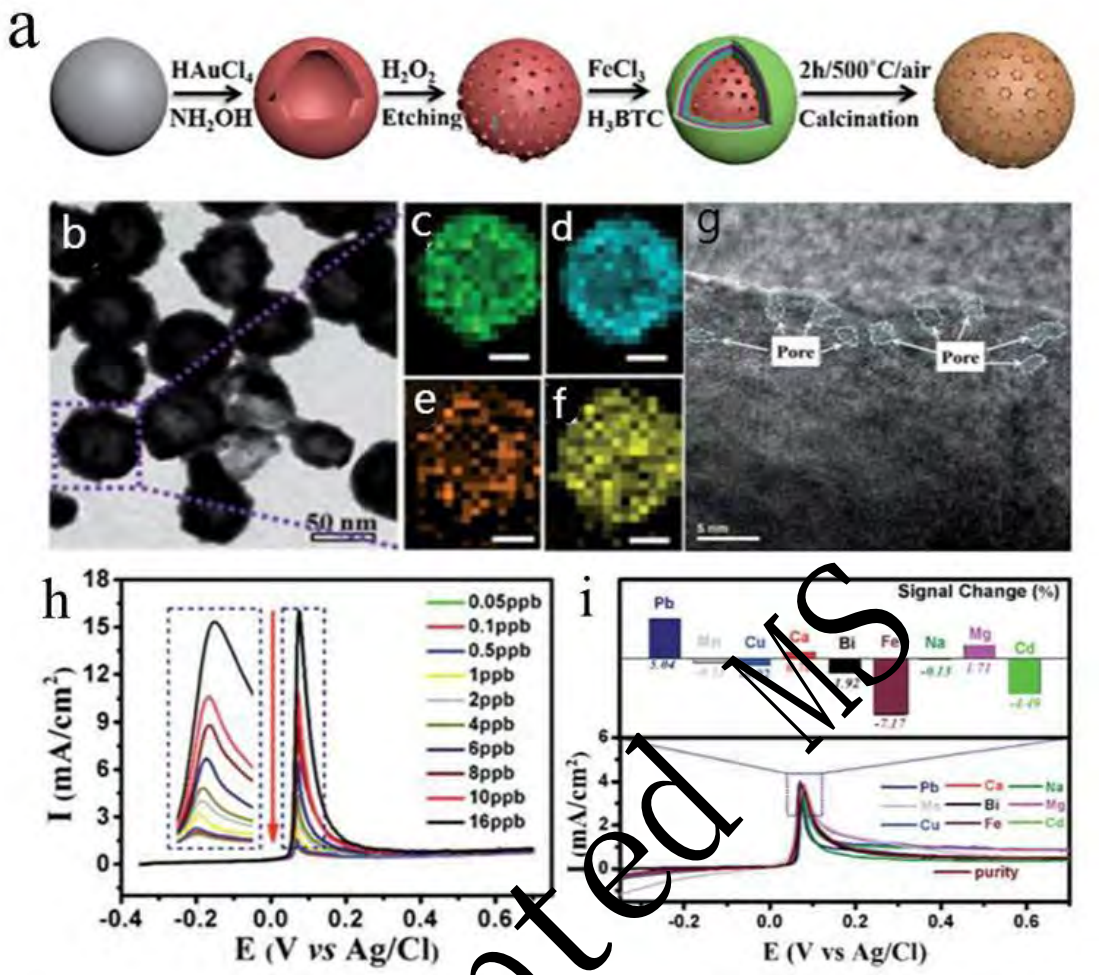

Fig. 21. (a) Schematic of the fabrication of the plasmonic Ag/Au HPNSs@FO. (b) typical TEM images of Ag/Au HPNSs@FO, (c–f) the corresponding EDS elemental mapping images of a fragment of the Ag/Au HPNSs@FO: (c) Au, (d) Ag, (e) Fe, and (f) O (scale bar in (c–f): 20 nm); (g) High-resolution TEM image of Ag/Au HPNSs@FO; (h) stripping voltammograms of the plasmonic Ag/Au HPNSs@FO electrode in 1 M HCl containing 2 ppb As(III) before (black) and after (red) 1000 cycles of accelerated stability test; (i) selectivity of the Ag/Au HPNSs@FO for As(III) in 1 M HCl containing 2 ppb As(III) in the presence of other metal ions; the concentration of each of the ions was 20 ppb. Reprinted with permission from Ref. [317] Copyright 2018 The Royal Society of Chemistry.

2507 **Table 1.** Summary of MOF-derived nanomaterials for adsorption.

MOF precursors	MOF-derived nanomaterials	Adsorption capacity	Reusability	Remarks	Ref.
MOF-5	HPC-950	310 mg g^{-1} for *p*-nitrophenol	The adsorbed amount of *p*-nitrophenol diminished slightly from 310 to 260 mg g^{-1} after five cycles.	The distinctive characteristics with hierarchical pores and partially graphitization enhanced the adsorption ability.	[108]
MOF-5	ZnO@C	Nearly 100% adsorption for RhB	Almost 80% after seven cycles, while nearly 20% in eighth cycle.	The high adsorption was attributed to the π-π interactions.	[120]
ZIF-8	IHNPC	455.95 mg g^{-1} for 17β-estradiol	The adsorption capacity decreased only about 12% after the 5th cycle.	The high adsorption was attributed to the hierarchical porous structures, ample vacant sites and low internal diffusion resistance for adsorption.	[124]
MAF-6	CDM6-K1000	408 mg g^{-1} for ibuprofen and 503 mg g^{-1} for diclofenac sodium	There was negligible decrease after five cycles for ibuprofen adsorption.	The main adsorption mechanism for ibuprofen was the van der Waals interaction.	[164]
Bio-MOF-1	BMDC-12 h	552 mg g^{-1} for ATNL and 540 mg g^{-1} for CLFA	The ATNL removal did not decrease appreciably after four cycles.	The main adsorption mechanism for ATNL was electrostatic interaction and for CLFA was H-bonding.	[190]
ZIF-8	MDC-1000	435 mg g^{-1} for SMX	The adsorption capacity slightly decreased after four cycles.	The main adsorption mechanism was H-bonding.	[191]
ZIF-8	Carbon-ZD	1148.2 mg g^{-1} for MB	The MB degradation rate still reached 99% after five cycles.	The high adsorption was endorsed by cooperative effects of the large BET surface area, well-distributed pore widths and N-doping.	[192]

MIL-53	Porous P-Al_2O_3	316.87 mg g^{-1} for U(VI) and 223.37 mg g^{-1} for Eu(III)	-	The higher adsorption capacity for U(VI) and Eu(III) were attributed to the existence of many hydroxy groups.	[193]
UiO-66	ZrSulf	824 mg g^{-1} for Hg(II)	The adsorption amounts had no obvious change after five runs.	The main adsorption mechanisms were ion exchange (at pH < 3.0), coordination of Hg(II) with sulfur-containing groups (at 3.0 < pH < 9.0), and precipitation (at pH > 9.0).	[105]
Ni-MOF	NiOx/Ni@C400	454.94 mg g^{-1} for As(V)	The adsorption capacity decreased from 115 to 80 mg g^{-1} after five cycles.	The main adsorption mechanisms were electrostatic interaction and surface complexation (As-O bond).	[194]
MIL-53(Fe)	Carbon-αFe/Fe_3C 910	511.06 mg g^{-1} for TC	The adsorption capacity slightly decreased after five cycles.	The main adsorption mechanisms were pore filling effect and electrostatic adsorption.	[195]

2508

2509 **Table 2.** Summary of MOF-derived nanomaterials for catalysis.

MOF precursors	MOF-derived nanomaterials	Application	Performance	Reusability	Ref.
ZIF-8	C-doped ZnO	Photocatalytic degradation for MB	Almost complete removal for MB within 90 min	There was no obvious deactivation after five degradation cycles.	[209]
MIL53/ MIL125	ZnO nanosheets	Photocatalytic degradation for MO	98.15% degradation by MIL53-ZnO^{400} and 96.89% degradation by MIL125-ZnO^{400} for MO in 60 min	There was no significant changes of all samples in the photocatalytic activity after five cycles.	[210]
Co/Fe-MOF	CoP/Fe_2P@mC	Photocatalytic degradation for RhB	95% degradation efficiency for RhB in 150 min	94% RhB was photodegraded after five cycle.	[211]
MIL-68(In)	CInS-2	Photocatalytic degradation for TC	Almost 100% degradation for TC within 120 min	Less degradation efficiency decrease was observed after three cycles.	[213]
MIL-101(Fe)	Fe_3O_4/C	Fenton-like degradation for MB	Almost 100% degradation for MB within 60 min	97% removal efficiency was achieved for MB after ten cycles.	[221]
[Cu/Fe]-BTC	$CuFe_2O_4$/Cu@C	Fenton-like degradation for MB	Almost 100% degradation for MB within 15 min	Original activity was retained after ten cycles.	[223]
PB	Fe_2O_3@SnO_2	Photo-Fenton degradation for RhB	99.7% degradation efficiency for RhB in 60 min	No obvious loss of RhB degradation was presented in three runs.	[224]
MIL-100(Fe)	CMIL-100@PCM	Electro-Fenton degradation for napropamide	82.3% degradation efficiency for napropamide in 60 min	A slight decrease of the napropamide degradation efficiency was	[225]

				observed after three cycles.	
Fe_yCo_{1-y}-Co PBA	$Fe_{0.8}Co_{2.2}O_4$	PMS degradation for BPA	95% BPA degradation efficiency within 60 min	Slight loss of the catalytic activity was observed in four cycles.	[232]
PB	Co_3O_4@Fe_2O_3	PMS degradation for NOR	Almost 100% degradation for NOR within 45 min	There was no significant deterioration in the four cycles.	[233]
ZIF-67	CoN/N-C@SiO_2	PMS degradation for TC	95% TC degradation efficiency within 30 min	The degradation efficiency of TC was reduced to 80% in 72 min.	[235]
MIL-100(Fe)	Nitrogen-doped graphene	PMS degradation for phenol	Almost 100% phenol removal within 30 min	Nearly 100% and 61% phenol removals were reached within 120 and 180 min in the second and third cycles.	[237]
Zn/Co-ZIF	NDHC	PMS degradation for BPA	98% of BPA removal efficiency in 5 min	Only 35% of BPA can be degraded in the second run.	[167]

2510